UQAC
Université du Québec
à Chicoutimi

Thermomechanical Behavior of Al-Mg-Mn Alloys: Effect of Mn and Na on Hot Workability

By

Mohammadreza Mofarrehi

Under supervision of Prof. X.-Grant Chen and co-supervision of Prof. Mousa Javidani

Thesis presented to the University of Quebec at Chicoutimi with a view to obtaining the degree of Philosophiae doctor (Ph. D.) in engineering

Québec, Canada

Le comportement thermomécanique des alliages Al-Mg-Mn : Effet de Mn et Na sur aptitude au formage à chaud

Résumé

Les alliages Al-Mg-Mn offrent une excellente formabilité, une résistance parfaite à la corrosion ainsi que la résistance souhaitée pour la production de carrosseries de voitures, de canettes de boissons et d'embarcations marines. La production commence typiquement par une séquence de procédés en amont comprenant le procédé semi-continu par refroidissement direct, l'homogénéisation et le laminage à chaud. La prédiction du comportement des matériaux lors du laminage à chaud a toujours été un problème compliqué. La raison en est la contribution et l'interaction de plusieurs paramètres thermomécaniques et métallurgiques dans le processus. En comprenant le comportement à la déformation et la Malléabilité à chaud des systèmes Al-Mg-Mn, il sera plus facile de contrôler les propriétés du produit final et d'éviter la défaillance du matériau pendant la déformation. Par conséquent, dans cette étude, l'effet de l'ajout de Mn dans la plage standard commerciale de (0,1 à 1% en poids) sur la formabilité à chaud des alliages Al-Mg-Mn a été étudié. La déformation à chaud a été effectuée à différentes températures (350-500℃) et taux de déformation (0,001-1s-1) par un test de compression à chaud.

Généralement, à l'état pré-déformé, Mn favorise un volume élevé d'intermétalliques contenant du fer. Il a été observé que les dispersoïdes contenant du Mn précipitaient à 0,4 % (en poids). Un ajout supplémentaire de Mn affine la taille des dispersoïdes, modifie la morphologie de l'aiguille et de la forme rhomboïdale à la forme cubique. Il augmente également la densité numérique des dispersoïdes dont la plupart avaient tendance à avoir une composition de Al6Mn. Au-dessus de 0,7 % de Mn, les dispersoïdes sont densifiés au centre des grains tandis que les joints de grains sont entourés de zones exemptes de dispersoïdes (DFZ).

En se basant sur les résultats de compression à chaud, le paramètre Zener-Hollomon a été utilisé pour évaluer l'évolution de la microstructure. En utilisant la technique EBSD, il a été déterminé que DRV et CDRX sont les mécanismes d'adoucissement dominants dans les conditions Z élevées et basses, respectivement. En coexistence avec CDRX, des indices de

recristallisation dynamique partiellement stimulée par les particules (PSN-DRX) et recristallisation dynamique discontinue (DDRX) ont été notés dans des conditions Z moyennes. L'impact majeur de l'ajout de Mn était dans la condition de déformation à faible Z, c'est-à-dire une vitesse de déformation plus faible et des températures plus élevées. C'était principalement par la contribution des dispersoïdes au retard de migration des joints de grains et à l'inhibition de CDRX. En calculant les données expérimentales à l'aide d'analyse constitutive, l'énergie d'activation pour la déformation à chaud se trouve qu'elle passe de 160 à 177 kJ/mol. Une telle augmentation est relativement modeste à cause de l'apparition de CDRX dans les DFZ.

Dans une autre approche, la modélisation dynamique des matériaux a été appliquée pour les mêmes résultats d'essais de compression à chaud afin d'ouvrir une plage de températures et de taux de déformation dans laquelle l'instabilité et les conditions de déformation sécurisées des alliages Al-Mg-Mn sont déterminées. Sur la base du modèle, la cartographie a été construite, où la zone de sécurité se situe entre 0,001-0,01s-1 à 350℃ et s'étend progressivement à tous les taux de déformation (c'est-à-dire 0,001-1s-1) avec l'augmentation de la température jusqu'à 450℃. Dans l'alliage de base à (0,1 Mn), en raison de l'absence de dispersoïdes, la puissance dissipée par DRX s'est située dans l'intervalle de 350 à 450 ℃ avec des taux de déformation de 0,001 à 0,007 s-1. Cependant, dans les alliages contenant des dispersoïdes, ce domaine rétrécissait progressivement avec la teneur en Mn jusqu'à 375-425℃ avec des taux de déformation appliqués de 0,001-0,002 s-1 dans l'alliage à 1Mn en raison de la suppression de DRX par les dispersoïdes. Les mécanismes d'instabilité observés sont la déformation des bandes à l'intérieur des grains et le cisaillement au voisinage des constituants aux joints de grains. Ce dernier a été prononcé par l'ajout de Mn puisque les intermétalliques riches en Fe deviennent plus grossiers et plus volumineux, ce qui entraîne une intensification des bandes de cisaillement adjacentes à travers la matrice.

La fissuration des bords présente un défi à long terme dans le laminage à chaud du système Al-Mg qui réduit la productivité des tôles. La fragilisation par des traces de sodium est généralement connue comme la principale raison de la fissuration des bords. Pour résoudre ce problème à l'échelle pratique et industrielle, deux alliages Al-5Mg-0,2Mn avec des contaminations <0,5 ppm et 1 ppm de Na ont été coulés par procédé DC et laminés à chaud en 11 passes (réduction de 86 %) et en 18 passes (réduction de 96 %). Des fissures

sur les bords se sont produites après 11 passes dans un échantillon à haute teneur en Na et se sont propagées vers la masse sous l’effet de l’augmentation de nombre de passes. Le chemin de la fissure était la nucléation et la coalescence des vides au voisinage des constituants Mg2Si. Plus la teneur en Na est élevée, plus la décohésion de l'interface Mg2Si/Al et la cavitation sont importantes. Un tel mécanisme explique la contribution des bandes ménisques aux fissures profondes.

Thermomechanical Behavior of Al-Mg-Mn Alloys: Effect of Mn and Na on Hot Workability

Abstract

Al-Mg-Mn alloys offer excellent formability, perfect corrosion resistance, and desired strength to produce car bodies, beverage cans, and marine crafts. Generally, the manufacturing process of these parts begins with a series of upstream processes, including direct chill casting, homogenization, and hot rolling. Several thermomechanical and metallurgical parameters interact during the hot rolling process; therefore, predicting the materials' behavior has always been complex. In order to control the properties of final products and prevent material failure during deformation, it is essential to understand the hot deformation behavior and hot workability of Al-Mg-Mn systems. Therefore, in this study, the effect of Mn addition at the standard commercial range of (0.1-1wt.%) on the hot deformability of Al-Mg-Mn alloys at various temperatures (350-500 °C) and strain rates (0.001-1 s^{-1}) was investigated.

Typically, Mn promotes high volume formation of Fe-bearing intermetallics in a pre-deformed state and it was observed that Mn-containing dispersoids precipitate in the presence of 0.4 wt.% Mn. In addition, by further adding Mn, the size of dispersoids is refined, their number density is increased, and also their morphology is altered from needle and rhomboidal to cube-like shapes, most of which have a composition of Al_6Mn. Moreover, above 0.7 wt. % Mn, dispersoids are densified at the central part of the grains, whereas grain boundaries are surrounded by dispersoids free zones (DFZs).

The microstructure evolution was investigated utilizing the Zener-Hollomon parameter based on the hot compressive results. The Electron Backscattered Diffraction (EBSD) results showed that dynamic recovery (DRV) and continuous dynamic recrystallization (CDRX) are dominant softening mechanisms at high and low Z conditions, respectively. On the other hand, at medium Z conditions, particle-stimulated nucleation (PSN-DRX) and discontinues dynamic recrystallization (DDRX) coexisted with CDRX. The main impact of Mn addition on microstructure evolution was at the low Z deformation condition, i.e. lower strain rate and higher temperatures. This impact is mainly attributed to the contribution of dispersoids to the boundary migration retardance and CDRX inhibition. Although the activation energy for hot deformation is increased from 160 to 177 kJ/mol,

but such an increasement is relatively modest due to the occurrence of CDRX at DFZs.

In another approach, Dynamic Material Modeling was used on the same findings of hot compression testing to evaluate the instability and safe deformation conditions of Al-Mg-Mn alloys over a range of temperatures and strain rates. On the basis of the model, the processing map was constructed at which the safe zone lies in between 0.001-0.01 s^{-1} at 350 °C and gradually expands to all strain rates (i.e. 0.001-1 s^{-1}) as temperatures increases to 450 °C. Due to the absence of dispersoids in the base alloy (i.e. 0.1Mn), the power dissipated by DRX fell in the range of 350-450 °C with strain rates of 0.001-0.007 s^{-1}. However, this domain in dispersoid-containing alloys was progressively shrinking by Mn content down to 375-425 °C with operating strain rates of 0.001-0.002 s^{-1} in 1Mn alloy due to the DRX suppression by dispersoids. Deformation bands in grain interiors and shearing at the vicinity of constituents at grain boundaries were found to be the instability mechanisms. Moreover, with Mn addition, Fe-rich intermetallics get coarser and larger in volume, and adjacent shear bandings across the matrix become more intense.

Edge cracking is a long-term issue in the hot rolling of the Al-Mg system, lowering sheet production productivity. The principal cause of edge cracking is often assumed to trace sodium embrittlement. Two Al-5Mg-0.2Mn alloys with 0.5ppm and 1ppm Na contaminations were cast using DC method to address this issue in industrial application. Then, the casted alloys were hot rolled for 11 and 18 passes to reach a reduction of 86% and 96%, respectively. After 11 passes in the high-Na sample, edge cracks occurred and propagated toward the bulk with additional passes. The void nucleation and coalescence at the periphery of the Mg_2Si components was discovered to be the crack path. The higher the Na concentration, the more the Mg_2Si/Al interface decohesion and cavitation. This process explains the contribution of meniscus bands to the profound cracks.

Table of Contents

List of Tables

List of Figures

List of Abbreviations

AA	Aluminum alloy
DRV	Dynamic recovery
DRX	Dynamic recrystallization
CDRX	Continuous dynamic recrystallization
DDRX	Discontinuous dynamic recrystallization
GDRX	Geometrical dynamic recrystallization
PSN-DRX	Particle stimulated nucleation dynamic recrystallization
LAB	Low angle boundaries
MAB	Medium angle boundaries
HAB	High angle boundaries
GB	Grain boundary
DB	Deformation band
ASB	Adiabatic shear band
DFZ	Dispersoid free zone
DZ	Dispersoid zone
Z	Zener-Hollomon parameter
SEM	Scanning electron microscopy
TEM	Transmission electron microscopy
EBSD	Electron backscattered diffraction
EDS	energy dispersive spectroscopy
DC	Direct chill casting
OM	Optical microscope
HS	High sodium
LS	Low sodium
HF	Hydrofluoric acid
HV	Hardness Vickers
V	Vector
AARE	Average absolute relative error

List of Symbols

Al	Aluminum
Fe	Iron
Mg	Magnesium
Mn	Manganese
Si	Silicon
Cu	Copper
Na	Sodium
H	Hydrogen
O	Oxygen
Ti	Titanium
B	Brome
α	Stress multiplier
β	Beta constant
Q	Activation energy
℃	Centigrade degree
s	Second
μm	Micrometre
kJ/mol	Kilo joule per mole
ε	True strain
$\dot{\varepsilon}$	Strain rate
σ	Stress
MPa	Mega pascal
m	Strain rate sensitivity
R	Universal gas constant
T	Temperature
ξ	Instability criterion
η	Power dissipation
R^2	Correlation coefficient

Acknowledgement

My deep gratitude goes out to my thesis supervisor, Professor X. Grant Chen, and co-supervisor, Professor Mousa Javidani, for their excellent guidance and continuous support throughout the project. In addition to their scientific insights and invaluable suggestions, their confidence in my abilities has proven to be a tremendous source of inspiration for me.

Grateful acknowledgement is attributed to the financial support from the ***Natural Sciences and Engineering Research Council of Canada (NSERC)*** *and from* ***Rio Tinto Alcan*** *through the NSERC Industrial Research Chair in Metallurgy of Aluminum Transformation at the University of Québec at Chicoutimi.*

Special thanks for technical support on my research project from Dr. Zhan Zhang for TEM and SEM training and guidance. I am thankful for the support of Dr. Kun Liu, Dr. Emad Elgallad, and Mr. Zhixing Chen. Also, I would like to Mr. Dany Racine, Samuel Dessureault and Felix Tremblay for Gleeble training, alloy casting, and sample machining, respectively.

Meanwhile, I am also deeply indebted to my colleagues for their fruitful collaboration, scientific discussions and sharing their research experiences with me: Ahmed Algendy, Esmaeil Pourkhorshid, Mohammad Khoshghadam Pireyousefan Mohamed Ahmed, Mohamed Qassem, Peng Hu, Liying Cui, Siamak Nikzad Khangholi, Shuai Wang, Cong Li, Zimeng Wang, Jovid Rakhmonov, Dong Li, Redouane Farid, Henry Agbe, Karthikeyan Rajan, and Lanfeng Jin. Special thanks go to Ali Elasheri and Chaima Hajji.

I dote on my family-like friends in Chicoutimi: Shahriyar&Parinaz, Samaneh, Khatereh, and Mohammad.

Chapter 1: Introduction

Wrought 5xxx or Al-Mg-Mn series are non-heat-treatable aluminum base alloys which have a high Mg content (~5%). Along with the high mechanical properties achieved from work hardening processes, they also show excellent weldability, resistance to atmospheric /seawater corrosion, and very good formability. Therefore, they are favorable to be applied in the production of automotive parts, storage tanks, marine utilization structures, architectural applications, aerospace features, and beverage cans [1]. The 5xxx alloys are mainly used in the sheet form. The sheets are commercially produced through “Direct Chill” casting by which the large ingots are fabricated and then subjected to a variety of multi-parameter processes including homogenization treatments, hot rolling, and cold rolling [2].

During the hot rolling process for sheet production, the strengthening effect of the progressive work hardening by deformation is relieved by restoration mechanisms. The main mechanisms are Dynamic Recovery (DRV) and Dynamic Recrystallization (DRX) [3,4]. DRV stands for microstructural defects being restored to their original homogenous state in the course of plastic flow. Concurrently, the process of energy-free volumes developed through the deformed substructure to new grains is called DRX. The DRX mechanism is categorized based on the characteristics of grain structure to discontinues (DDRX), continues (CDRX), and geometric (GDRX) dynamic recrystallization [5]. Various thermomechanical parameters, including deformation temperature, strain rate, and strain degree, dictate how softening takes place. Acquired knowledge of the hot deformation behavior and the correlated mechanisms aids desirable control of the alloy’s properties.

The mechanical properties of the Al-Mg-Mn system are affected by the chemical composition and the history of thermomechanical processing. Mn is a key element that provides mechanical properties via strain hardening strengthening. With the addition of Mn, Mn-bearing sub-micron intermetallics called dispersoids can form during homogenization due to the decomposition of Mn atoms from supersaturated solid solution [6,7]. The plasticity of the Al-Mg-Mn alloys at elevated temperatures is highly influenced

by the Mn-containing thermostable dispersoids [8]. This can be expounded by the interaction of dispersed particles with the substructure dynamically evolved in the matrix. To optimize the hot formability of alloy, a better understanding of the microstructural evolution related to the effect of micro-alloying elements during hot deformation is necessary.

The thermomechanical process of the Al-Mg-Mn alloys sometimes undergoes a large extent of failure linked to the chemical composition. Sodium in the order of ppm has a detrimental effect on the hot rolling process of the sheet production line [9]. In industrial practice, during the hot rolling of Al-Mg-Mn ingots, the edge cracking takes place at the sides of the rolled slabs. From the mechanical point of view, the edges of the slabs tolerate the longitudinal tensile stress in contrary to the compressive stress of center. Edge cracks are usually initiated in all ingots, but the level of severity changes from one ingot to another. The general notion is the defects which stimulate void nuclei that later coalesce to generate microcracks, a path for macrocracks propagation [10]. Sodium contamination during the DC-casting process of Al-Mg-Mn is responsible for such defects. Several assumptions were introduced as mechanisms of crack initiation from which the grain boundary weakening by segregation of trace Na is more popular [9,11–14]. It was reported [9] that Si addition can decrease the effect of the Na-embrittlement by the concentration of Na atoms on the Mg_2Si particles. However, it is argued [15] that this hypothesis was doubtful and suggested that the deterioration of Na at elevated temperatures has more microstructural aspects which need to be investigated.

1.1 Problem statement

Al-Mg-Mn aluminum alloys are generally subjected to the hot rolling process to produce sheets; it is thus necessary to optimize the parameters of such thermomechanical processing for maximum efficiency and workability of the product metals. Due to the industrial emergency, the investigation of edge cracking was prioritized. However, for the sake of academic research, hot compressive behavior of rolling process was simulated at various Mn contents to clarify the fundamentals for future alloy developments.

Adding Mn to aluminum alloys promotes formation of fine Mn-containing dispersoids [16,17]. Mn has a remarkable impact on the dispersoids evolution during pre-deformation heat treatment which still needs to be investigated. The effect of type, size, morphology, and distribution of dispersoids on hot formability was less reported.

Deformation of Al-Mg alloys at elevated temperatures undergoes complex competition of hardening and softening mechanisms. The role of Mn on the hot formability during hot deformation is still lacking in the Al-Mg-Mn alloys [18–21]. To address this issue, systematic analyses in terms of microstructure evolution must be carried out to understand the hot deformation behavior.

The ultimate objective in rolling process of Al-Mg-Mn alloys is to manufacture products with controlled microstructures and properties. This can be achieved by having knowledge on how deformation condition affects the microstructure. The safe and instability deformation conditions of Al-Mg-Mn has not been investigated properly. Plus, it is not clear how Mn content affects these conditions. No study has been determined the impact of Mn on the stability or instability mechanisms.

Trace sodium embrittlement tends to profoundly reduce the productivity in hot rolling of Al-Mg-Mn alloys. Edge cracking caused by Na has not been fully understood. Many lab-scale attempts have been done to figure out the mechanism behind; however, not sufficient investigations were devoted to the industrial practice. The role of microstructural components, specifically intermetallic constituents is the subject of debate [9,15]. In order to achieve optimum processing, it is necessary to bring more evidence from different aspects of Na-induced edge cracking. The final goal is to assist the industry to improve the processes in order to increase the quality of products.

1.2 Originality Statement

In this project, the response of Al-Mg-Mn alloys to Mn addition and Na contamination during hot deformation was investigated. For the Mn project, two approaches including constitutive and Dynamic Material Modeling was applied. In the constitutive analyses, Mn was systematically added to Al-5Mg alloy from 0.1 to 1 wt.% with intervals of 0.3. Mn refines the dispersoids and increases their number density. Based on Zener-Hollomon parameter, the microstructures were categorized into high/medium/low Z conditions. DRV and instability mechanisms were active at high Z condition. In medium Z, CDRX and partially DDRX and PS-DRX were observed. In low Z condition CDRX was active throughout the base alloy (0.1Mn) but it was detected only at DFZs of grain boundaries in high Mn alloys.

The second part consists of establishment of processing map on the basis of DMM of the experimental results and correlation of different zones to the microstructural evolutions. Shearing/deformation banding were the instability and DRV/DRX were the main softening mechanisms. The results showed that although instability conditions did not change with increase of Mn, however, total shearing increases. That is because the volume of intermetallics and related shearing at their vicinity increases by Mn. Two peaks of power dissipation at 400℃/0.001s^{-1} and 500℃/1s^{-1} were observed due to DRX. At both conditions, high Mn alloy showed less recrystallization because of suppressive effect of dispersoids.

The third part of this study was attributed to the sodium induced edge cracking in Al-Mg-Mn alloys. The microstructural analyses revealed that inverse segregation increases the volume of the intermetallics near the surface. The edge crack can initiate at the periphery of the intermetallics. It was observed that in industrial practice, Mg_2Si constituents involve in void nucleation since Na atoms segregate on these intermetallic. It was shown that cracks are more profound at meniscus bands due to the higher concentration of constituents.

1.3 Thesis outline

The present Ph.D. thesis contains seven chapters. Following introduction, a literature review is carried out on the history of the Al-Mg-Mn, applications, and production process. Also, fundamentals of softening and instability mechanisms are discussed properly. Moreover, a review on the previous studies conducted on the sodium embrittlement in Al-Mg alloys was provided. Chapter 3 consists of experimental procedure, materials, and equipment used in this study.

In chapter 4, an under-review paper titled as “Effect of Mn content on the hot deformation behavior and microstructure evolution of Al-Mg-Mn 5xxx alloys” in the *Journal of Science and Engineering A* is presented. In this chapter the impact of Mn on the pre-deformed microstructure specifically Mn-rich dispersoids in terms of distribution, density, and type were investigated. Then examinations were carried out by hot compression test to determine how these sub-micron intermetallics affect the hot deformation behavior. Subsequently, the results were used for the prediction of behavior by constitutive equations.

In chapter 5, Dynamic Material Modeling was employed to the experimental results of previous chapter to show the correlation between microstructural characteristics and hot workability. The results illustrated the unsafe, safe, and optimum hot deformation conditions in Al-Mg-Mn alloys regarding the Mn effect. The manuscript of this chapter will be submitted in *Journal of Materials Science and Performance*.

Chapter 6 is dedicated to the sodium induced edge cracking of Al-Mg-Mn alloys. For the sake of industrial requirement, the microstructural evolutions from cast to the rolling stage were carried out. The results indicated a large difference between the microstructure at the surface and centre of the ingots. The detrimental role of Mg_2Si intermetallics was demonstrated which plays a main role in deep cracks occurred in meniscus bands. The findings of this study were published in *Philosophical Magazine* entitled as “On the intermetallic constituents in the sodium-induced edge cracking of hot-rolled AA5182 aluminum alloys”.

In chapter 7, general conclusions and recommendations for future works are presented. In addition to these main body chapters, appendix was also included providing results on the effect of Si on the hot deformation behavior of Al-Mg-Mn alloys which showed negligible influence.

1.4 Objectives

In this thesis, followed by the general background of previous works and some details on the methodology, the main body will specifically address the objectives below:

Part 1. **Investigate the impact of Mn on the hot deformation behavior and microstructural evolution of Al-Mg-Mn alloys.**

1. Study the effect of Mn on the microstructural components including grain structure and dispersoid evolution in as-cast and as-homogenized state.

2. Determination of the impact of Mn content and related Mn-containing dispersoids on the hot deformation behavior and softening mechanisms.

3. Constitutive analyses of the flow stress curves to determine the material constants and activation energies for hot deformation at different Mn contents.

Part 2. **Investigate the impact of Mn on the hot workability and processing map of Al-Mg-Mn alloys.**

1. Construct the processing map based on the Dynamic Material Model by calculation of the data obtained from hot compression test.

2. Determine the impact of Mn on the safe and optimum deformation conditions in correlation with the microstructural evolution.

3. Demonstrate the instability deformation conditions based on the processing map and explain how Mn affects the instability mechanisms.

Part 3. **Investigate the impact of trace Na on the edge crack of Al-Mg-Mn sheets in correlation with the microstructural evolution.**

1. Examine the as-cast and as-homogenized microstructural characteristics of the subsurface and center of a direct chill cast Al-Mg-Mn ingots.

2. Compare the details of the crack formation at the edge of the slab at different sodium contents and rolling passes.

3. Demonstrate the role of the constituents and meniscus bands in edge crack initiation and propagation.

1.5 References

[1] A. Poznak, D. Freiberg and P. Sanders, *Automotive Wrought Aluminium Alloys*, in *Fundamentals of Aluminium Metallurgy*, Elsevier Ltd., 2018, pp. 333–386.

[2] D.G. Eskin, *Direct chill casting: Development of the technology*, in *Physical Metallurgy of Direct Chill Casting of Aluminum Alloys*, CRC Press, 2008, pp. 1–17.

[3] O. Engler and J. Hirsch, *Control of recrystallisation texture and texture-related properties in industrial production of aluminium sheet*, Int. J. Mat. Res. 100 (2009), pp. 564–575.

[4] H.J. McQueen, S. Spigarelli, M.E. Kassner and E. Evangelista, *Metal foming and deformation modes*, in *Hot Deformation and Processing of Aluminum Alloys*, Taylor & Francis Group, 2011, pp. 21–47.

[5] K. Huang and R.E. Logé, *A review of dynamic recrystallization phenomena in metallic materials*, Mater. Des. 111 (2016), pp. 548–574.

[6] Y.J. Li and L. Arnberg, *A eutectoid phase transformation for the primary intermetallic particle from Alm(Fe,Mn) to Al3(Fe,Mn) in AA5182 alloy*, Acta Mater. 52 (2004), pp. 2945–2952.

[7] Y.J. Li and L. Arnberg, *Solidification structures and phase selection of iron-bearing eutectic particles in a DC-cast AA5182 alloy*, Acta Mater. 52 (2004), pp. 2673–2681.

[8] H.J. McQueen, S. Spigarelli, M.E. Kassner and E. Evangelista, *Hot Working of Dispersoids and Solute Alloys*, in *Hot Deformation and Processing of Aluminum Alloys*, CRC Press, 2011, pp. 143–183.

[9] K. Horikawa, S. Kuramoto and M. Kanno, *Intergranular fracture caused by trace impurities in Al-5.5mol %Mg alloy*, Acta Mater. 49 (2001), pp. 3981–3989.

[10] H. Riedel, F. Andrieux, T. Walde and K. Karhausen, *The Formation of Edge Cracks during Rolling of Metal Sheet*, Steel Res. Int. 78 (2007), pp. 818–824.

[11] G.H. Lu, Y. Zhang, S. Deng, T. Wang, M. Kohyama, R. Yamamoto et al., *Origin of intergranular embrittlement of Al alloys induced by Na and Ca segregation: Grain boundary weakening*, Phys. Rev. B - Condens. Matter Mater. Phys. 73 (2006), pp. 1–5.

[12] H. Yamada, K. Horikawa and H. Kobayashi, *Effect of trace sodium on high temperature embrittlement in quasi-static and impact deformation of Al–5 mass% Mg alloys*, J. Japan Inst. Light Met. 60 (2010), pp. 31–35.

[13] S. Zhang, O.Y. Kontsevoi, A.J. Freeman and G.B. Olson, *Sodium-induced embrittlement of an aluminum grain boundary*, Phys. Rev. B - Condens. Matter Mater. Phys. 82 (2010), pp. DOI:10.1103/PhysRevB.82.224107.

[14] S. Zhang, O.Y. Kontsevoi, A.J. Freeman and G.B. Olson, *Aluminum grain boundary decohesion by dense sodium segregation*, Phys. Rev. B - Condens. Matter Mater.

Phys. 85 (2012), pp. 1–8.

[15] S.P. Lynch, *Comments on Intergranular fracture caused by trace impurities in an Al-5.5 mol% Mg alloy,* Acta Mater. 47 (2002), pp. 125–129.

[16] X. Qian, N. Parson and X.G. Chen, *Effects of Mn addition and related Mn-containing dispersoids on the hot deformation behavior of 6082 aluminum alloys*, Mater. Sci. Eng. A 764 (2019), pp. DOI:10.1016/j.msea.2019.138253.

[17] C.L. Liu, X. Wang, N.C. Parson and W.J. Poole, *The effect of Mn on the high temperature flow stress of Al–Mg–Si alloys*, Mater. Sci. Eng. A 802 (2021), pp. 140605.

[18] G. Avramovic-Cingara, H.J. McQueen and D.D. Perovic, *Comparison of torsion and compression constitutive analyses for elevated temperature deformation of Al-Li-Cu-Mn alloy*, Mater. Sci. Technol. 19 (2003), pp. 11–19.

[19] H.J. McQueen, E. Fry and J. Belling, *Comparative constitutive constants for hot working of Al-4.4Mg-0.7Mn (AA5083)*, J. Mater. Eng. Perform. 10 (2001), pp. 164–172.

[20] S. Ding, S.A. Khan and J. Yanagimoto, *Constitutive descriptions and microstructure evolution of extruded A5083 aluminum alloy during hot compression*, Mater. Sci. Eng. A 728 (2018), pp. 133–143.

[21] S. Ding, S.A. Khan and J. Yanagimoto, *Flow behavior and dynamic recrystallization mechanism of A5083 aluminum alloys with different initial microstructures during hot compression*, Mater. Sci. Eng. A 787 (2020), pp. DOI:10.1016/j.msea.2020.139522.

Chapter 2: Theoretical Background and Literature review

2.1 Al-Mg-Mn system alloys

Al-Mg-Mn or commercially called 5xxx series, are non-heat treatable aluminum base alloys which are characterized by their high Mg contents (~5 %) [1]. The 5xxx alloys exhibit remarkable energy absorbance before fracture [1]. This makes them favorable for critical applications where superior toughness is vital [1]. They are also readily weldable by commercial procedures and have excellent resistance to atmospheric and seawater corrosion [2]. Therefore, Al-Mg-Mn alloys are principally used in manufacturing automotive parts such as body panels and reinforcement members [3]. In addition, they are a very good choice for production of rigid parts (tabs) of beverage cans [4]. Moreover, 5xxx series are attractive for a wide range of applications, for instance, building highway structures including bridges, storage tanks, and pressure vessels [2]. Besides, they are applied in marine utilization structures, architectural applications, aerospace features, milk crates, hydraulic tubes, and appliances [2].

Mg is the key element that provides the mechanical properties by solid solution strengthening [5]. Other common elements of industrial composition include Mn (0.2-0.8 %), Fe (<1 %), Si (<0.3), Cr (0.1-0.25 %) and Cu (~1 %) [2]. With Mg addition, the misfit in the lattice of the Al matrix entangles the mobile dislocations to increase the work hardening effect by which the required strength is acquired [5]. Such a specific characteristic of Al-Mg-Mn alloys is employed to achieve the mechanical properties through strain hardening and stabilization treatments [2]. In practice, the ultimate tensile strength order is usually from 120 to 450 MPa. Yield strength varies from 40 to 350MPa and the hardness alters from 20 to 100 HB [5]. Some microstructural features, namely intermetallic constituents or dispersoids promote the hardening phenomenon [6,7]. During casting, primary phases containing the forementioned elements are solidified in the Al matrix; some exemplified ones are Mg_2Si, $Al_6(Fe,Mn)$, and α-Al(Fe,Mn)Si [6,7]. Other metastable eutectic phases such as τ-Al_6CuMg_4, β-Al_8Mg_5, and $Al_3(Fe,Mn)$ are formed as well in the

low temperature solidifying reactions. The latter phases can be resolved back in the solid state or transform into other stable ones through the homogenization process [6,7].

2.2 Production of 5xxx sheets

In order to serve the needs of 5xxx sheet final consumers, a sequence of fabrication and forming technics were developed. The journey begins with melt aluminum alloying through a method called “Direct Chill” [8] casting by which the large ingots are fabricated and then subjected to the variety of multi-parameter processes including homogenization treatments, hot rolling, and cold rolling [1].

2.3 Direct chill casting

Direct chill (DC) casting is an industrial scale method of producing wrought aluminium ingots. Developed in the 1930s, the process has been being successfully used and improved until today to produce 5xxx ingots [8]. As illustrated in Fig. 2-1, melt enters from the top of mould at where it begins to solidify when touching the mould walls (primary cooling). Here, the outer shell forms and shapes the base of the ingot. Along with vertically lowering the starting head at a constant speed, continuous filling maintains the level of melt [8]. Meanwhile the shell is cooled down supplementally by jet waters installed below the top-head. It is called secondary cooling which extracts the major heat at the surface while inside the shell contains a semi-solid/ liquid mix (sump) until the whole ingot is formed and immersed into water [8]. Subsequently, finishing practices such as surface scalping are applied to make the ingot ready for the thermomechanical processes [8].

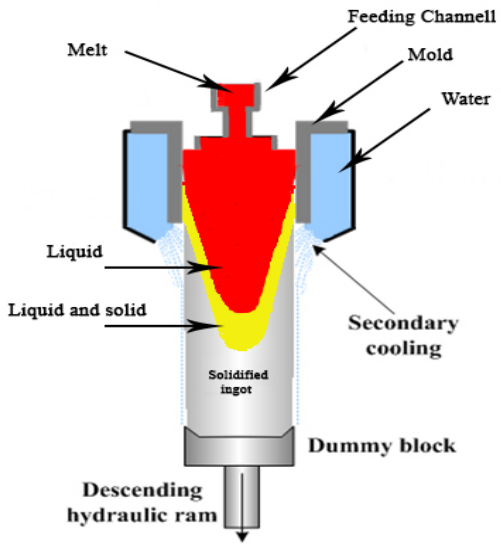

Fig. 2-1: A schematic of the direct chill casting method

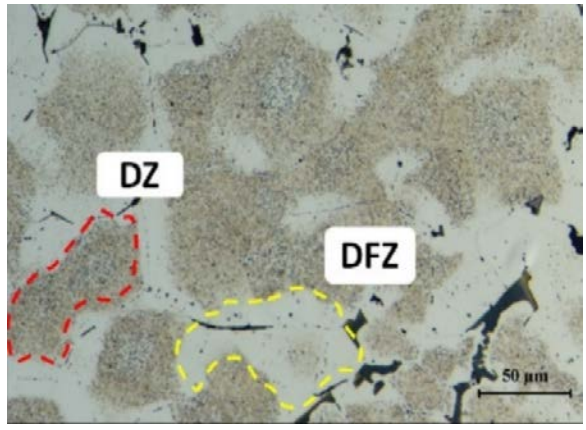

Fig. 2-2: Optic micrograph obtained from typical microstructure of Al-5Mg-0.7Mn alloy after the heat treatment at 500 ℃ indicating dispersoid zone (DZ) and dispersoid free zone (DFZ) [9].

2.4 Homogenization treatment

The as-cast ingots are not uniform due to chemical and structural inhomogeneities. As a result, a wide microsegregation and coring occurs across the aluminium matrix. Such features are prone to material failure under deformation because of their heterogenetic characteristics [2]. Desirable heat treatments are necessary to homogenize the microstructure. In addition to segregation reduction, homogenization also modifies the distribution and morphology of the primary eutectic phases. For example in Al-Mg-Mn alloys, the metastable low temperature solidified phases such as β-Al_8Mg_5 and τ-Al_6CuMg_4 are dissolved or Al_3(Fe,Mn) and Al_m(Fe,Mn) are transformed to stable ones [9]. The stable phases such as Al_6(Fe,Mn) in turn are refined and/or spheroidized to become less harmful for the deformation [2]. Achieving this purpose is complicated and requires a precise design of the homogenization regime based on the proper steps, temperatures, heating/cooling rates, and holding times [10–12].

One noteworthy aspect of homogenization is precipitation of thermally stable submicron intermetallics. These particles so called “dispersoids” are formed in the course of homogenizations through decomposition of low soluble/diffusivity supersaturated transition

elements (such as Mn, Fe, Cu) [13–17]. The precipitation takes place at the grain interiors since the grain boundaries are solute depleted due to the large intermetallic formation through consumption of the alloying atoms (Fig. 2-2). Dispersoids are important since they own an effective mechanism in improving fracture toughness of aluminum alloys at elevated temperature [18]. They hinder the dislocation and grain boundary movement and stabilize the substructure [19]. Such properties make dispersoid a prominent component with an inevitable influence on the microstructural evolutions during hot deformation [20]. Dynamic recrystallization suppression through Zener drag force on migrating grain boundaries is one good example [21]. The distribution and the evolution of dispersoids are influential on the material stability in the course of hot deformation [10]. In the Al-Mg-Mn alloys, there is an important aspect up on the characteristics of the dispersoids in terms of volume, size, morphology, type, and composition [22]. The final products of Al-Mg-Mn alloys are very sensible to the grain structure and texture of the sheets which in turn are function of the interaction between sub-micron intermetallics and the grain evolution [23,24]. Therefore, the characteristics of the particles are signified since each type and distribution can affect specifically [25].

2.5 Hot rolling process

2.5.1 Basics and fundamentals

Hot rolling is a major fabrication process in the sheet production procedure that opens up the possibility of significantly decreasing the thickness of the cast ingots [4] (Fig. 2-3). Its main objective is to provide a uniform shape, thickness, and finished surface strips for the feed stock of cold rolling operation [2]. The industrial details are not the focus of this study considering that the configuration of the rolling line is an intricated art and depends on numerous parameters. Briefly, a general setup consists of roughing and finishing rolling stands which are employed for the primary breakdown and final thickness operations, respectively [26].

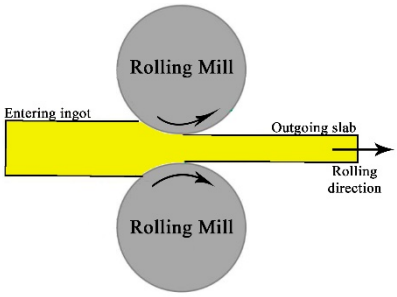

Fig. 2-3: A schematic of a rolling process

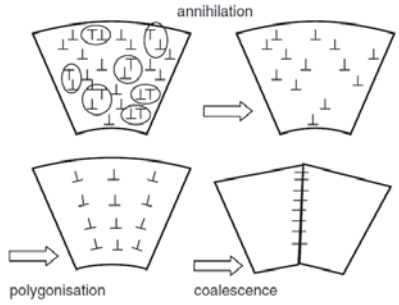

Fig. 2-4: Schematic of dislocation evolution during the dynamic recovery [19]

Throughout conventional rolling, the microstructure alters by complicated mechanisms which occur concurrently or one after other. Generally, the equiaxed as-cast to the elongated compact grain structure is the major impact of rolling that leads to diminishing of any internal porosities caused by casting process [26]. Also, primary intermetallics are crushed and distributed thoroughly. Such a deformation must be performed at the highest possible temperature to lower the applied load [26]. The grain structure undergoes a significant evolution through generation of new grains at: 1) during the deformation (Dynamic recrystallization: DRX) and 2) intervals between each milling operation (Static recrystallization: SRX) [23,27]. Both phenomena are of high importance for the properties' control, where the former is way complex due to the dynamic nature and limits of the in-situ studies. Therefore, it elaborates the prediction of the material's behavior which requires deep knowledge of the challengeable hot deformation behavior [28].

2.5.2 Edge crack of hot rolled slabs

Edge crack is a fractural failure that occurs during the hot rolling process of ingots at the edges and its detrimental features reduce the productivity (Fig. 2-5) [29]. The longitudinal tension imposes tensile force near the edges while the centre of the rolling slab is principally deformed in plain strain compression [30]. In a multi pass schedule in materials with low ductility, the tensile stresses are sufficient to form edge cracks. Edge cracking of Al-Mg alloys is a disputable subject on which an extensive survey in the literature have been carried out [31–37]. From the metallurgical aspect, the microstructural characteristics of the ingots directly affect the edge crack formation. The edge of ingots are more susceptible to

cracking due to the inverse segregation and porosities near the outer surface [35]. Both hydrogen and sodium found to be tailored to the edge crack initiation [35]. However, the mechanism of each and the evolution of microstructural components with crack generation needs to be well understood [35].

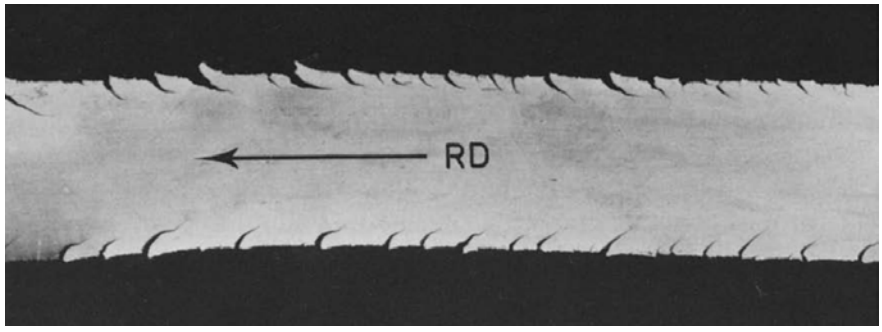

Fig. 2-5: Typical edge cracks distributed at both sides of a slab of aluminum alloy. Observation is normal to the rolling direction [29]

2.6 Hot deformation principals

The ductility at the ambient temperature has limits for pure and multiple phase metal alloys. This is due to the strengthening effect of the progressive work hardening by deformation [27]. Thus, thoughts have turned to elevate the forming temperatures [38]. It is a general trend that when the temperature increases, the flow stress required for the deformation decreases with a corresponding increase in the elongation to failure [28]. This links to the easy motion of the dislocations on the dense atomic plains and in the dense atomic directions (slip systems) [39]. In such a condition, dislocations break away from tangling. Consequently, easy flow behavior of the material is promoted and is governed by either or both dynamic recovery (DRV) [39] and dynamic recrystallization (DRX) [40] mechanisms. On the other hand, if the deformation condition does not support the dislocation slip on all slip systems, material undergoes flow localization mechanisms namely deformation and/or shear bands [41].

2.6.1 Work hardening

Work or strain hardening is a term used to describe the density of the dislocations in a deformed material [42]. Due to the work hardening effect, the flow stress required for the

plastic deformation increases. This is because the multiplication of dislocations leads to their entanglement [42]. Principally, when the crystal structure of a metal is strained, the lattice distortions associated with dislocations and interaction stresses between them reduces their mobility. Consequently, further straining becomes more difficult [42].

Any obstacles in the lattice can increase the work hardenability. The addition of alloying elements in the form of solid solution is one good example [43]. Atomic impurities that go into interstitial or substitutional solid solution cause a strain field linked to the mismatch in atomic size with that of the matrix that acts as a barrier against dislocation motion. Second-phase precipitates also reduce the free slip of dislocations which is significantly affected by size, morphology, volume fraction, and the number density of the particles [22]. Strain hardening is a fundamental strengthening mechanism for non-heat treatable alloys such as Al-Mg-Mn systems that may be achieved by several ways as dislocation tangles, cells and sub-grain walls formation, the change in the shape of grains and internal structures [43].

2.6.2 Dynamic Recovery (DRV)

The term “dynamic recovery (DRV)” refers to the phenomenon in which microstructural defects such as dislocations and interfaces imposed by the plastic flow are restored again to the original homogenous state [39]. A schematic graph of Fig. 2-4 illustrates two main dynamic recovery features which are annihilation and polygonization of dislocations that leads to the reduction of dislocation density [39]. The essential driving force for occurrence of DRV is the thermal activation energy provided by elevating the temperature. Plus, when straining is slow, the mobile dislocations have more time to rearrange and/or annihilate [28]. Therefore, higher temperature and lower strain rates promote DRV [39]. DRV decreases stress concentration on grain boundaries, hence, increases ductility [44]. Dispersoids and solute atoms effectively reduce DRV due to the substructure dislocation stabilization [44].

2.6.3 Dynamic Recrystallization (DRX)

Due to the high stacking fault energy of aluminum, DRV at high temperatures monotonically increases to enhance the straining and ductility [28]. In particular deformation conditions in which the restoration is not possible by DRV, the stored energy related to the dislocation tangling is eliminated via DRX resulting in new grains nucleation [45–48]. The

DRX phenomenon is categorized based on the characteristics of grain structure to discontinues (DDRX), continues (CDRX), and geometric (GDRX) dynamic recrystallization schematically shown in Fig. 2-6 [45]. Also, the microstructural manifestation of each mechanism by means of Electron Backscattering Diffraction (EBSD) was exemplified in Fig. 2-7 [49]. When the DDRX is operating on the microstructure, on the wavy original grain boundaries (GBs) which are serrated due to the applied stress, new grains nucleate at the local bulges and then grow up by the migration of GBs (Fig. 2-7a-b). If only DDRX is active, a neckless structure of grains forms on the original boundaries (Fig. 2-6) [21,45,50]. During the microstructural evolution in CDRX, a continuous rotation of subgrains due to the transition of low angle grain boundaries (LABs) into high angle grain boundaries (HABs) takes place. In this mechanism, no distinct stage of nucleation or growth is distinguishable and a uniform structure of the new grains and subgrains is observed through the material (Fig. 2-6 and Fig. 2-7c-d) [21,45,50]. In GDRX, in the course of straining at elevated temperatures, the grain boundaries become serrated and the thickness of initial grains decreases enormously to touch an approximation of subgrain size where new grains impinge and a uniform structure of recrystallized grains forms (Fig. 2-6 and Fig. 2-7e-f) [21,45,50]. Moreover, it is possible that due to incompatibility of particle plasticity with that of matrix, new grains nucleate at the vicinity of constituent intermetallics [51]. The nucleation of recrystallization originates close to the interface of particle and matrix and consumes the stored energy by new boundary migration and grain growth [21,45,50]. An example of this phenomenon which is called particle stimulated dynamic recrystallization (PSN-DRX) is illustrated in Fig. 1-7g-h [52].

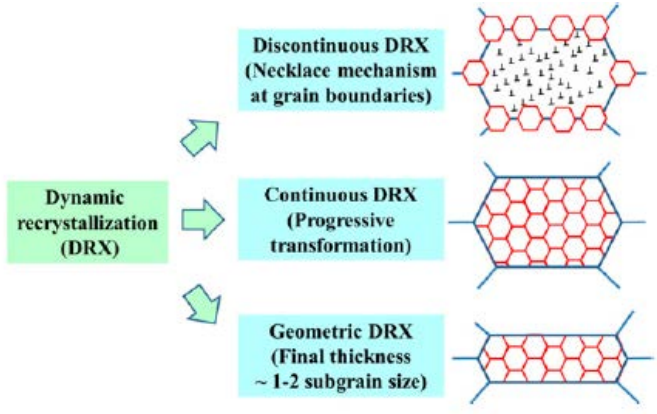

Fig. 2-6: Schematic of the three principal dynamic recrystallization formation in aluminum alloys [45]

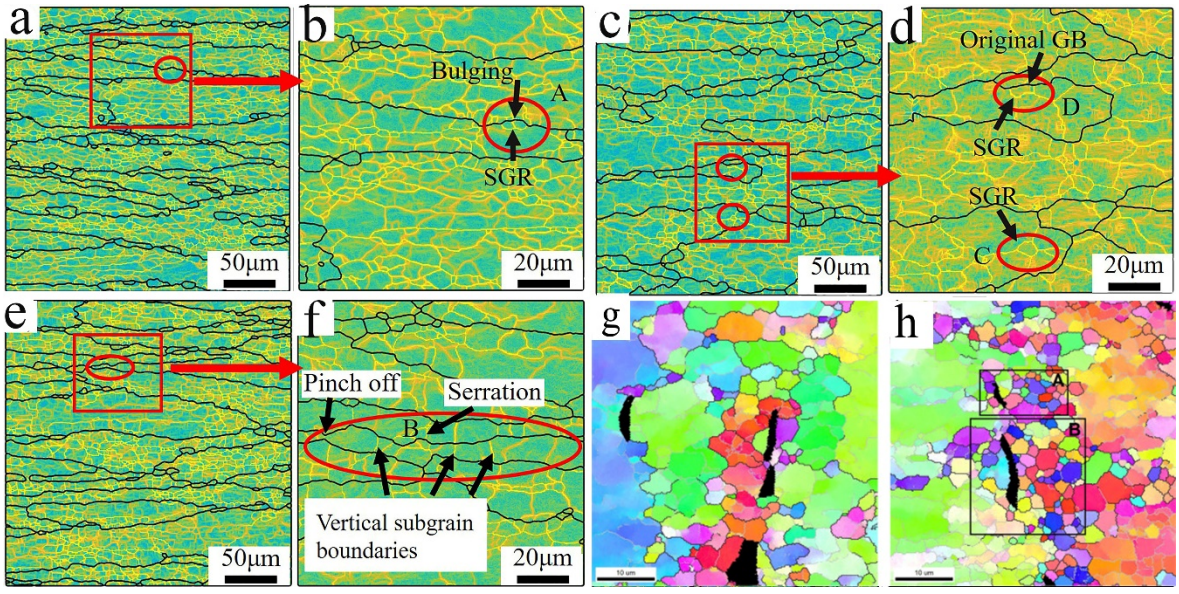

Fig. 2-7: EBSD results (Geometrically Necessary Dislocation maps) of three typical DRX mechanisms in aluminum alloys, (a)(b) DDRX, (c)(d) CDRX, (e)(f) GDRX. The black lines mark high angles (15°<) and yellow lines medium/low angles (< 15°) [49] (g)(h) PSN-DRX exhibited by IPF map, black regions are the intermetallics [52].

2.6.4 Hot deformation instability

Instable deformation is defined by occurrence of nonuniform defective microstructure during the deformation [53]. The plastic instability mechanisms are very important for differentiating the “safe” from “unsafe” deformation conditions during hot working procedures. Received considerable attentions in several studies, namely wedge cracks [54] (Fig. 2-8a), flow localizations [55], adiabatic shear bands (ASBs) [55] deformation bands (DBs) [54] (Fig. 2-8b), and microcracks [56] are known to be the hot workability failure structural defects. The adiabatic shear bands and deformation bands are two principal instability mechanisms frequently observed to endanger the plasticity of aluminum alloys at elevated temperatures [57,58]. The premier [59] is characterised by non-crystallographic bandlike narrow regions of highly concentrated flow across many grains. The latter is the broken up fragments of an individual grain, occurred in order to accommodate the applied strain when the deformation conditions are not suitable for the contribution of enough slip systems in grain [41]. Accordingly, shear bands consist of ultra-fine grains (up to 500nm) generated by local heat at the highly distorted regions and deformation bands are subdivided regions of a grain with almost high uniform misorientation from elsewhere in the grain [41].

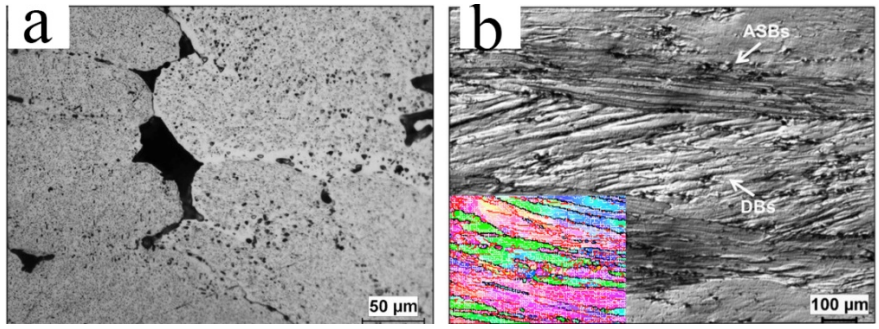

Fig. 2-8; Typical examples of (a) wedge cracking, and (b) deformation and shear bands in the aluminum alloy under optical microscope. The inset of figure b is deformation bands shown by EBSD analysis [54].

2.7 Hot deformation of Al-Mg-Mn alloys

During hot deformation of Al-Mg alloys, the work hardening effect is depleted by softening mechanisms resulted in thermodynamically stabilization of the material. The principal softening mechanism in Al-Mg alloys is DRV due to the high stacking fault energy of aluminum [22]. DRV at elevated temperatures monotonically increases to enhance the straining and the ductility [27] as observed for example in hot deformation of commercial Al [60]. Dynamic recrystallization has been already shown to occur in Al-Mg-Mn alloys [61,62] at temperatures above 400°C [62]. In AA5083 (Al-5Mg-0.7Mn) alloy, Blum et. al. [61] observed that GDRX is the main mechanism through pinching-off of the grain following an extensive DRV. Ding et. al. [52] believe that DRX is generated at the serrated grain boundaries via nucleation and growth and/or through the particle stimulated nucleation dynamic recrystallization (PSN-DRX) in the vicinity of Mn-containing particles over 2 µm in size. Jeong et. al. demonstrated that DRX in Al-Mg system is composition dependent where CDRX as the most frequent mechanism alters to DDRX if Mg increases from 5 to 10 wt.% [63].

2.8 Mn in hot deformation of Al-Mg-Mn systems

The control of material stability basically necessitates detailed knowledge on the microstructure evolution during the thermomechanical process. This in turn links to the alloy's chemical composition. In the Al-Mg-Mn systems, Mn is one of the key elements essential to enhance the strength via solid solution and Mn-rich fine dispersoids

strengthening [5]. Manganese in solid solution impedes dislocation slip due to the individual atom misfit in lattice [64]. It also has a synergic effect via clustering with trace elements to increase the pinning effect, thus increasing the tensile strength [64]. In the same manner, the solute drag effect prevents the dislocation motion and suppresses DRV in plastic deformation at elevated temperatures [65]. The thermally stable Mn-containing dispersoids precipitated during homogenization also retard grain boundary migration, hence, play a prominent role in DRX inhibition [22].

2.9 Constitutive and processing analysis

The constitutive model is widely used to describe the change in mechanical response during hot deformation. The reason is that material flow behavior during hot forming is the function of several factors including stress, strain, strain rate, temperature, and microstructural features [27]. Therefore, prediction of the hot deformation behavior is often a very complex operation. An accurate constitutive model helps to overcome this issue. It has advantages for rolling mill designing [66] and can be integrated into the codes for numerical simulation or embedded in commercial hot forming analysis software [67]. By employing the thermo-mechanical parameters into the plasticity model, the behavior of the alloy is precisely described. Of course, it is crucial to choose a proper constitutive model. The constitutive models are categorized into: (1) phenomenological constitutive, (2) physically-based constitutive, and (3) artificial neural network models. Phenomenological constitutive models has less complexity of mathematical formulization and are widely used for aluminum alloys [20,48,54,68–70]. They are described in terms of experimental data driven from stress-strain flow curves employed in mathematical formulas.

2.9.1 Flow curves

Hot compression test under a certain domain of temperature and strain rate is a common investigating method of hot deformation behavior of a material [27]. Through compressive deformation by computerized equipment, a series of load-displacement data is acquired from which the stress-strain curves are generated. The tendency of the experimentally determined stress-strain flow curves varies by thermomechanical conditions.

In general, the flow behavior of material consists of work hardening and strain softening stages. It is frequently observed that stress-strain curves of aluminum alloys follow three trends of Fig. 2-9. The flow stress initially increases rapidly to a point due to work hardening from which it: (a) increases slightly, (b) exhibits firstly a decline followed by a steady-state stress, (c) declines moderately to the end of the test. The trend indicates specific characteristics of the material microstructural evolution. The inclination signals the prominent work hardening while the steady state and/or declination of the curve links to either or both DRV and DRX [28].

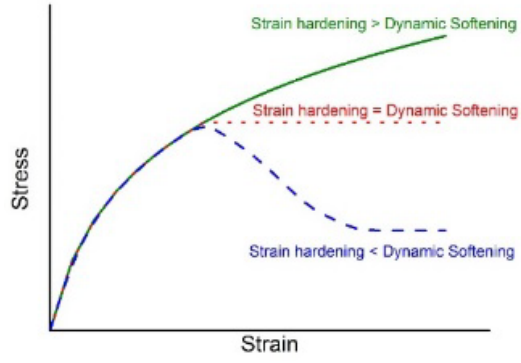

Fig. 2-9: General trend variations of flow curves correlated to the microstructural evolution

2.9.2 Constitutive equations

One of the popular phenomenological models applied for aluminum alloys is Arrhenius type equation [71]. This equation is formulated as:

$$\dot{\varepsilon} = Af(\sigma)\, exp\left(-\frac{Q}{RT}\right) \qquad \text{Eq. 2-1}$$

where $\dot{\varepsilon}$ is strain rate (s^{-1}), A is material constant, Q is activation energy (kJ/mol), R is universal gas constant equal to 8.314 (J/Kmol) and T is temperature (K). The flow stress function f(σ) is expressed in three forms:

(1): $f(\sigma) = \sigma^{n_1}$ Eq.2-2

(2): $f(\sigma) = exp(\beta\sigma)$ Eq. 2-3

(3): $f(\sigma) = [sinh(\alpha\sigma)]^n$ Eq. 2-4

Generally, Eq.2-2 (power law) and Eq. 2-3 (exponential) equations break down at high and low stress values, respectively. However, the hyperbolic-sine law (Eq. 2-4) is proper for constitutive analysis over a wide range of temperatures and strain rates [66].

Furthermore, investigating the simultaneous impact of thermomechanical parameters (i.e. T and $\dot{\varepsilon}$) on hot deformation requires a unit factor. That is because increase in strain rate increases the flow stress while increase in temperature performs conversely. To merge the contribution of both, Zener-Hollomon parameter was defined [72]. In another word, with Z value augmentation temperature and strain rate decrease and increase, respectively. The equation is presented as:

$$Z = \dot{\varepsilon}\, exp\left(-\frac{Q}{RT}\right) \qquad \text{Eq. 2-5}$$

2.9.3 Processing maps

The hot processing map is a method stablished on the dynamic materials model (DMM) [73]. The theory behind was developed on the basis of a system which transforms the power into different states [73]. Accordingly, when a workpiece is deformed, the external energy imposed by the source of power (deformation instrument) can be consumed either as the energy used for the microstructural evolution or released as heat [73]. The total dissipated power P, as expressed in Eq. 2-1 can be composed of parameters G and J. The constant G is the energy required for plastic deformation, which is dissipated as deformation heat, while the constant J is the energy for the mechanisms of material deformation and phase transitions [73].

$$P = \sigma\dot{\varepsilon} = G + J = \int_0^{\dot{\varepsilon}} \sigma d\dot{\varepsilon} + \int_0^{\sigma} \dot{\varepsilon} d\sigma \qquad \text{Eq. 2-6}$$

where $\dot{\varepsilon}$ is strain rate (s^{-1}) and σ is stress (MPa). The efficiency of power dissipation (η) represents the intrinsic energy dissipated by the microstructural evolution during hot deformation which is defined as:

$$\eta = \frac{J}{J_{max}} = \frac{P-G}{J_{max}} = 2\left(1 - \frac{1}{\sigma\dot{\varepsilon}}\int_0^{\dot{\varepsilon}} \sigma d\dot{\varepsilon}\right) \qquad \text{Eq. 2-7}$$

where J_{max} is the maximum value equal to P/2. In this model, partitioning of G and J can be given by the strain rate sensitivity (m) as follows:

$$m = \left[\frac{\partial J}{\partial G}\right]_{\varepsilon,T} = \left[\frac{\partial ln\sigma}{\partial ln\dot{\varepsilon}}\right]_{\varepsilon,T} \quad \text{Eq. 2-8}$$

The m values are extracted from the slope of the $ln\sigma - ln\dot{\varepsilon}$ plot for each temperature and strain rate. From Eq. 2-8, it follows that the dynamic constitutive equation is of the type:

$$\sigma = K\dot{\varepsilon}^m \quad \text{Eq. 2-9}$$

Subsequently, via combination of Eq. 2-6 and Eq. 2-9, J can be expressed as:

$$J = \sigma\dot{\varepsilon} - \int_0^{\dot{\varepsilon}} \sigma d\dot{\varepsilon} = (\sigma\dot{\varepsilon})(\frac{m}{m+1}) \quad \text{Eq. 2-10}$$

Then Eq. 2-10 can be rewritten as:

$$\eta = \frac{J}{J_{max}} = \frac{(\sigma\dot{\varepsilon}\times(\frac{m}{m+1}))}{(\frac{\sigma\dot{\varepsilon}}{2})} = \frac{2m}{m+1} \quad \text{Eq. 2-11}$$

The typical variation of η values that is intrinsically favored for the hot workability is associated with dynamic recovery (DRV) and dynamic recrystallization (DRX) and proposed to be below 20% and above 30%, respectively [74].

Another criterion that Prasad et. al. [73] developed to constitutively express the material behavior is the flow instability which is dimensionless parameter defined as:

$$\xi(\dot{\varepsilon}) = \frac{\partial ln[m/(m+1)]}{\partial ln\dot{\varepsilon}} + m < 0 \quad \text{Eq. 2-12}$$

In the instability regions including adiabatic shear bands, flow localization regions, flow rotation, and kinking which are characterized by the negative $\xi(\dot{\varepsilon})$ values, failure is highly predictable thus deformation processing is undesirable [73].

2.10 Description on edge cracking by Na in Al-Mg alloys

In Al-Mg alloys, trace sodium has a significant deteriorating influence. Sodium contamination is unavoidable in industrial practice since Na is difficult to be eliminated from Mg added to Al-Mg alloys [31]. Na impurities may segregate at the grain boundaries to elevate the embrittlement from where the crack is generated [75]. Thomson and Burman [35] reported that sodium involves in grain boundary decohesion if adsorbed at the pores formed by hydrogen. However, the nature of such interaction was not determined. Later, Lu et. al. [32] proved the responsibility of sodium in Al intergranular embrittlement via grain boundary weakening even in the absence of hydrogen. Yamada et. al. [33] found that Na atoms segregation at the grain boundaries and promote GB-sliding at higher temperature leading to ductility drop. Zhang et. al. [34] determined that Na atoms intrinsically have decohesive characteristics when it segregates on the GBs. It was also found that sodium creates a gap along the GB where oxidation occurrence causes embrittlement. Through thermodynamic simulation, Zhang et. al. [37] also demonstrated that Na in Al-Mg system forms a phase so-called liquid-2 phase that has a low melting temperature. Following this fact, during hot rolling, liquid-2 may transform to liquid resulting in high-temperature embrittlement and cracking, consequently. In addition, other parameters may attribute reciprocally and synergically to the sodium-induced crack initiation from which rolling temperature, grain structure, intermetallics, and alloying contents are exemplified in the literature [76].

2.11 Intermetallic constituents and crack formation

The macroscopic fracture appearance results from micro-mechanisms occurred in the material. Generally, since the edge cracking takes place at elevated temperatures, ductile fracture mode through void nucleation and growth is dominant [77]. Accordingly, the cavities appear at the stress concentrated locals such as particle-matrix interface or porosities. The cavities grow and coalesce together providing a proper path for crack propagation [78]. Voids can nucleate at the interface of Fe-bearing particles during the hot tensile test of Al- 4.6Mg- 0.5Mn- 0.15Fe at 475℃/ 2×10^{-3} s^{-1} (Fig. 2-10a) [79]. It has been

also reported that higher volume of Mg_2Si particles promotes crack initiation since they were observed to be prone to void nucleation (Fig. 2-10b) [80]. It is worthy to note that the segregation of sodium atoms at the periphery of Mg_2Si intermetallics has been reported in the literature [80,81]. This can be correlated to the role of constituents in edge cracking.

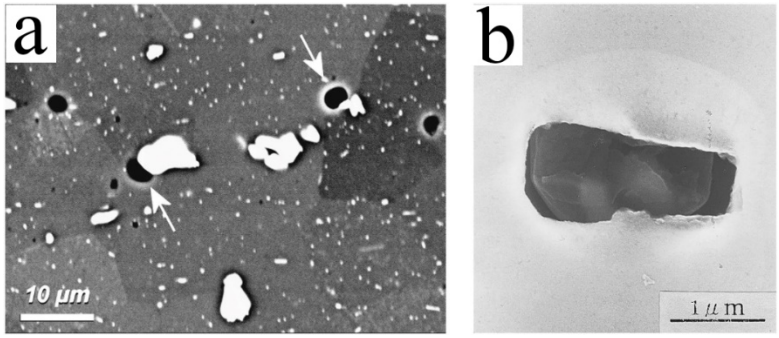

Fig. 2-10: Void nucleation during hot deformation of Al-Mg-Mn alloys on the interface of (a) Fe-[79] and (b) Mg_2Si [80] intermetallics with matrix.

2.12 References

[1] W.M. Mao, G.E. Totten and D.S. MacKenzie, Handbook of Aluminum: Vol. 1: Physical Metallurgy and Processes, Marcel Dekker Inc., 2003.

[2] A. Poznak, D. Freiberg and P. Sanders, Automotive Wrought Aluminium Alloys, in Fundamentals of Aluminium Metallurgy, Elsevier Ltd., 2018, pp. 333–386.

[3] J. Hirsch, Aluminium in Innovative Light-Weight Car Design, Mater. Trans. 52 (2011), pp. 818–824.

[4] J. Hirsch, Aluminium sheet fabrication and processing, in Fundamentals of Aluminium Metallurgy: Production, Processing and Applications, Woodhead Publishing Limited, 2010, pp. 719–746.

[5] J.E. Hatch, Properties of commercial wrought alloys, in Aluminum Properties and Physical Metallurgy, ASM international, 1984, pp. 351–378.

[6] Y.J. Li and L. Arnberg, A eutectoid phase transformation for the primary intermetallic particle from Alm(Fe,Mn) to Al3(Fe,Mn) in AA5182 alloy, Acta Mater. 52 (2004), pp. 2945–2952.

[7] Y.J. Li and L. Arnberg, Solidification structures and phase selection of iron-bearing eutectic particles in a DC-cast AA5182 alloy, Acta Mater. 52 (2004), pp. 2673–2681.

[8] D.G. Eskin, Direct chill casting: Development of the technology, in Physical Metallurgy of Direct Chill Casting of Aluminum Alloys, CRC Press, 2008, pp. 1–17.

[9] A.Y. Algendy, K. Liu and X.G. Chen, Evolution of dispersoids during multistep heat treatments and their effect on rolling performance in an Al-5 % Mg-0 . 8 % Mn alloy, Mater. Charact. 181 (2021), pp. https://doi.org/10.1016/j.matchar.2021.111487.

[10] O. Engler and S. Miller-Jupp, Control of second-phase particles in the Al-Mg-Mn alloy AA 5083, J. Alloys Compd. 689 (2016), pp. 998–1010.

[11] Z. Liu, V. Mohles, O. Engler and G. Gottstein, Thermodynamics based modelling of the precipitation kinetics in commercial aluminium alloys, Comput. Mater. Sci. 81 (2014), pp. 410–417.

[12] O. Engler, Z. Liu and K. Kuhnke, Impact of homogenization on particles in the Al-Mg-Mn alloy AA 5454-Experiment and simulation, J. Alloys Compd. 560 (2013), pp. 111–122.

[13] J. Rakhmonov, K. Liu, P. Rometsch, N. Parson and X.G. Chen, Effects of Al(MnFe)Si dispersoids with different sizes and number densities on microstructure and ambient/elevated-temperature mechanical properties of extruded Al–Mg–Si AA6082 alloys with varying Mn content, J. Alloys Compd. (2020), pp. 157937.

[14] K. Liu, H. Ma and X.G. Chen, Improving the Elevated-Temperature Properties by Two-Step Heat Treatments in Al-Mn-Mg 3004 Alloys, Metall. Mater. Trans. B 49 (2018), pp. 1588–1596.

[15] K. Liu and X.G. Chen, Evolution of microstructure and elevated-temperature properties with Mn addition in Al-Mn-Mg alloys, J. Mater. Res. 32 (2017), pp. 2585–2593.

[16] K. Liu and X.G. Chen, Evolution of Intermetallics, Dispersoids, and Elevated Temperature Properties at Various Fe Contents in Al-Mn-Mg 3004 Alloys, Metall. Mater. Trans. B Process Metall. Mater. Process. Sci. 47 (2016), pp. 3291–3300.

[17] Z. Li, Z. Zhang and X.G. Chen, Improvement in the mechanical properties and creep resistance of Al-Mn-Mg 3004 alloy with Sc and Zr addition, Mater. Sci. Eng. A 729 (2018), pp. 196–207.

[18] K. Liu and X.G. Chen, Development of Al-Mn-Mg 3004 alloy for applications at elevated temperature via dispersoid strengthening, Mater. Des. 84 (2015), pp. 340–350.

[19] X. Qian, N. Parson and X.G. Chen, Effects of Mn content on recrystallization resistance of AA6082 aluminum alloys during post-deformation annealing, J. Mater. Sci. Technol. 52 (2020), pp. 189–197.

[20] X. Qian, N. Parson and X.G. Chen, Effects of Mn addition and related Mn-containing dispersoids on the hot deformation behavior of 6082 aluminum alloys, Mater. Sci. Eng. A 764 (2019), pp. DOI:10.1016/j.msea.2019.138253.

[21] F.J. Humphreys, G.S. Rohrer and A. Rollette, Recrystallization of Two-Phase Alloys, in Recrystallization and Related Annealing Phenomena, Elsevier Ltd, 2017, pp. 285–319.

[22] H.J. McQueen, S. Spigarelli, M.E. Kassner and E. Evangelista, Hot Working of Dispersoids and Solute Alloys, in Hot Deformation and Processing of Aluminum Alloys, CRC Press, 2011, pp. 143–183.

[23] O. Engler and J. Hirsch, Control of recrystallisation texture and texture-related properties in industrial production of aluminium sheet, Int. J. Mat. Res. 100 (2009), pp. 564–575.

[24] O. Engler, L. Löchte and J. Hirsch, Through-process simulation of texture and properties during the thermomechanical processing of aluminium sheets, Acta Mater. 55 (2007), pp. 5449–5463.

[25] The double-edge effect of second-phase particles on the recrystallization behaviour and associated mechanical properties of metallic materials. Elsevier Ltd, 2018.

[26] R.V.P. Singh, Introduction to Hot Rolling, Cold Rolling, Foilrolling, and Basic Philosophy of Product Quality Control, in Aluminum - Rolling: Process Principles and Applications, TMS, 2000, 2011, .

[27] H.J. McQueen, S. Spigarelli, M.E. Kassner and E. Evangelista, Metal foming and deformation modes, in Hot Deformation and Processing of Aluminum Alloys, Taylor & Francis Group, 2011, pp. 21–47.

[28] F.J. Humphreys, G.S. Rohrer and A. Rollette, Hot Deformation and Dynamic

Restoration, in Recrystallization and Related Annealing Phenomena, Elsevier Ltd, 2017, pp. 415–450.

[29] B. Dodd and P. Boddington, The causes of edge cracking in cold rolling, J. Mech. Work. Technol. 3 (1980), pp. 239–252.

[30] M.M. Al-Mousawi, A.M. Daragheh and S.K. Ghosh, A data base for some physical defects in metal forming processes, Stud. Appl. Mech. 43 (1995), pp. 387–400.

[31] K. Horikawa, S. Kuramoto and M. Kanno, Intergranular fracture caused by trace impurities in Al-5.5mol %Mg alloy, Acta Mater. 49 (2001), pp. 3981–3989.

[32] G.H. Lu, Y. Zhang, S. Deng, T. Wang, M. Kohyama, R. Yamamoto et al., Origin of intergranular embrittlement of Al alloys induced by Na and Ca segregation: Grain boundary weakening, Phys. Rev. B - Condens. Matter Mater. Phys. 73 (2006), pp. 1–5.

[33] H. Yamada, K. Horikawa and H. Kobayashi, Effect of trace sodium on high temperature embrittlement in quasi-static and impact deformation of Al–5 mass% Mg alloys, J. Japan Inst. Light Met. 60 (2010), pp. 31–35.

[34] S. Zhang, O.Y. Kontsevoi, A.J. Freeman and G.B. Olson, Aluminum grain boundary decohesion by dense sodium segregation, Phys. Rev. B - Condens. Matter Mater. Phys. 85 (2012), pp. 1–8.

[35] P. Thomson and N. Burman, Edge cracking in hot-rolled Al-Mg alloys, Mater. Sci. Eng. 45 (1980), pp. 95–107.

[36] N.M. Burman and P.F. Thomson, Edge cracking and profile of hot rolled aluminum slabs, J. Mech. Work. Technol. 13 (1986), pp. 205–217.

[37] S. Zhang, Q. Han and Z.K. Liu, Fundamental understanding of Na-induced high temperature embrittlement in Al-Mg alloys, Philos. Mag. 87 (2007), pp. 147–157.

[38] F. Shehata, M.J. Painter and R. Pearce, Warm forming of aluminium/magnesium alloy sheet, J. Mech. Work. Technol. 2 (1978), pp. 279–290.

[39] F.J. Humphreys and M. Hatherly, Recovery after Deformation, in Recrystallization and related annealing phenomena, Elsevier, 2004, pp. 211–213.

[40] F.J. Humphreys and M. Hatherly, Recrystallization of Single-Phase Alloys, in Recrystallization and Related Annealing Phenomena, 2004, pp. 215–IV.

[41] F.J. Humphreys and M. Hatherly, The Deformed State, in Recrystallization and Related Annealing Phenomena, Elsevier Ltd., 2004, pp. 11–65.

[42] J.E. Hatch, work hardening, recovery, recrystallization, and grain growth, in Aluminum Properties and Physical Metallurgy, ASM international, 1984, pp. 105–133.

[43] A.F. Padilha and R.L. Plaut, Work Hardening, recovery, recrystallization, and grain growth, in Handbook of Aluminum: Alloy production and materials manufacturing, G.E. Totten and D.S. MacKenzie, eds., Marcel Dekker Inc., 2003, pp. 193–220.

[44] H.J. McQueen, S. Spigarelli, M.E. Kassner and E. Evangelista, Precipitation Hardening Alloys, in Hot Deformation and Processing of Aluminum Alloys, CRC Press, 2011, pp. 191–233.

[45] K. Huang and R.E. Logé, A review of dynamic recrystallization phenomena in metallic materials, Mater. Des. 111 (2016), pp. 548–574.

[46] G.A. Henshall, M.E. Kassner and H.J. McQueen, Dynamic restoration mechanisms in Al-5.8 At. Pct Mg deformed to large strains in the solute drag regime, Metall. Trans. A 23 (1992), pp. 881–889.

[47] H.J. McQueen and O.C. Celliers, Review application of hot workability studies to extrusion processing : part II. microstructural development and extrusion of Al , Al-Mg , and Al-Mg-Mn alloys, Can. Metall. Q. 35 (1996), pp. 305–319.

[48] C. Shi, J. Lai and X.G. Chen, Microstructural evolution and dynamic softening mechanisms of Al-Zn-Mg-Cu alloy during hot compressive deformation, Materials (Basel). 7 (2014), pp. 244–264.

[49] J. Li, X. Wu, L. Cao, B. Liao, Y. Wang and Q. Liu, Hot deformation and dynamic recrystallization in Al-Mg-Si alloy, Mater. Charact. 173 (2021), .

[50] T. Sakai, A. Belyakov, R. Kaibyshev, H. Miura and J.J. Jonas, Dynamic and post-dynamic recrystallization under hot, cold and severe plastic deformation conditions, Prog. Mater. Sci. 60 (2014), pp. 130–207.

[51] R.D. Doherty, D.A. Hughes, F.J. Humphreys, J.J. Jonas, D. Juul Jensen, M.E. Kassner et al., Current issues in recrystallization: A review, Mater. Sci. Eng. A 238 (1997), pp. 219–274.

[52] S. Ding, S.A. Khan and J. Yanagimoto, Constitutive descriptions and microstructure evolution of extruded A5083 aluminum alloy during hot compression, Mater. Sci. Eng. A 728 (2018), pp. 133–143.

[53] M. Xiong, Z. Weidong, S. Yu, Z. Yongqing, W. Shaoli and Z. Yigang, A Comparative Study of Various Flow Instability Criteria in Processing Map, Rare Met. Mater. Eng. 39 (2010), pp. 756–761.

[54] C. Shi and X.G. Chen, Hot Workability and Processing Maps of 7150 Aluminum Alloys with Zr and V Additions, J. Mater. Eng. Perform. 24 (2015), pp. 2126–2139.

[55] B. Ke, L. Ye, J. Tang, Y. Zhang, S. Liu, H. Lin et al., Hot deformation behavior and 3D processing maps of AA7020 aluminum alloy, J. Alloys Compd. 845 (2020), pp. DOI:10.1016/j.jallcom.2020.156113.

[56] Y. Sun, Z. Cao, Z. Wan, L. Hu, W. Ye, N. Li et al., 3D processing map and hot deformation behavior of 6A02 aluminum alloy, J. Alloys Compd. 742 (2018), pp. 356–368.

[57] Q. Luan, H. Xing, J. Zhang and J. Jiang, Experimental and crystal plasticity study on deformation bands in single crystal and multi-crystal pure aluminium, Acta Mater. 183 (2020), pp. 78–92.

[58] Y. Xu, J. Zhang, Y. Bai and M.A. Meyers, Shear localization in dynamic deformation: Microstructural evolution, Metall. Mater. Trans. A Phys. Metall. Mater. Sci. 39 A (2008), pp. 811–843.

[59] N. Yan, Z. Li, Y. Xu and M.A. Meyers, Shear localization in metallic materials at high strain rates, Prog. Mater. Sci. 119 (2021), pp. DOI:10.1016/j.pmatsci.2020.100755.

[60] H.J. McQueen and W. Blum, Dynamic recovery: sufficient mechanism in the hot deformation of Al (< 99.99), Mater. Sci. Eng. A 290 (2000), pp. 95–107.

[61] W. Blum, Q. Zhu, R. Merkel and H.J. McQueen, Geometric dynamic recrystallization in hot torsion of Al-5Mg-0.6Mn (AA5083), Mater. Sci. Eng. A 205 (1996), pp. 23–30.

[62] H.J. McQueen, E. Evangelista, J. Bowles and G. Crawford, Hot deformation and dynamic recrystallization of Al-5Mg-O.8Mn alloy, Met. Sci. 18 (1984), pp. 395–402.

[63] H.T. Jeong, S.H. Han and W.J. Kim, Effects of large amounts of Mg (5–13 wt%) on hot compressive deformation behavior and processing maps of Al-Mg alloys, J. Alloys Compd. 788 (2019), pp. 1282–1299.

[64] Ø. Ryen, B. Holmedal, O. Nijs, E. Nes, E. Sjölander and H.-E. Ekström, Strengthening mechanisms in solid solution aluminum alloys, Metall. Mater. Trans. A 37 (2006), pp. 1999–2006.

[65] S.G. Song, J.S. Vetrano and S.M. Bruemmer, Pinning effect of solute atoms on grain boundary dislocation dissociation, Mater. Sci. Eng. A 232 (1997), pp. 23–30.

[66] H.J. McQueen and J. Belling, Constitutive constants for hot working of Al-4.5 Mg-0.35 Mn (AA5182), Can. Metall. Q. 39 (2000), pp. 483–492.

[67] Y.C. LIN, S. cun LUO, X. you JIANG, Y. TANG and M. song CHEN, Hot deformation behavior of a Sr-modified Al-Si-Mg alloy: Constitutive model and processing maps, Trans. Nonferrous Met. Soc. China (English Ed. 28 (2018), pp. 592–603.

[68] M. Shakiba, N. Parson and X.G. Chen, Hot deformation behavior and rate-controlling mechanism in dilute Al-Fe-Si alloys with minor additions of Mn and Cu, Mater. Sci. Eng. A 636 (2015), pp. 572–581.

[69] C. Shi and X.G. Chen, Effect of Zr addition on hot deformation behavior and microstructural evolution of AA7150 aluminum alloy, Mater. Sci. Eng. A 596 (2014), pp. 183–193.

[70] A critical review of experimental results and constitutive descriptions for metals and alloys in hot working. Elsevier Ltd, 2011.

[71] H.J. McQueen and N.D. Ryan, Constitutive analysis in hot working, Mater. Sci. Eng. A 322 (2002), pp. 43–63.

[72] C. Zener and J.H. Hollomon, Effect of strain rate upon plastic flow of steel, J. Appl. Phys. 15 (1944), pp. 22–32.

[73] Y.V.R.K. Prasad, H.L. Gegel, S.M. Doraivelu, J.C. Malas, J.T. Morgan, K.A. Lark et al., Modeling of dynamic material behavior in hot deformation: Forging of Ti-6242, Metall. Trans. A 15 (1984), pp. 1883–1892.

[74] K.P. Rao, Y.V.R.K. Prasad and K. Sivaram, Deformation processing map for control of microstructure in Al4Mg alloy, Mater. Lett. 10 (1990), pp. 66–70.

[75] S. Zhang, O.Y. Kontsevoi, A.J. Freeman and G.B. Olson, Sodium-induced embrittlement of an aluminum grain boundary, Phys. Rev. B - Condens. Matter Mater. Phys. 82 (2010), pp. DOI:10.1103/PhysRevB.82.224107.

[76] S.P. Lynch, Comments on Intergranular fracture caused by trace impurities in an Al-5.5 mol% Mg alloy, Acta Mater. 47 (2002), pp. 125–129.

[77] H. Riedel, F. Andrieux, T. Walde and K. Karhausen, The Formation of Edge Cracks during Rolling of Metal Sheet, Steel Res. Int. 78 (2007), pp. 818–824.

[78] G.E. Dieter, H.A. Kuhn and S.L. Semiatin, Bulk Workability of Metals, in Handbook of Workability and Process Design, 2003, pp. 22–39.

[79] H. Jin, Optimization of Aluminum Alloy AA5083 for Superplastic and Quick Plastic Forming, Metall. Mater. Trans. A (2019), pp. 5–7.

[80] H. Hosokawa, H. Iwasaki, T. Mori, M. Mabuchi, T. Tagata and K. Higashi, Effects of Si on deformation behavior and cavitation of coarse-grained Al-4.5Mg alloys exhibiting large elongation, Acta Mater. 47 (1999), pp. 1859–1867.

[81] C.J. Simensen and U. Södervall, Investigation of trace elements in an Al-4.8 wt.% Mg-0.3 wt.% Mn alloy, Surf. Interface Anal. 30 (2000), pp. 309–314.

Chapter 3: Experimental procedure

3.1 Alloys and compositions

The alloys used for the study on the effect of Mn on hot deformation were prepared with pure Al (99.7wt.%), pure Mg (99.9wt.%), Al-25wt.%Mn, Al-25wt.%Fe, and Al-50wt.%Si master alloys. For the composition measured by optical emission spectroscopy (OES) of Table 3-1, approximately 5kg material for each alloy was melted in an electrical resistance furnace. The temperature was kept at 750 ℃ for 30 min and the melt was progressively degassed for 15 mins then poured into a preheated (250℃) permanent steel mold with dimensions of 30mm*40mm*80 mm. To obtain a homogenized microstructure before the deformation test, an industrial imitated heat treatment was applied by a two steps regime: I) 420℃/2h and II) 500℃/4h. The treatment process was designed to obtain the optimum dispersoid distribution by Mn decomposition from solid solution. The homogenized ingots were then machined into cylindrical samples.

Table 3-1: The measured composition of the alloys in the hot deformation study (wt.%)

Alloy	Mg	Mn	Fe	Si	Ti	Al
0.1Mn	4.67	**0.11**	0.26	0.1	0.01	Bal.
0.4Mn	4.65	**0.4**	0.28	0.09	0.01	Bal.
0.7Mn	4.74	**0.74**	0.27	0.09	0.01	Bal.
1Mn	4.7	**1.05**	0.27	0.09	0.01	Bal.

Table 3-2: The measured composition of the alloys in the edge crack study (wt.%)

Alloy	Si	Fe	Cu	Mn	Mg	Ti	Na
High Sodium	0.05	0.14	≤0.05	0.25	4.8	0.023	**0.0001**
Low Sodium	0.06	0.15	≤0.05	0.25	4.8	0.023	**0.00003**

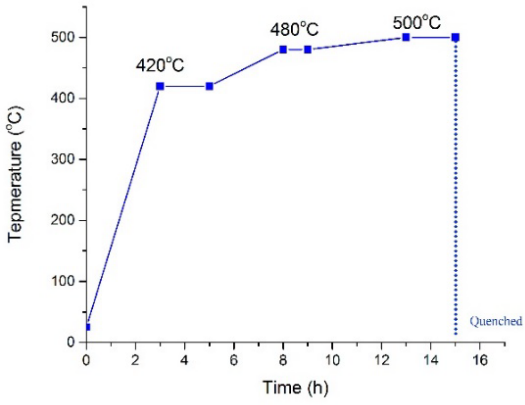

Fig. 3-1: Homogenization regime for the edge crack study

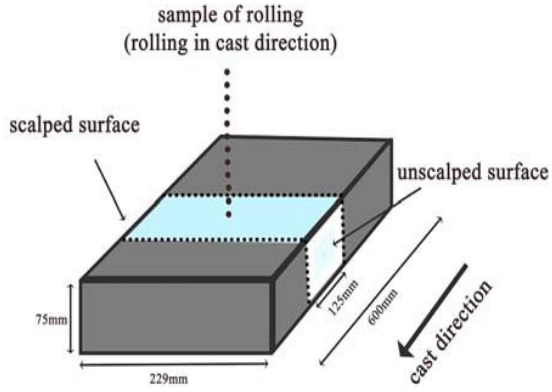

Fig. 3-2: The dimensions of the ingot and the location of the workpiece used for rolling

For the study of edge cracking, two trace sodium contaminated Al-Mg-Mn alloys included 1ppm (high sodium) and <0.5ppm (low sodium) with chemical compositions shown in Table 3-2 casted by Direct Chill method and homogenized based on the regime of Fig. 3-1by the Arvida Research and Development Centre of Rio Tinto Aluminum, Saguenay, QC, Canada. The intention of the two steps at the beginning of the homogenization (i.e. 420℃ and 480℃) was to dissolve the low melting point eutectic intermetallics. Fig. 3-2 shows the dimensions of the rectangular blocks prepared from the cast ingot for the hot-rolling process. Blocks were machined to remove the as-cast surface from their rolling faces (10 mm from each side). One of the short faces of each ingot was also scalped approximately 25 mm off to investigate the effect of subsurface microstructure on edge cracking. The cast surface of the other short face was left intact.

3.2 Deformation test

For the effect of Mn on hot deformation behavior, the hot compression tests were performed at temperatures of 350, 400, 450, and 500℃ at each strain rate of 0.001, 0.01, 0.1, and 1s^{-1} by Gleeble 3800 equipment (Fig. 3-3).

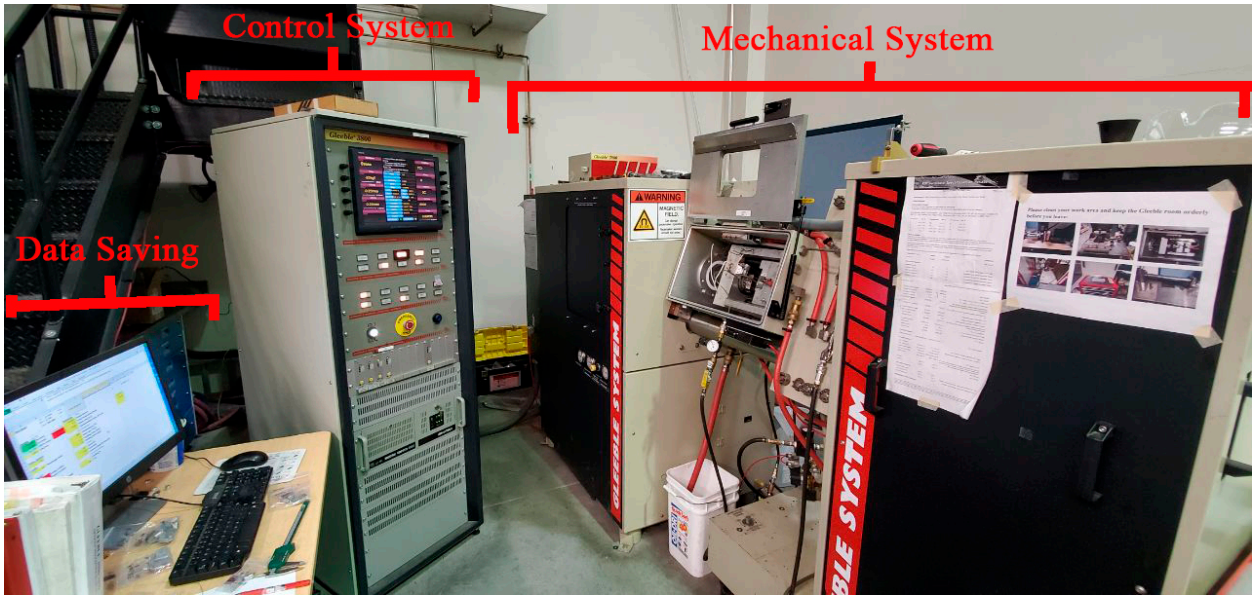

Fig. 3-3: The Gleeble 3800 unit by which the hot compression tests were carried out.

CompressionV5.xlsm - Microsoft Excel

File Home Insert Page Layout Formulas Data Review View Developer

A11 tc2

	A	B	C	D	E	F	G	H	I	J	K	L
1	***Test Detail***	H_{fp} / H_{fs}	**9.944**	**10.144**	mm	Copy program						
2		ΔH_p / ΔH_s	**5.189**	**4.989**	mm							
3		Time	**4.000**		s							
4	***801***											
5	***Sample***			***Parameter***	*Strain*							
6	15.133	**H (mm)**	*Compensated*	LGauge	**Strain Source**							
7	9.750	**D (mm)**	0.4199	0.4	**Total Strain (mm/mm)**							
8	2000	**pts/run**	0.1050	0.1	**Strain rate (s-1)**							
9				0.2	**Compensation (mm, 0 if no)**							
10	***Temp. control***				*Temperature*							
11	tc2			400	**Temperature (°C)**							
12	***Limits***			2.0	**Heat rate (°C/s)**							
13	70	**PowAngle limit**		3.0	**Holding time (min)**							
14				50	**Holding force (kgf)**							
15	***PID HZT***				*Quench*							
16	-24.0%	**extkp (-24%)**		On	**Quench1**							
17	-0.24%	**extki (-0.24%)**		On	**Quench2**							
18	***PID TC***			5.0	**minimal Quench time (s)**							
19	1.00	**tc2kp (1)**			*End of test Cooling*							
20	1.00	**tc2ki (1, clip 0.08)**			**Cooling to**							
21				80	**(°C)**							
22												

Fig. 3-4: Example of the Excel file in which the deformation parameters were defined and the program for deformation was generated

Cylindrical shape samples with diameter of 10 mm and length of 15 mm as shown in Fig. 3-4. was used to study the hot compression test. Before the test starts, two wires were welded on the body of cylinder with an equal distance from the bases. The other ends of these wires were attached to the thermocouple in the unit to progressively control the

temperature. The data required for the test running such as deformation conditions and sample size was inserted in an Excel file named as CompressionV5 (Fig. 3-4). The file was programmed to develop the codes of the control system of Gleeble. According to the code that was used for Gleeble system, the compressive unit is able to follow the deformation procedure. During the test, the parameters must be monitored on the screen of the control system. The most important parameter is the Power Angle which indicates the sustainability of the temperature distribution trough the sample. It is recommended to keep this value below 35%. If it exceeds over 60% the test will be stopped, and if not, the results are not reliable. The cleanness and accuracy of the weld of the thermocouples are very critical to gain a low Power Angle. During the compression, the data received from the simulator was continuously saved in an Origin software file to extract the flow curve. After the test, the results have to be treated to extract the smooth curves. The heat flowed by anvils from two circular bases of the cylinder and increased the temperature. To eliminate the temperature gradient throughout the sample, they were heated up at 2°C/s to reach the desired temperature and kept for 3 min. Subsequent to the temperature stabilization step, samples were compressed to the strain of 0.8 (Fig. 3-4). Each test was replicated at least three times to ensure reproducibility. An automatic water-spray system installed on the unit was used to water quench one sample out of three to reserve the microstructure for further analysis.

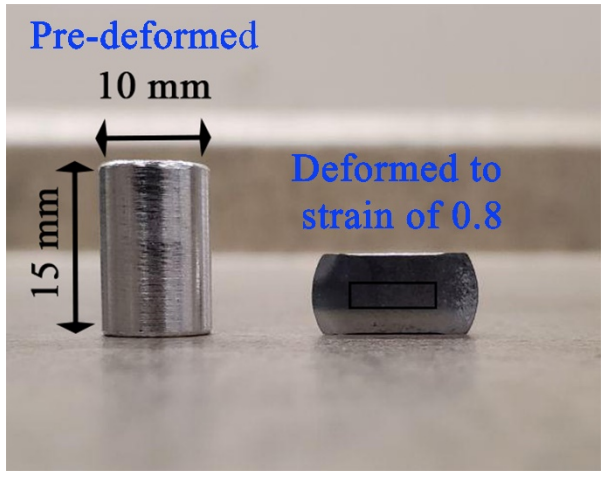

Fig. 3-5: The cylindrical samples used in hot compression tests before and after the deformation

For the edge crack study, 18 consecutive passes were applied directly to the heat-treated blocks. Hot rolling was performed in the 400–500 °C temperature range using a two-high rolling mill with 310 mm diameter rolls. The temperature of the rolled strip was constantly

monitored over 400°C during hot rolling. In between rolling passes, the strip was re-heated to 500 °C when the strip temperature fell below 400 °C. The blocks were rolled down from 75 to 3 mm in thickness, resulting in a 96% reduction in area. After the 11th and 18th passes, sampling was carried out for microstructural characterisation. Pass #11 (plate thickness of 12 mm, 86% area reduction) was the beginning of edge cracking detectable by naked eye and pass #18 (Fig. 3-5) was the end of the rolling process.

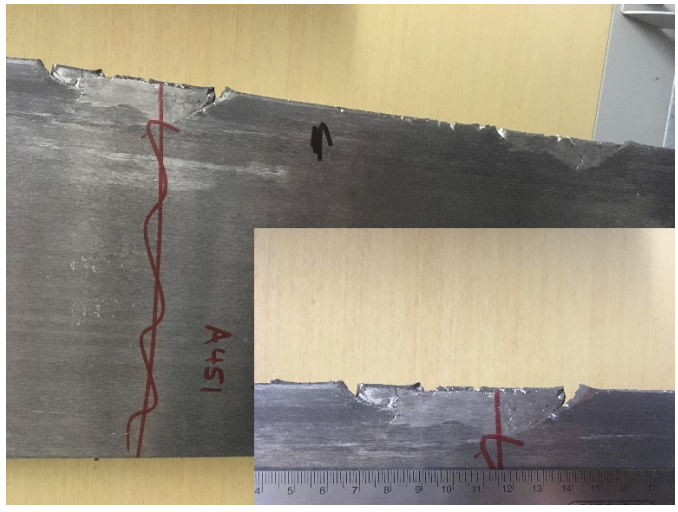

Fig. 3-6: Edge crack of high sodium alloy after 18 passes hot rolling. The inset is the deep cracked region with a scale.

3.3 Microstructure characterization

3.3.1 Sample preparation

Metallographically, samples were ground and polished to characterize their microstructures. Workpieces were cut by means of cutting saws into pieces of below 5 cm. For hot deformation study, sample were cut from the center of an axial section. Followed by mounting, every batch of 6 mounted samples were fixed in a sample holder designed for the machine. The grinding procedure was carried out by Struers wheel grinder/polisher bench (Fig. 3-6). The grinding started with sandpapers of P120 up to P600. The force, speed of rotation, and time were the important parameters to acquire a desirable surface. The force and speed increases as the grinding approaches to the finer steps. For instance, 30 N / 120 rpm at P120 and 40 N / 150 rpm at P600. Time depends on the sample thickness and roughness but usually alters from 2-3 min at the beginning to 3-4 min at the finer steps.

Followed by P600 step, sandpaper was replaced by a pad on which diamond suspension and lubricant were sprayed for the polishing process. The polishing includes three steps in which suspension with particle size of 6, 1, and 0.5 µm was used, each for 5 min. The last step was carried out by white colloidal silica suspension. For the EBSD analysis it was important to prolong the final polishing (0.5µm for 10min) with single sample holder in order to sufficiently flatten the surface. For the in situ-analyses, microindentation was located by Vicker hardness equipment (NG-1000 CCD). Normally three traces of the micro-hardness test under forces of 25-100-200 mN were obtained. These three spots were clearly detectable under optic and scanning electron microscopy.

Fig. 3-7: The polishing unit with a six-sample containing holder

Etching process was used to reveal specific microstructural components of the alloy such as dispersoids and grain boundaries. For the former one, samples simply were soaked in 0.5%HF etchant for 40-60s in the ambient temperature. The latter was detectable after electrochemical etching in Barker's reagent (Setup of Fig. 3-7). For this purpose, 25 mL HBF_4 (40%) was added to 1000 mL distilled water. Samples held by an alligator attached to a wire on one end while the other end was attached to the positive pole of the transformer. The negative pole was attached to a graphite bar held in the solution. For electropolishing, samples were kept in the Barker solution for 3 min at 17 volt.

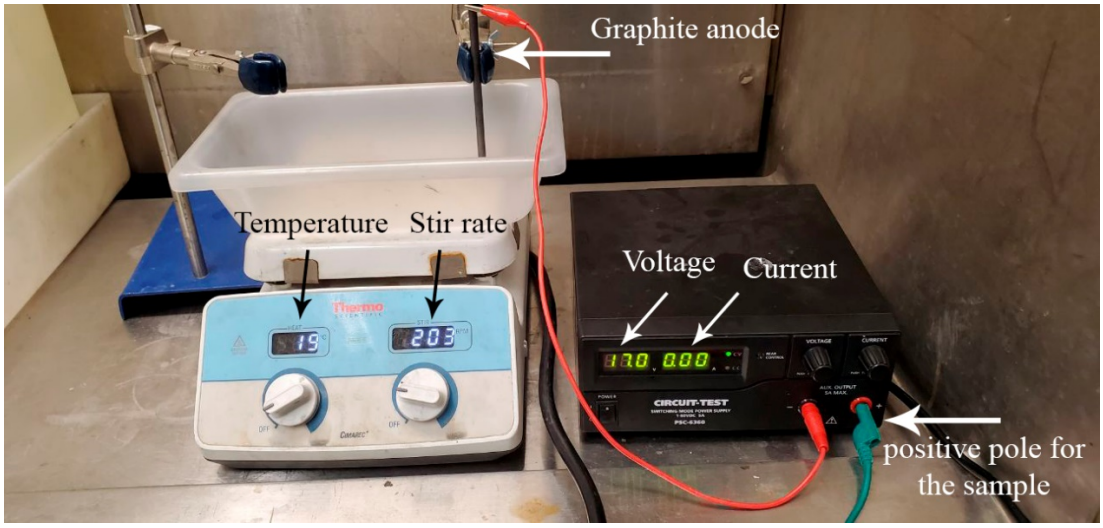

Fig. 3-8: The setup of the electro etching process

For the TEM sample preparation, first, plates with thickness of ~400 µm was provided using the precision cutter. Then disks with 3 mm in the diameter were cut out and mechanically ground to the thickness of ~60 µm. Followed by this step, a twin-jet unit operated at 20 V and -20˚C using a 30% nitric acid and 70% methanol solution was employed to make a whole inside the disk.

3.3.2 Optical microscopy

Optical analyses were carried out by Nikon, Eclipse ME600 optical microscopy equipped to CLEMEX software. To study the constituents and dispersoids, usually 200-500x magnification was suitable while for grain study 50-100x. For grain structure analyses the light was adjusted to polarized option in order to detect the orientation of grain structure.

3.3.3 Scanning Electron Microscopy and EBSD

Scanning electron microscope (SEM, JEOL JSM-6480LV) (Fig. 3-7a) and energy dispersive spectroscopy (EDS) were used to examine microstructure components, including intermetallics and dispersoids. The EBSP data from electron backscattered diffraction analysis (EBSD) at step sizes of 0.1, 0.2, 0.5, and 1 and 0.2 m were used to extract information about grain and subgrain structure. The large and small grain structures are analyzed by high and low step sizes, respectively. To display the orientation maps, first, raw maps with over 80% reliable indexed data points acquisition were provided by HKL

technology. Then Channel 5 Tango software was used to discard poor data through a standard data clean-up or 'noise reduction' procedure of which the points where indexing was not possible or points that have been incorrectly indexed were substituted with copies of the neighboring correct points [1]. With the aid of Tango software, All-Euler, Inverse Pole Figure (IPF), Quality Map (QM), and recrystallization fraction map could be extracted. In order to extract the maps from Tango software, it is necessary to define the grain boundaries manually. The misorientation angles were marked as white, blue, and black for low (LABs: 2°–5°), medium (MABs: 5°-15°), and high (HABs: 15°<) angle boundaries, respectively [2]. To carry out the in-situ comparison between EBSD and OM observation, it was required to do the EBSD first, then optical observation.

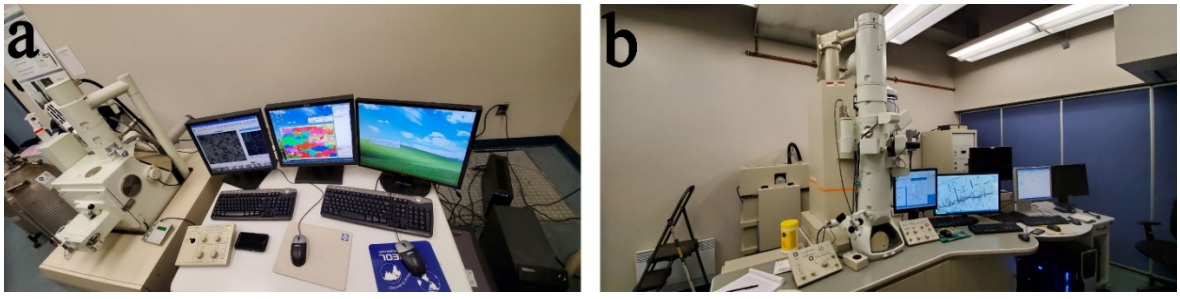

Fig. 3-9: (a) Scanning Electron Microscopy (SEM) and (b) Transmission Electron Microscopy (TEM) used in this study.

3.3.4 Transmission Electron Microscopy (TEM)

Detailed characteristics of the dispersoids and grain boundaries were achieved by TEM analyses. The examination was carried out by JEM- 2100 electron microscope equipped with an EDS system at 200 kV, as shown in Fig. 3-7b. The selected area diffraction patterns (SADPs) of [001] and [011] were suitable to capture dispersoids and dislocations/boundaries, respectively. The composition of the dispersoids was determined by means of TEM-EDS.

3.4 References

[1] V. Randle, *Electron backscatter diffraction: Strategies for reliable data acquisition and processing*, Mater. Charact. 60 (2009), pp. 913–922.

[2] F.J. Humphreys, *Grain and subgrain characterisation by electron backscatter diffraction*, J. Mater. Sci. 36 (2001), pp. 3833–3854

Chapter 4: Effect of Mn Content on the Hot Deformation Behavior and Microstructure Evolution of Al-Mg-Mn 5xxx Alloys

Mohammadreza Mofarrehi, Mousa Javidani, X.-Grant Chen
Department of Applied Science, University of Québec at Chicoutimi, Saguenay, Québec, G7H 2B1, Canada

This manuscript was published in:
Journal of Materials Science and Engineering A

Abstract

The hot deformation behaviors of Al-Mg-Mn 5xxx alloys with different Mn contents (0.1–1 wt.%) were studied by carrying out uniaxial compression tests over the temperature and strain rate ranges of 350–500 °C and 0.001–1.0 s^{-1}, respectively. In the pre-deformed state, Mn dispersoids appeared in the α-Al matrix once the Mn content reached 0.4%. The density of these dispersoids increased with a further increase in the Mn content. The peak flow stress gradually increased with an increase in the Mn content under a given deformation condition owing to the strong strengthening effect of the dispersoids, and the activation energy of hot deformation also increased with increasing Mn content. The deformed microstructures were analyzed using the electron backscatter diffraction technique, and the dominant restoration mechanisms were classified based on the Zener-Hollomon parameter (Z). Under low-Z deformation conditions, continuous dynamic recrystallization (CDRX) was the principal softening mechanism. At intermediate Z values, CDRX was partially accompanied by particle-stimulated and discontinuous DRX. At higher Z values, dynamic

recovery was the only softening mechanism, which was mainly dominated by work hardening.

4.1 Introduction

Al-Mg-Mn 5xxx alloys are extensively used in various industries, such as transportation, construction, and aerospace owing to their high strength-to-weight ratio, excellent weldability, and good corrosion resistance [1–4]. They are suitable for a wide range of applications that require high strength and formability, such as automotive interior panels and components, storage tanks, marine utilization structures, architectural applications, and beverage cans [2]. It is well-known that 5xxx alloys are a class of non-heat treatable aluminum alloys, and with the addition of up to 5 % Mg, these alloys are mainly strengthened by solid solution hardening combined with strain hardening. After thermomechanical processing, these alloys exhibit high strength and good formability.

These alloys are mainly used in rolled sheets and are mainly fabricated through conventional ingot metallurgy via direct chill casting [5] and homogenization followed by hot rolling [6]. During hot rolling, dynamic recovery (DRV) and dynamic recrystallization (DRX) are the principle restoration mechanisms that reduce the work-hardening effect and enhance the formability of alloys. For metals with high stacking fault energy, such as Al, DRV is usually the dominant softening mechanism [7]. By further straining after DRV initiation, the continuous accumulation of dislocations enhances the misorientation angle through which the subgrains are progressively transformed into fine equiaxed grains. This phenomenon is known as continuous dynamic recrystallization (CDRX) [8]. Under conditions where DRV is inhibited, other softening mechanisms may be activated. For example, discontinuous dynamic recrystallization (DDRX) can be initiated by high dislocation density gradients near the initial grain boundaries, leading to subgrain formation followed by local boundary bulging. The bulged grains are surrounded by high-angle grain boundaries (HABs) on one side and sub-boundaries on the other. If the deformation continues, further subgrain rotation increases the misorientation angle to HABs and DDRX grains are formed [9]. New grains can also be formed by the energy stored in the matrix in the proximity of large intermetallic particles. This phenomenon is known as particle-stimulated dynamic recrystallization [10].

Several studies have been conducted on the hot-deformation behavior of Al-Mg-based alloys [11–17]. For instance, McQueen et al. [11] studied the hot deformation of the AA5083

alloy in hot torsion over the temperature range of 300–500°C and found that DRX occurred at 300–500 °C. Haaften et al. [13] investigated the effect of the strain rate on the thermomechanical behavior of the AA5182 alloy by carrying out tensile tests at the strain rates of 10^{-4}–1 s^{-1}, and found that the constitutive behavior was independent of the deformational history over the temperature range of 350–500°C. Jeong et al. [15] studied the effect of the Mg content (5–13 wt. %) on the hot deformation behavior using compression tests, and found that the softening mechanism changed from CDRX to DDRX with an increase in the Mg content beyond 7 %. In addition, the thermomechanical parameters have a considerable impact on the response of a material to deformation. In a recent study by Ding et al. [17], the flow and DRX behaviors of AA5083 alloys with different initial microstructures (extruded and homogenized) were examined by carrying out hot compression tests. The flow curves under the homogenized condition were lower than those under the extruded condition, and the DRX process for the homogenized condition was slower than that for the extruded condition.

Mn is one of the key alloying elements in Al-Mg-based alloys and enhances their mechanical properties by dispersion strengthening and solid solution hardening. Mn is typically added to Al-Mg-based alloys to compensate for the negative effects of Fe. The addition of Mn promotes the transformation of needle-like Al_3Fe intermetallics to Chinese-script $Al_6(Fe,Mn)$ intermetallics during solidification, which have less harmful effect on the mechanical properties of Al-Mg-based alloys [18]. During homogenization, submicron Mn-bearing intermetallics called dispersoids can be formed, which have a significant impact on the deformed microstructure during rolling. Such Mn-bearing dispersoids can inhibit DRV and DRX by pinning the dislocations and retarding the grain-boundary migration [19,20]. Consequently, they may affect the hot formability of Al-Mg-Mn alloys as well as the mechanical properties of the rolled products [21,22]. However, to the best of our knowledge, a systematic investigation on the effect of the Mn content and Mn-bearing dispersoids on the hot deformation behavior of Al-Mg-Mn alloys has not been reported.

The activation energy of hot deformation (Q) is usually an indicator of the degree of difficulty of the plastic deformation of Al alloys. The addition of Mn to Al-Mg-based alloys is expected to enhance their activation energy (Q) [22–24]. However, according to recent studies, Q is not always constant [22]. It may vary with the metallurgical factors (e.g., the

dispersoid size/distribution and area fraction of the dispersoid-free zones (DFZs)) as well as the hot deformation parameters (e.g., temperature and strain rate) [19].

In this study, the effects of the Mn level and Mn-bearing dispersoids on the hot deformation behavior of Al-Mg-Mn alloys were investigated. The microstructures of the alloys during homogenization were studied to characterize the evolution of Mn-bearing dispersoids at different Mn levels. The homogenized samples were subjected to uniaxial hot compression tests to assess their flow behavior and to conduct constitutive analyses. The deformed microstructures, characterized using the electron backscatter diffraction (EBSD) technique, were classified based on the Zener-Hollomon (Z) parameter. Finally, the dominant restoration mechanisms and their correlation with the Mn content were elucidated.

4.2 Experimental procedure

Four Al-5Mg-Mn experimental alloys with 0.1, 0.4, 0.7, and 1 % Mn were investigated. Among these, the alloy containing 0.4 % Mn had a typical AA5182 composition, while the alloys containing 0.7 and 1 % Mn showed the AA5083 composition (all the alloy compositions used in this study were in wt. % unless otherwise indicated). The alloys were prepared in an electrical resistance furnace. The melts were grain-refined by adding 0.015 % Ti in the form of an Al–5Ti–1B master alloy, left for 10–15 min at 700 °C, and cast into a rectangular permanent steel mold with the dimensions of 30 mm × 40 mm × 80 mm. The chemical compositions of the alloys, as determined using optical emission spectroscopy, are listed in Table 4-1. After casting, the ingots were subjected to two-step homogenization in an air circulating furnace, in which the samples were heated to 420 °C for 2 h at the heating rate of 1 °C/min and were then heated up to 500 °C for 4 h followed by water quenching to room temperature.

Table 4-1. Chemical compositions of experimental alloys (wt.%)

Alloy ID	Mg	Mn	Fe	Si	Ti	Al
0.1Mn (base)	4.67	**0.11**	0.26	0.10	0.01	Bal.
0.4Mn	4.65	**0.4**	0.28	0.09	0.01	Bal.
0.7Mn	4.74	**0.74**	0.27	0.09	0.01	Bal.
1Mn	4.7	**1.05**	0.27	0.09	0.01	Bal.

Cylindrical samples with a length of 15 mm and diameter of 10 mm were machined from the homogenized ingots. The samples were subjected to uniaxial compression test at four different temperatures (i.e. 350, 400, 450, and 500 ℃) with at four different strain rates (i.e. 0.001, 0.01, 0.1, and 1 s^{-1}) to a true strain of 0.8 using a Gleeble 3800 thermomechanical testing unit. The specimens were heated with a rate of 2 ℃/s and maintained for 180 s at the desired test temperature to stabilize a uniform temperature distribution before the compression starts. The deformed specimens at the end of each test were rapidly cooled with a spray of water to retain the deformed microstructure.

The metallographic samples were prepared according to a standard metallographic procedure. To examine the dispersoids formed after the homogenization process, the samples were etched for 45 s in a 0.5 % HF solution. To observe the grain structure, electrochemical etching was performed on the polished samples using the Barker's reagent (4 mL HBF_4 + 200 mL H_2O) at 20 V for 90 s. The microstructures of the alloys were characterized using optical microscopy (Nikon, Eclipse ME600) in both the polarized and unpolarized modes and scanning electron microscopy (SEM, JEOL-6480LV). The chemical compositions of the primary and secondary phases were determined using energy-dispersive X-ray spectroscopy (EDS). The pre-deformed grains were measured using the linear intercept method. The deformed samples were sectioned along the compression axis and analyzed using the electron backscattered diffraction (EBSD) with the step sizes of 1, 0.5, and 0.1 μm. The EBSD data were processed using Channel 5 analysis software considering that the data points with low confidence index were discarded. To analyze the grain and subgrain structures, the boundaries and sub-boundaries were defined based on the misorientation angle as low-angle boundaries (LABs: 2-5 °), medium-angle boundaries (MABs: 5-15 °) and high-angle boundaries (HABs: >15 °) [25]. The distribution of dispersoids was examined by a transmission electron microscope (TEM, JEM-2100) operated at 200 kV. To prepare the samples for TEM observation, samples were mechanically ground to a thin disc of 35-60 μm; they were then subjected to electropolishing in a twin-jet unit operated at 20 V and -20 ˚C using a 30 % nitric acid and 70 % methanol solution.

4.3 Results

4.3.1 Microstructure after homogenization

The grain structures of all the four experimental alloys showed equiaxed morphology. Fig. 4-1 shows the typical grain structures of the 0.4 and 1Mn alloys. The average grain sizes of the 0.1 and 0.4Mn alloys were 152 and 148 μm, respectively. With an increase in the Mn content, the grains became finer, and the average grain sizes of the 0.7 and 1Mn alloys decreased to 103 and 91 μm, respectively.

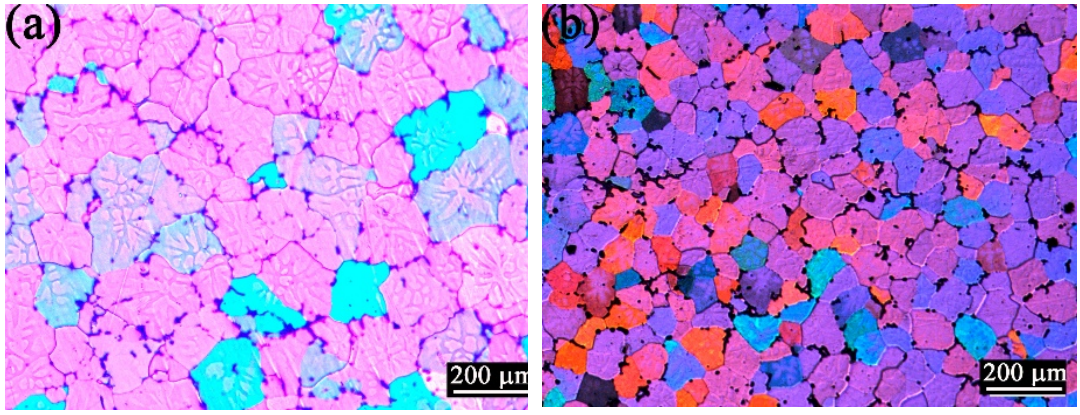

Fig. 4-1 The typical grain structure after homogenization, a) 0.4Mn and b) 1Mn alloys.

The as-homogenized microstructures of the four alloys are shown in Fig. 4-2. The microstructures were composed of the α-Al matrix, primary Mg_2Si, and Fe/Mn-bearing intermetallics located mostly in the dendrite boundaries. The Fe/Mn-rich intermetallics observed in the case of the base alloy were mainly Al_m(Fe,Mn) and Al_3(Fe,Mn), while those observed in the alloys with high Mn contents (0.4, 0.7, and 1%) were largely Al_6(Fe,Mn) and α-Al(Fe,Mn)Si, as indicated by the SEM-EDS results (not showed here). The detailed analyses of Fe/Mn-bearing intermetallics in 5xxx alloys are reported in the literature [18,21,26]. After etching with 0.5 % HF, dispersoids could be clearly observed in the aluminum matrix (Fig. 4-2). In the base alloy (0.1Mn), almost no dispersoid was observed (Fig. 4-2a). In the other three alloys (0.4Mn, 0.7Mn, and 1Mn), a number of Mn-bearing dispersoids appeared, and they were uniformly distributed in the interiors of the aluminum cells/grains (Figs. 4-2b to d). The interdendritic regions were almost free of dispersoids and were denoted as DFZs (see arrows in Fig. 4-2b to d). The DFZ area fractions were quantified

by analyzing a series of optical images, and the results are shown in Fig. 4-2e. The 0.4Mn alloy exhibited the lowest DFZ area fraction (~8%). With an increase in the Mn content to 0.7%, the DFZ area fraction increased to 25%; however, with a further increase in the Mn content to 1%, it remained almost stable.

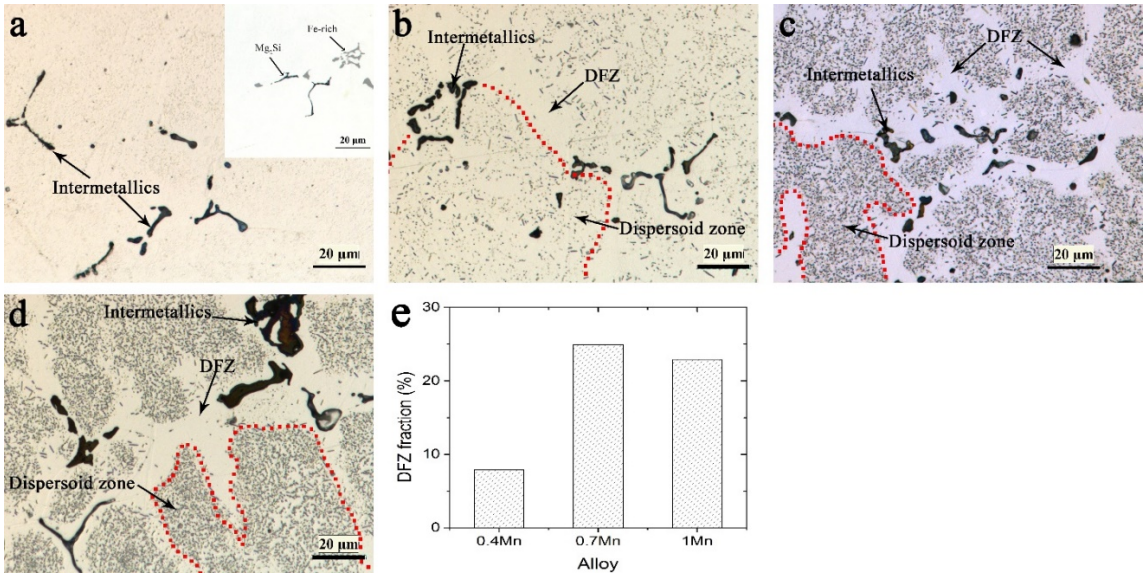

Fig. 4-2 Optical microstructures after homogenization, a) 0.1Mn, b) 0.4Mn, c) 0.7Mn and d) 1Mn alloys, e) the area fraction of the DFZ in three dispersoid-containing alloys.

The distribution of the dispersoids in the dispersoid zones was further analyzed using SEM and transmission electron microscopy (TEM). The 0.4Mn alloy was composed of two types of dispersoids: 1) long needle-like dispersoids (Figs. 4-3a and d) with a stoichiometry of Al_6(Fe,Mn) and 2) fine rhomboidal ones with a chemical composition of α-Al(Fe,Mn)Si (Fig. 4-3e) [27]. The spectra of TEM-EDS from the dispersoids are presented Fig. 4-4. In the 0.7Mn alloy also, there were two types of dispersoids (Fig. 4-3b): long needle-like dispersoids same (Al_6(Fe,Mn) stoichiometry) as those in the 0.4Mn alloy located at the vicinity of dispersoid zones and fine plate- and cube-like dispersoids in the dispersoid zones (Fig. 4-3f), which were identified to be Al_6Mn [28]. With an increase in the Mn content to 1.0% (1Mn), the long needle-like dispersoids disappeared, and only the fine plate- and cube-like dispersoids (Al_6Mn) remained in the dispersoid zones (Fig. 4-3c and g). The dispersoids were mainly identified by carrying out TEM-EDS analysis on several particles in each sample and comparing the results with those reported in the literature [27, 28]. The number density of the dispersoids was quantified using the SEM images of the alloys, and the average

equivalent diameter was measured from the TEM images, and the results are shown in Fig. 4-3h. With an increase in the Mn content, the dispersoids became finer and more densely distributed. For instance, the average equivalent diameter of the dispersoids decreased from 660 nm for 0.4Mn to 140 nm for the 1Mn alloy, while the number density of the dispersoids increased from 0.65 μm^{-2} for 0.4Mn to 2.05 μm^{-2} for the 1Mn alloy.

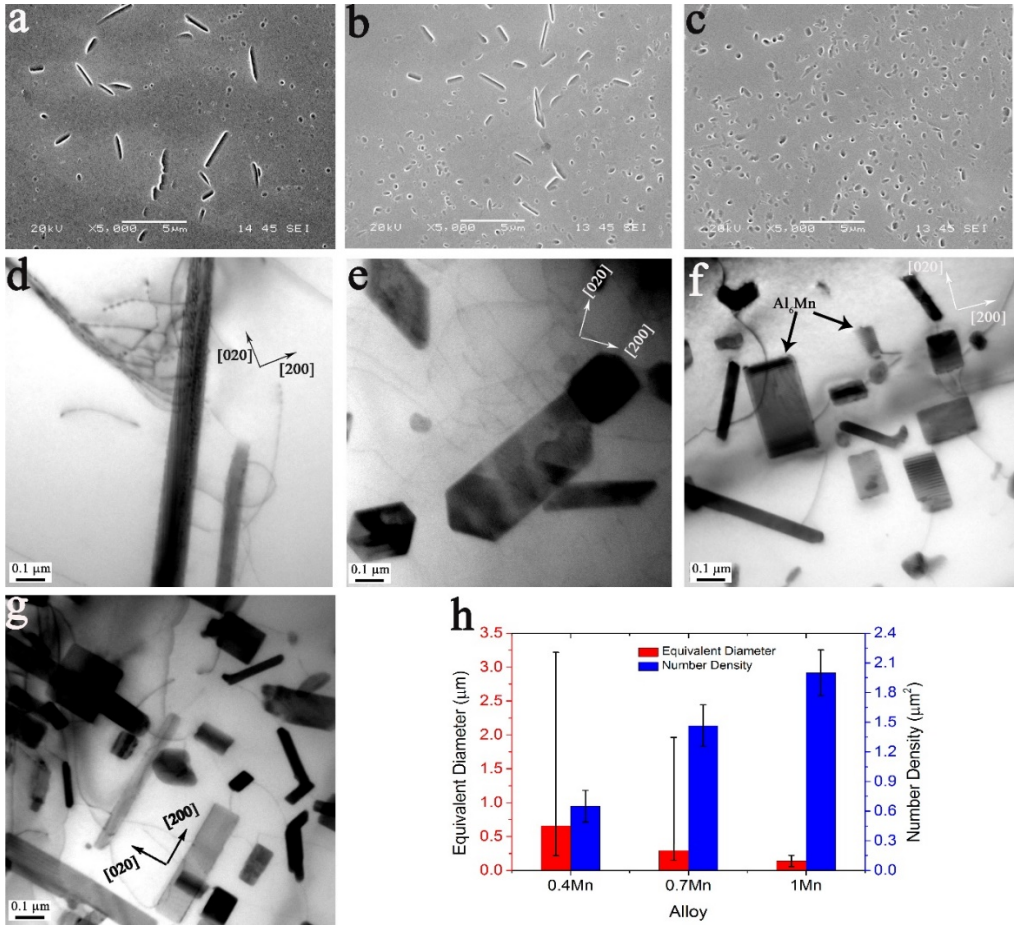

Fig. 4-3: SEM images of dispersoids in a) 0.4Mn, b) 0.7Mn and c) 1Mn alloys. Bright-field TEM images of dispersoids, d) the long needle-like ones in Fig. 3a and b, e) the fine α-Al(Fe,Mn)Si in Fig. 4-3a, f) the fine Al_6Mn in Fig. 4-3b, g) the fine Al_6Mn in Fig. 4-3b, and h) the average equivalent diameter and number density of dispersoids in three alloys.

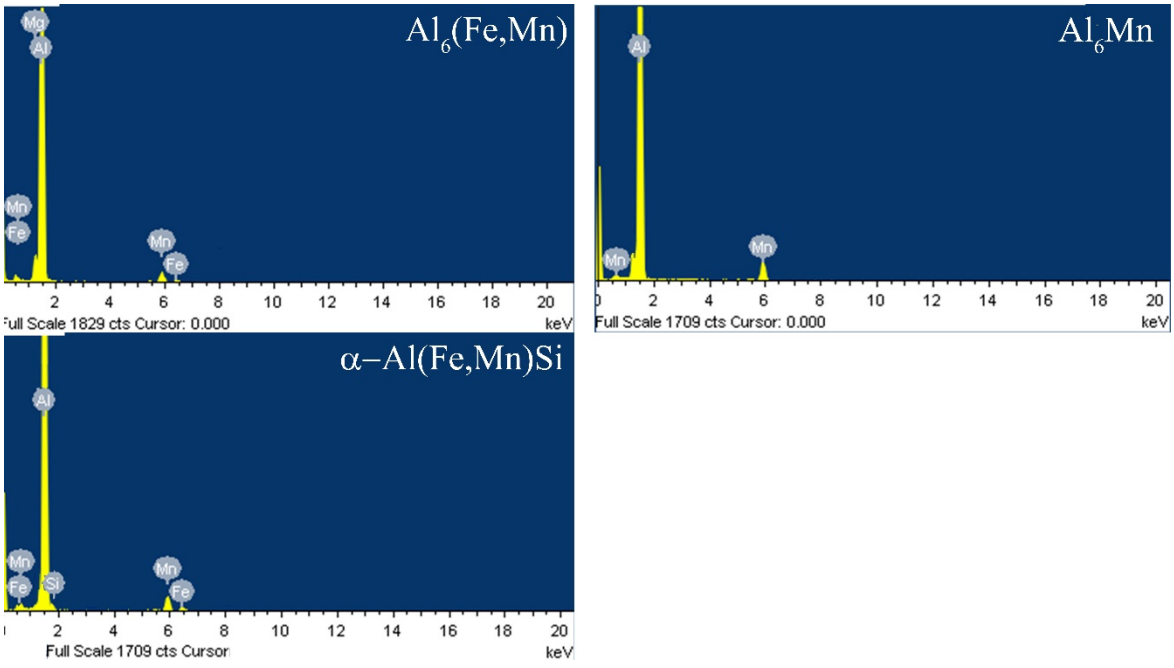

Fig. 4-4: The TEM-EDS spectra from the dispersoids

4.3.2 Flow stress behavior

The uniaxial hot compression tests of the Al-Mg-Mn alloys with different Mn contents were carried out at the deformation temperatures ranging from 350 to 500°C and the strain rates ranging from 0.001 to 1 s^{-1}. Fig. 4-5 shows the typical true stress-true strain curves of the four alloys. As can be observed from the curves, the flow stress increased sharply at the beginning of the deformation process to reach the peak stress. The sharp rise in the flow stress was due to the predominant work hardening at the initial stage of deformation, which was induced by dislocation multiplication and a large increase in the number density of dislocations.

The flow stress curves exhibited three distinct trends in the subsequent step: a) A slow but progressive increase in the flow stress with further straining, which is often observed under the high-Z deformation condition (e.g., 350°C/1s^{-1}. The progressive increase in the flow stress indicates that the softening mechanisms (DRX/DRV) were dominated by work hardening [7]. b) A steady-state condition with a fairly stable plateau of flow stress until the end of deformation. This phenomenon was observed under the medium-Z condition (e.g. 400°C/0.01s^{-1}). The plateau of the flow stress represents a dynamic equilibrium between work-hardening and dynamic restoration. c) A slight but continuous decrease in the flow

stress until the end of straining was observed under the low-Z condition (e.g., 500°C/0.001s^{-1}). The tendency toward a slight reduction in the flow stress can be associated with the predominant softening mechanisms (i.e., DRV/DRX) [29-31].

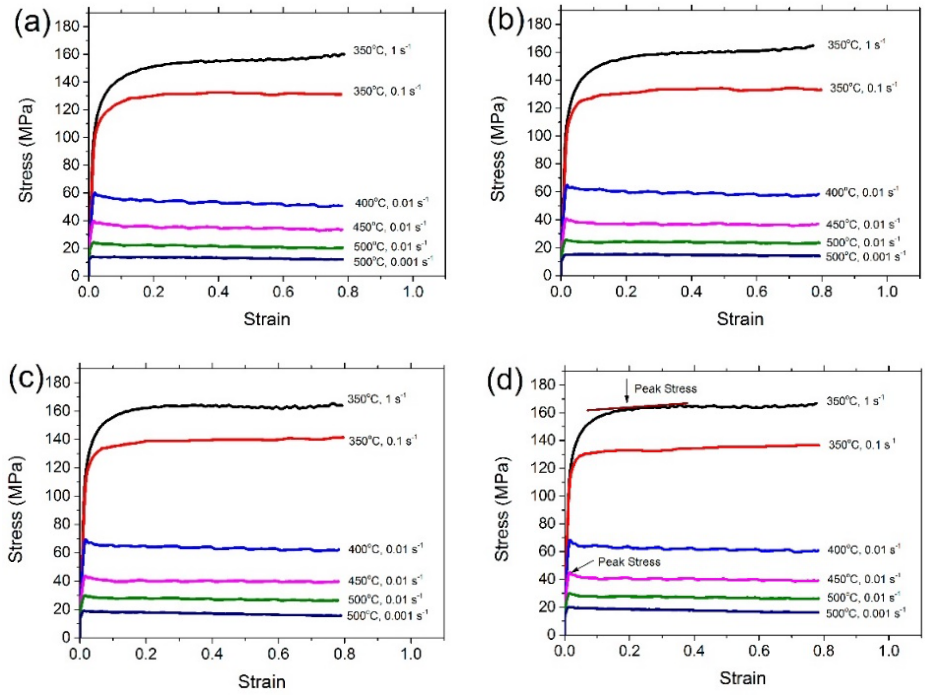

Fig. 4-5 The true stress-true strain curves of a) 0.1Mn, b) 0.4Mn, c) 0.7Mn, and d) 1Mn alloys.

As shown in Fig. 4-5, the hot deformation behavior of the alloys varied with the deformation conditions. For a given temperature, an increase in the strain rate enhanced the flow stress as it accelerated dislocation interaction and multiplication. A reverse tendency was observed when the temperature was increased at a constant strain rate, i.e., the flow stress decreased with an increase in the temperature.

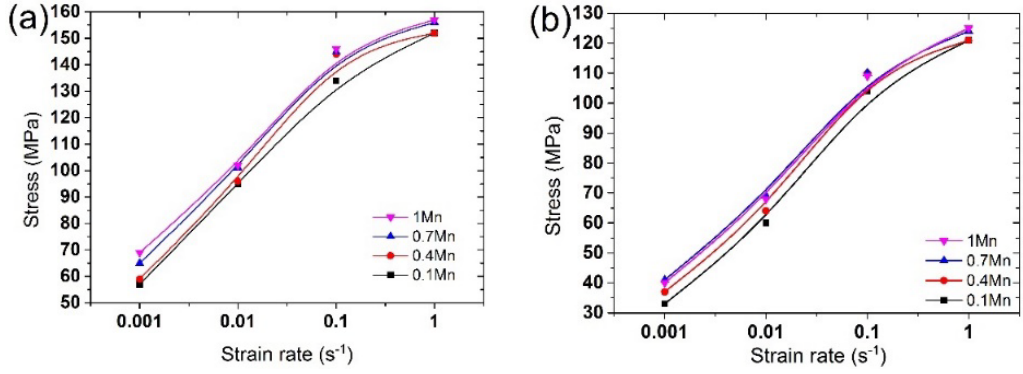

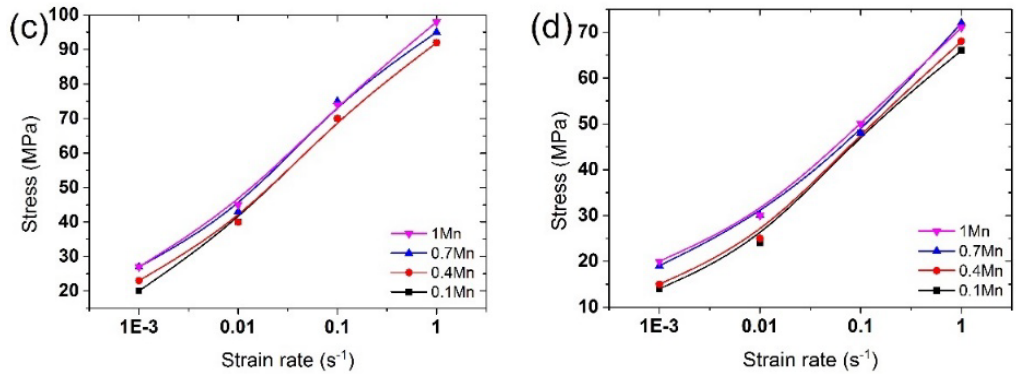

Fig. 4-6 The evolution of flow stresses with the Mn content in four alloys at a) 350 ℃, b) 400 ℃, c) 450 ℃ and d) 500 ℃.

To better elucidate the effect of the Mn content on the flow stress behavior of the alloys, their peak flow stress (σp) vs. strain rate curves were obtained, as shown in Fig. 4-6. With an increase in the Mn content, the peak flow stress of the alloys generally increased under all the four deformation temperatures (Fig. 4-6a to d). However, this influence was much more significant at lower strain rates. For instance, under the deformation at the strain rate of 0.001 s-1 and the temperature of 500 °C (Fig. 4-6d), the peak stress of the 0.1Mn alloy was 14 MPa, whereas those of the 0.4Mn, 0.7Mn, and 1Mn alloys were 15, 19, and 20 MPa, respectively. It can be seen that with an increase in the Mn content from 0.1 to 1%, the peak stress of the alloys increased by up to 43%. However, with an increase in the strain rate from 0.001 to 1 s^{-1}, the effect of the Mn content on the peak stress decreased. For instance, at the strain rate of 1 s^{-1}, the peak stresses for the 0.1Mn, 0.4Mn, 0.7Mn, and 1Mn alloys were 66, 68, 72, and 73 MPa, respectively. This indicates that the peak stress increased by approximately 10% with an increase in the Mn content from 0.1 to 1.0%.

4.3.3 Constitutive analyses

Constitutive equations are a very useful analytical tool for simulating the deformation behavior of materials and predicting the effect of the deformation parameters on their flow stress response during hot deformation. The hyperbolic sine equation, proposed by Sellars and McTegart [32], known as the Zener-Hollomon parameter (Z), is widely used to describe the relationship between the strain rate, deformation temperature, and flow stress and is effective over a wide range of deformation temperatures and flow stresses [22,23,33,34]. The equation is mathematically expressed as follows [32]:

$$Z = \dot{\varepsilon} \exp\left(\frac{Q}{RT}\right) = A[\sinh(\alpha\sigma)]^n \qquad \text{Eq. 4-1}$$

where Z is the Zener–Hollomon parameter, $\dot{\varepsilon}$ is the deformation strain rate (s^{-1}), Q is the activation energy for hot deformation (kJ/mol), R is the universal gas constant (8.314 J/mol K), T is the deformation temperature (K), A and n are material constants, α is the stress multiplier, and σ is the flow stress (MPa).

The experimental flow-stress data obtained for the 0.4Mn alloy were used as an example to determine the activation energy and material constants. The peak stress (σ_p), which generally represents the dynamic equilibrium between work hardening and flow softening, is considered as the flow stress (σ). The stress multiplier, α, was defined as $\alpha=\beta/n_1$, where β and n_1 for the experimental deformation temperatures used in this study were evaluated using the mean slopes of the lnε̇ – σ (Fig. 4-7a) and ln$\dot{\varepsilon}$ – lnσ (Fig. 4-7b) plots, respectively. The mean value of α was calculated to be 0.018 MPa^{-1}. The partial differentiation of Eq. 4-1 yields Eq. 4-2.

$$Q = R\left[\frac{\partial ln\dot{\varepsilon}}{\partial \ln[\sinh(\alpha\sigma)]}\right]_T \left[\frac{\partial \ln[\sinh(\alpha\sigma)]}{\partial \frac{1}{T}}\right]_{\dot{\varepsilon}} = RnS \qquad \text{Eq. 4-2}$$

where n is the mean slope of the plots of ln$\dot{\varepsilon}$ – ln[sinh(ασ)] at various temperatures (Fig. 4-7c) and S is the mean slope of the plots of ln[sinh(ασ)] – 1/T at different strain rates (Fig. 4-7d). The mean slope of the plot of lnε̇ versus ln[sinh(ασ)] gives the n value of 3.619. In the plot of ln[sinh(ασ)] versus 1/T, the average slope at all strain rates was calculated to acquire S=5.55.

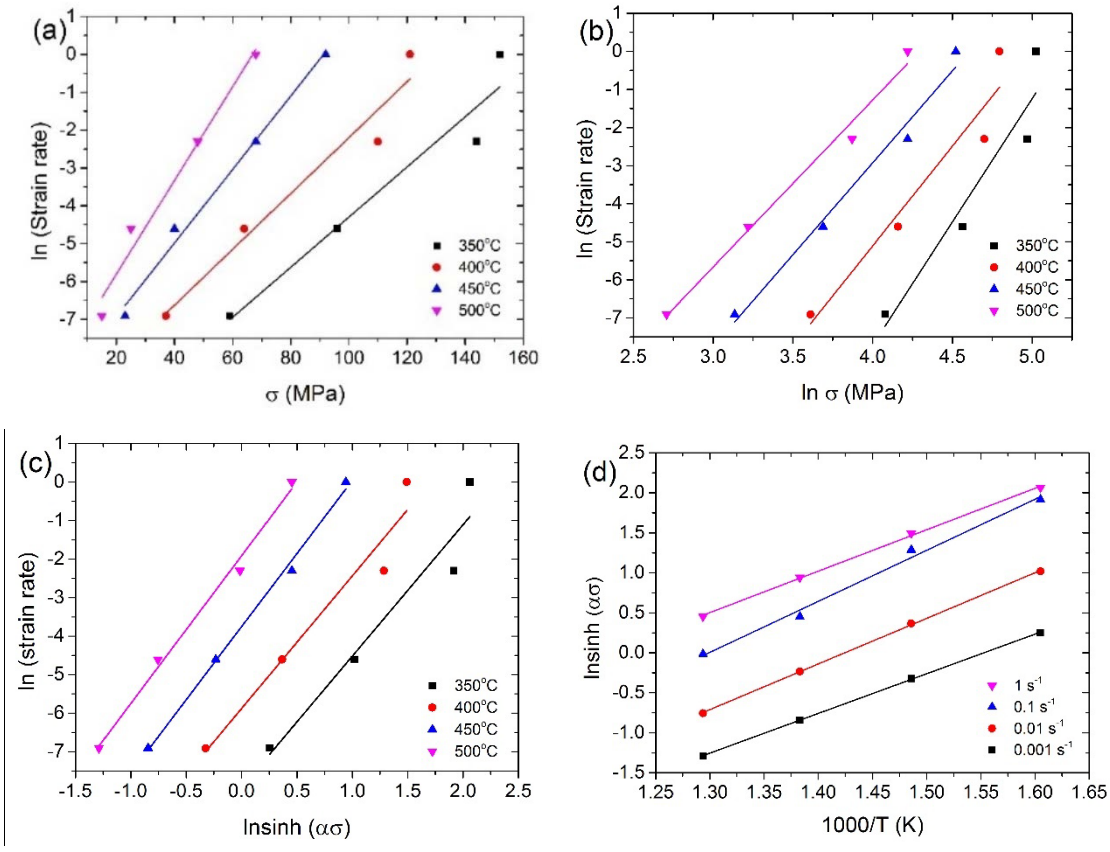

Fig. 4-7 Relationships between a) lnε̇ and σ, b) ln ε̇ and lnσ, c) lnε̇ and ln[sinh (ασ)] and d) ln[sinh(ασ)] and 1000/T.

Applying the natural logarithm of Eq. 4-1 yields Eq. 4-3, which was used to calculate the material constants n and A from the slope and intercept of the ln Z vs. ln sinh (ασ) linear plot, respectively.

$$lnZ = lnA + nln[sinh(\alpha\sigma)] \qquad \text{Eq. 4-3}$$

where lnA is derived from the intercept of the linear plot of lnZ – lnsinh(ασ). As Fig. 4-8 presents, linear fitting is in acceptable agreement ($R^2 = 0.99$) and the material constants n and A for the 0.4Mn alloy were found to be 3.6 and 2.65×10^{10}, respectively.

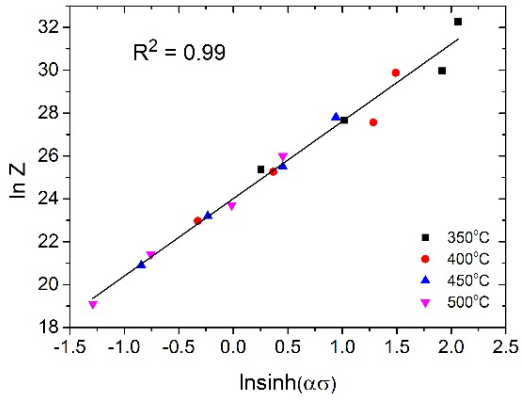

Fig. 4-8 Correlation between lnZ and ln[sinh(σ)].

Table 4-2. Values of material constants and activation energies of four alloys studied.

Alloys	α (MPa^{-1})	n	A (s^{-1})	Q (kJ/mol)
0.1Mn	0.019	3.4	7.13×10^{9}	159.7
0.4Mn	0.018	3.6	2.65×10^{10}	167.1
0.7Mn	0.016	4.0	7.03×10^{10}	172.7
1Mn	0.017	3.79	5.99×10^{10}	176.7

In a similar manner, the material constants α, n, and A and activation energies (Q) were calculated using Eq. 4-1 – Eq. 4-3 for all the studied alloys, and the results are summarized in Table 4-2. The activation energy for hot deformation (Q) is an important parameter that indicates the degree of difficulty in plastic deformation. The Q values calculated for the four alloys were consistent with those reported previously for Al-Mg-Mn alloys. For instance, Dai et al. [16] obtained a Q value of 168.6 kJ/mol for a typical AA5083 alloy containing 0.5% Mn, which is comparable to the Q value calculated for the 0.4Mn alloy in this study (167.1 kJ/mol). It is also evident that the Q value of Al-Mg-Mn alloys increases with an increase in the Mn content. The Q value increased gradually from 159.7 to 176.7 kJ/mol with an increase in the Mn content from 0.1 to 1.0 % because of the increased pinning effect of the dispersoids on the dislocations, which resulted in an increase in the deformation resistance of the alloys at all the deformation temperatures. This is discussed in detail in section 4.4.

Based on Eq. 4-1, the peak flow stress, σ, can be expressed as a function of Zener-Hollomon parameter, Z, as follows:

$$\sigma = \frac{1}{\alpha} sinh^{-1}[\frac{Z}{A}]^{\frac{1}{n}} = \frac{1}{\alpha} sinh^{-1}[\frac{\dot{\varepsilon} \exp\left(\frac{Q}{RT}\right)}{A}]^{\frac{1}{n}} \quad \text{Eq. 4-4}$$

Using the values of the established material constants and Q (Table 4-2), the peak flow stress of the Al-Mg-Mn alloys could be predicted at any given temperature and strain rate based on Eq. 4-4. The predicted and measured peak flow stress values for all the four alloys investigated in this study are plotted in Fig. 4-9. To assess the accuracy of the developed constitutive equation and to evaluate the strength of the linear relationship between the predicted and experimental values, the correlation coefficient (R^2) and average absolute relative error were calculated as follows [100].

$$AARE\ (\%) = \frac{1}{n}\sum_{i=1}^{n}\left|\frac{\sigma_{E_i} - \sigma_{P_i}}{\sigma_{E_i}}\right| \quad \text{Eq. 4-5}$$

where σ_{E_i} and σ_{P_i} are the experimental and predicted values of each point, and n is the total number of the employed data samples. The correlation coefficient, R^2, are greater than 0.97 and the average error, AARE, are less than 6% for all alloys studied, which show a good agreement between the experimental and predicted results.

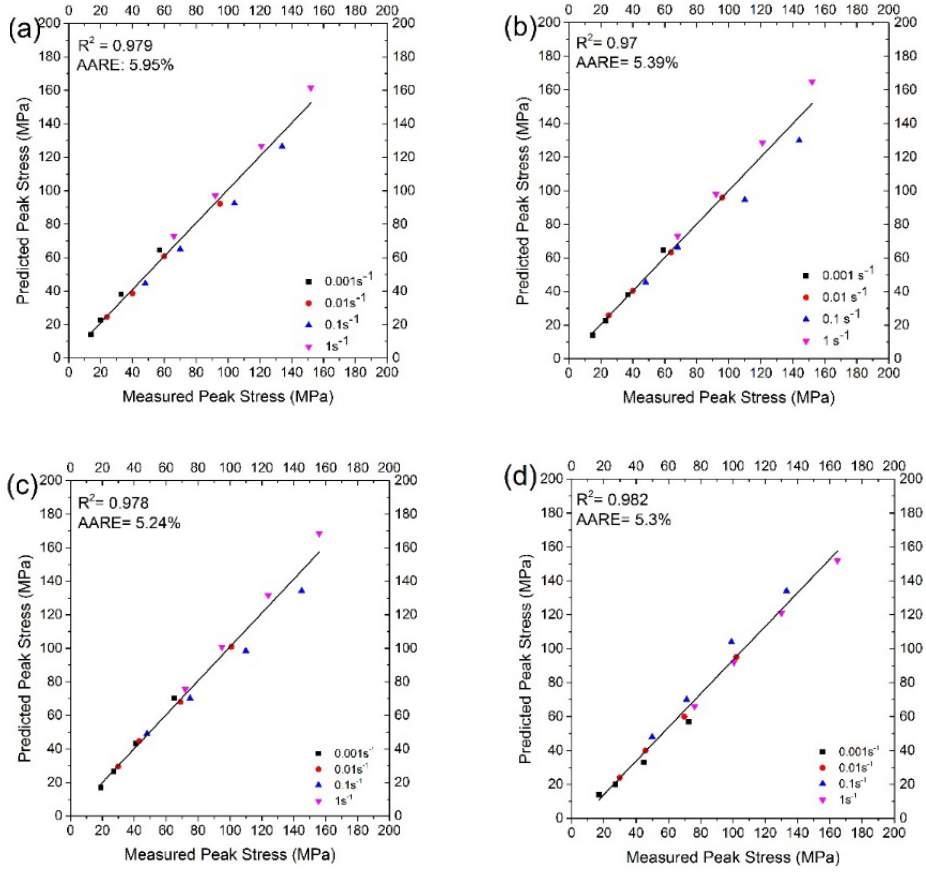

Fig. 4-9 Correlation between predicted and measured peak flow stress, a) 0.1Mn, b) 0.4Mn, c) 0.7Mn and d) 1Mn alloys.

4.3.4 Microstructure evolution during hot deformation

To investigate the effect of Mn on the microstructure evolution of the alloys during deformation, the samples deformed under three typical deformation conditions 1) high-Z (350°C/0.1s^{-1}), 2) medium-Z (400°C/0.01s^{-1}), and 3) low-Z (500°C/0.001s^{-1}) were selected. The microstructures of the samples deformed under these conditions were examined at the true stain of 0.8 using the EBSD technique.

4.3.4.1 Microstructure under the high-Z condition

Fig. 4-10 shows the optical microscopy images and Euler orientation maps of the 0.1Mn, 0.4Mn, and 1Mn alloys under the high-Z deformation condition. The deformed

microstructures of all the four alloys (0.1Mn, 0.4Mn, 0.7Mn, and 1Mn) were similar and consisted of pancaked grain structures elongated perpendicular to the compression direction. The original grains were severely deformed, which resulted in a significant increase in the volume of the sub-boundaries and interfaces. Deformation bands were observed in the grain interiors (black arrows in Fig. 4-10.a – c) along with the shear bands at the grain boundaries (white arrows in Fig. 4-10d – f). The deformation bands were formed because of the lack of active slip systems inside the grains at low deformation temperatures, which resulted in regional rotation within the grains to compensate for the strain imposed by the neighboring grains [36]. Shear bands were formed owing to the localized plastic deformation, which increased the local temperature adiabatically to release the stored energy by creating a large number of tiny recrystallizations along the original grain boundaries [37]. Similar behaviors have been reported previously for Al-Mg alloys deformed at high strain rates and temperatures below 425°C [15]. It was observed that with an increase in the Mn content, the shear bands increased (Fig. 4-10d vs. Fig. 4-10f). This is because Mn increased the amount of Fe/Mn-bearing intermetallics, which caused incompatibility between the aluminum matrix and intermetallic particles in terms of the induced strain.

Despite the formation of the deformation bands and shear bands, the presence of intense substructures and sub-boundaries in the elongated grains implies that DRV was the main softening mechanism of the alloys. However, the presence of heavily deformed regions and the instability of the shear bands indicate that the restoration mechanism was weak. This is consistent with the flow stress curves deformed at 350°C/0.1s^{-1}, which showed a slight but gradual increase in the flow stress with increasing strain after reaching the peak flow stress, implying the work hardening is still dominated.

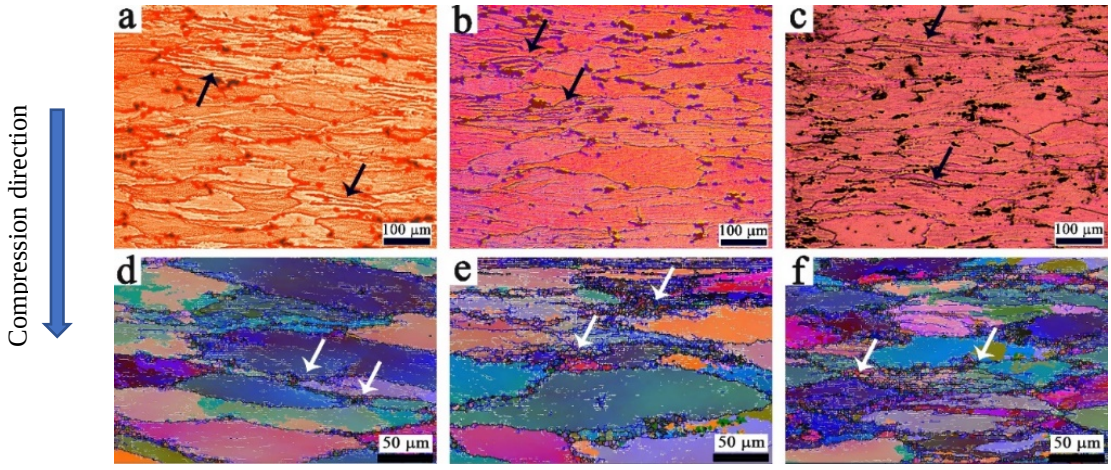

Fig. 4-10: The optic images (a - c) and All Euler maps (d - f) of as-deformed samples: a) and d) 0.1Mn, b) and e) 0.4Mn, and c) and f) 1Mn under 350℃/0.1s^{-1} deformation condition.

4.3.4.2 Microstructure under the medium-Z condition

The All-Euler orientation maps and quality grain boundary maps of the four alloys deformed under the medium-Z condition are shown in Fig. 4-11. Boundary distributions with the misorientation angles of 2–5° (LABs), 5–15° (MABs), and >15° (HABs) were also quantified as a function of the Mn content (Fig. 4-12). As shown in Fig. 4-11, the shear bands observed in the high-Z condition disappeared; however, the majority of grains was still elongated perpendicular to the compression direction. High densities of dislocation cells and subgrains were observed in all the grain interiors. These microstructures are characteristics of DRV. The level of DRV varied with the Mn content, as demonstrated by the misorientation angle distributions shown in Fig. 4-12. As compared to the base alloy (0.1Mn), the high-Mn content alloys (0.4Mn, 0.7Mn, and 1Mn) showed high LAB (2–5°) and low HAB (>15°) fractions, indicating that the Mn content significantly affected the restriction of DRV owing to the presence of dispersoids. For instance, the LAB fraction increased from 35% for the base alloy to 50% for the 0.4Mn alloy and further to 55% for the 0.7Mn and 1Mn alloys (Fig. 4-12a).

However, partial DRX could be clearly observed along the grain boundaries in all the four alloys. During the hot deformation, the applied stress increased the dislocation density gradient near the grain boundaries, leading to the generation of serrated grain boundaries. Along the serrated grain boundaries, new DRXed grains were formed because of the bulging

of the boundaries (see the arrows in Fig. 4-11a – 10d). In addition, because of the localized strain concentration the triple points acted as favorable nucleation sites for DRX. Some narrow-recrystallized regions, including newly formed equiaxed grains surrounded by HABs (black lines) and MABs (blue lines), were observed adjacent to the original grains. The formation of relatively HABs via progressive lattice misorientation and subgrain rotation can be considered as CDRX. An increase in the Mn content inhibited the DRV. As CDRX is a DRV-driven mechanism, CDRX was also inhibited in the three alloys with high Mn contents. As shown in Fig. 4-12a, with an increase in the Mn content from 0.1 to 0.4%, the HAB fraction decreased from 50 to 30%. The HAB fraction remained the same with a further increase in the Mn content to 0.7 and 1%. This can be attributed to the decrease in the overall DRX of the alloys with an increase in the Mn content.

It is worth noting that under the medium-Z deformation condition, the flow curves remained constant after reaching the peak flow stress until the end of the deformation (Fig. 4-5). This implies that a dynamic equilibrium was established between work hardening and the two restoration mechanisms (DRV and DRX).

4.3.4.3 Microstructure under the low-Z condition

The All-Euler orientation and quality grain boundary maps of the four alloys deformed under the low-Z condition are shown in Fig. 4-13. Under this deformation condition (high temperature and low strain rate), the microstructures exhibited better restoration with an overall low LAB density and high HAB density as compared to those observed under the medium-Z deformation condition. This is because high temperatures increase the grain boundary mobility, whereas low strain rates allow sufficient time for dislocation slipping, thus promoting both DRV and DRX. The base alloy (0.1Mn) consisted mainly of equiaxed grains (Fig. 4-13a), which were mostly HABs with a negligible fraction of internal substructures (LABs and MABs). This indicates that full DRX occurred in the base alloy. In contrast, the alloys with high Mn contents (0.4Mn, 0.7Mn, and 1Mn) still had the majority of elongated and deformed grains. The 0.4Mn alloy consisted of a relatively large number of LABs, but partial recrystallization occurred (Fig. 4-13b). The newly crystallized grains were mainly restricted to the original grain boundaries. Similar tendency was also observed in the microstructure of the other two high-Mn content alloys (0.7Mn and 1Mn). These new recrystallized grains with HABs or some with MABs (marked by arrows in Fig. 4-13b–d),

formed by progressive lattice misorientation and subgrain rotation, are characteristic of CDRX.

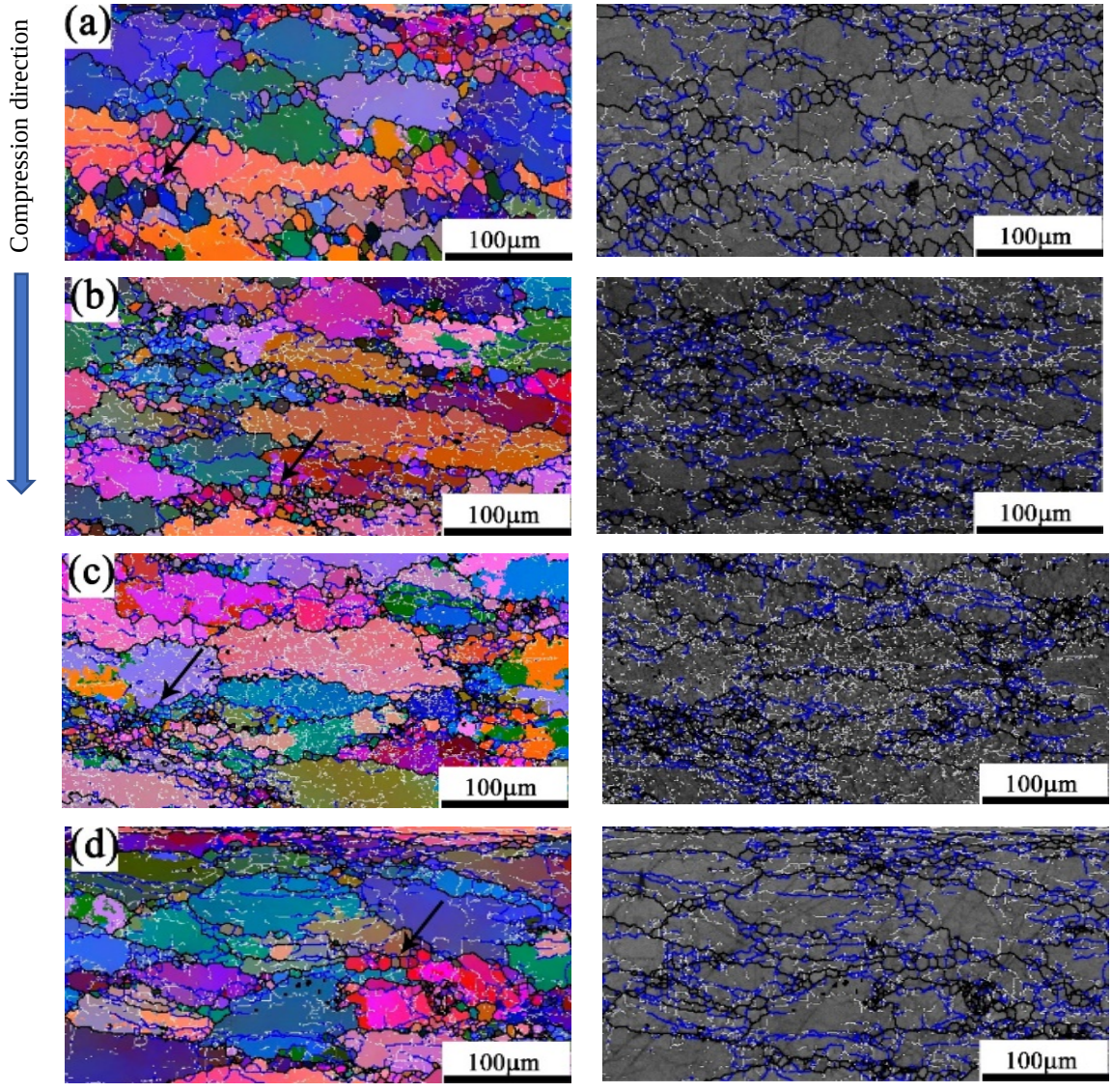

Fig. 4-11 All Euler orientation maps and quality grain boundary maps of samples under the 400℃/0.01s^{-1} deformation condition: a) 0.1Mn, b) 0.4Mn, c) 0.7Mn, and d) 1Mn alloys. White lines remark 2-5°, green lines 5-15° and black lines >15° misorientations.

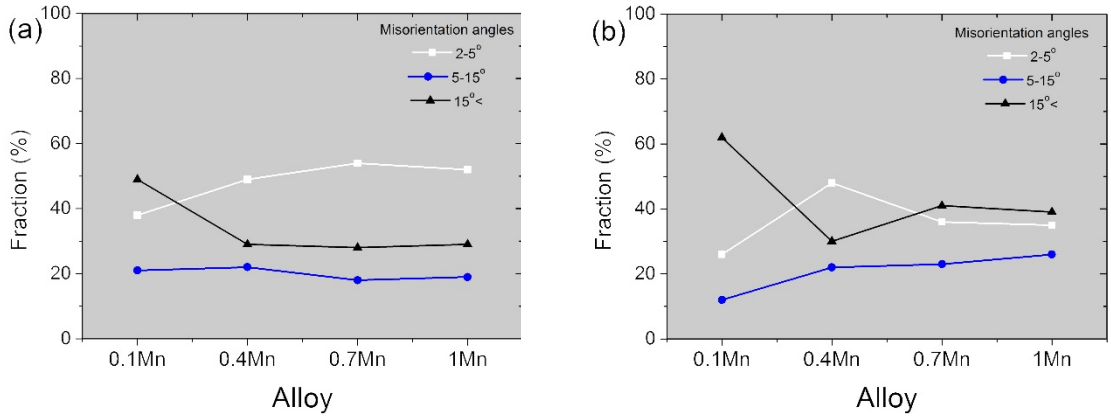

Fig. 4-12 The effect of Mn on the evolution of the misorientation angle distribution, a) at the medium-Z (400℃/0.01s^{-1}) and b) at the low-Z (500℃/0.001s-1).

The misorientation angle distributions at the boundaries of the four alloys are shown in Fig. 4-12b. The base alloy (0.1Mn) had the highest fraction of HABs (~65%) and the grain structure was fully recrystallized, indicating that dislocation rearrangement and recrystallization were much easier in this alloy as compared to the other alloys owing to the absence of dispersoids. With an increase in the Mn content to 0.4, 0.7, and 1%, the LAB fractions of the alloys increased from 25% (base alloy) to 50, 38, and 39%, respectively. Meanwhile, the HAB fraction decreased from 65% (base alloy) to 30% in the 0.4Mn alloy, but it slightly increased to ~40% for the 0.7Mn and 1Mn alloys. These results indicate that the increase in the Mn content from 0.1 to 0.4%, which introduced a number of Mn-bearing dispersoids in the grain interiors (Fig. 4-3), had a significant effect on the retardation of DRX. However, a further increase in the Mn content from 0.4% to 0.7 and 1% seemed to be less effective in inhibiting the DRX by Mn-bearing dispersoids. The reason for this is discussed in section 4.4.

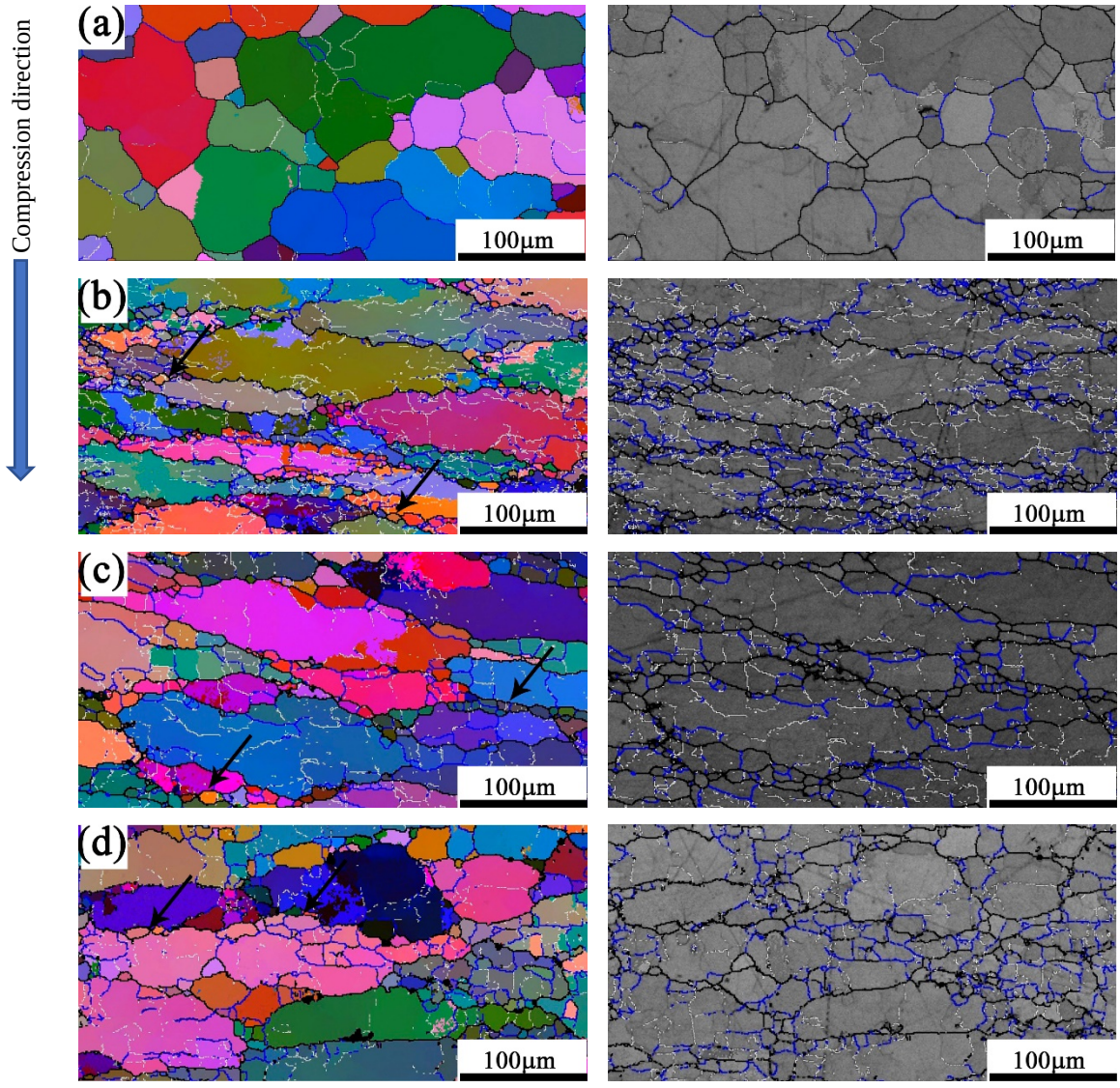

Fig. 4-13 All Euler orientation and quality grain boundary maps of samples deformed under the 500℃/0.001s^{-1} deformation condition: a) 0.1Mn, b) 0.4Mn, c) 0.7Mn and d) 1Mn alloys. White lines remark 2-5°, green lines 5-15° and black lines >15° misorientations.

4.4 Discussion

4.4.1 Effect of Mn on the activation energy of hot deformation

Various studies have been carried out on the hot deformation behavior and activation energy of Al-Mg-Mn alloys, mostly focusing on Al-5Mg-0.4Mn (AA5182) and Al-5Mg-0.7Mn (AA5083) alloys. Table 3 lists the previously reported Q values for these alloys under

different process conditions. Except the first Q value reported in [13], which seems obviously to be too low for the Al-5Mg alloy, the Q values for AA5182 alloys vary from 175 to 218 kJ/mol (25%). Similar results have been reported for AA5083 alloys, whose Q values vary from 153 to 205 kJ/mol (34%). The large variation in the Q values of 5xxx alloys with similar chemical compositions can mainly be attributed either to the metallurgical factors (e.g., intermetallics, dispersoids, and their distributions) or the state of the starting materials before the deformation (as-rolled, as-extruded, and as-homogenized). It is apparent that the state of the starting materials significantly affects the Q value of these alloys, probably because these alloys exhibit a wide variety of microstructures under different process conditions. For most thermomechanical processes (rolling, extrusion, and forging), the cast ingots/billets generated after the homogenization process are the common starting materials. When considering only four as-homogenized conditions (Table 4-3) [16,38,43], which are close to our experimental conditions, the Q value varies in the narrow range from 168 to 185 kJ/mol, which is in good agreement with the Q values calculated in this study.

Table 4-3. Summary of the values of the activation energy in Al-Mg-Mn 5xxx alloys

Alloy	Q (kJ/mol)	%Mg	%Mn	%Cu	State prior deformation	References
5182	167	4.65	0.4	-	Homogenized	Prensent study
5182	125	3.6	0.16	-	Homogenized	Haaften et al. [13]
5182	175	4.43	0.33	-	Homogenized	Verlinden et al. [38]
5182	182	4.33	0.3	1	Homogenized	Verlinden et al. [38]
5182	185	4.5	0.35	-	As-rolled	McQueen et al. [39]
5182	196	4.66	0.31	0.05	As-rolled	Wells et al. [40]
5182	218	4.5	0.35	-	As-rolled	McQueen et al. [41]
5083	173	4.74	0.74	-	Homogenized	Prensent study
5083	153	4.7	0.7	-	As-rolled	Hsiao et al. [42]
5083	163	4.45	0.74	-	As-rolled	McQueen et al. [11]
5083	168	4.8	0.5		Homogenized	Dai et al. [16]
5083	185	4.63	0.64	-	Homogenized	Fang et al. [43]
5083	205	4.5	0.8	0.05	As-extruded	Ding et al. [17]

The solid solubility of Mg in Al is approximately 15% at 451 °C [44]. Hence, the ~4.7% Mg present in all the alloys was expected to remain in the solid solution after homogenization. As compared to the Q value of pure aluminum (142 kJ/mol) [23], the base alloy showed high Q value (159.7 kJ/mol) mainly because of the Mg solid solution hardening effect. With an increase in the Mn content from 0.1 to 1%, the Q value increased moderately from 159.7 to 176.7 kJ/mol (Table 4-2) owing to the formation of Mn-rich dispersoids and their influence on the softening mechanism. As mentioned earlier, with an increase in the Mn content from 0.1 to 0.4%, Mn-rich dispersoids appeared after homogenization. With a further increase in the Mn content, the number density of these dispersoids increased; however, the fraction of the DFZs also increased (Fig. 4-2). The effect of the Mn content on the hot deformation behavior and Q of the alloys depended on two competing factors. The presence of dispersoids had a strong pinning effect on dislocation slip and subgrain rotation [22,33,34]. In the case of the base alloy (0.1Mn), in which dispersoids were absent, DRX could easily propagate under the medium-/low-Z deformation conditions (Fig. 4-11 and Fig. 4-13). After the formation of dispersoids in the alloys with high Mn contents (0.4Mn, 0.7Mn, and 1Mn), the recovered grain structure was retained and DRX was restrained. The higher the Mn content was, the higher was the number density of the dispersoids and the stronger was the inhibiting effect on DRV and DRX. Therefore, the flow stress and Q values of the alloys increased with an increase in the Mn content. In contrast, DFZs facilitated DRX. In fact, the DFZs in the grain boundary regions persisted during the hot deformation and were elongated only in the deformation direction (Fig. 4-14a). In the high Mn-content alloys, DRX was limited in the DFZs, where nearly no dispersoids existed, and the pinning effect on the dislocations and subgrain boundaries was much weaker than that on the grain interiors. Fig. 4-14b shows the EBSD and optical images taken at the same location, where the DRXed grain bands fitted well with the shape and distributions of the DFZs. The increase in the DFZ fraction with increasing Mn content partially compensated for the overall inhibiting effect of the dispersoids on DRX. These two contradictory factors can explain the low increase in the Q value of the Al-Mg-Mn alloys investigated in this study with a considerable increase in the Mn content from 0.1 to 1%.

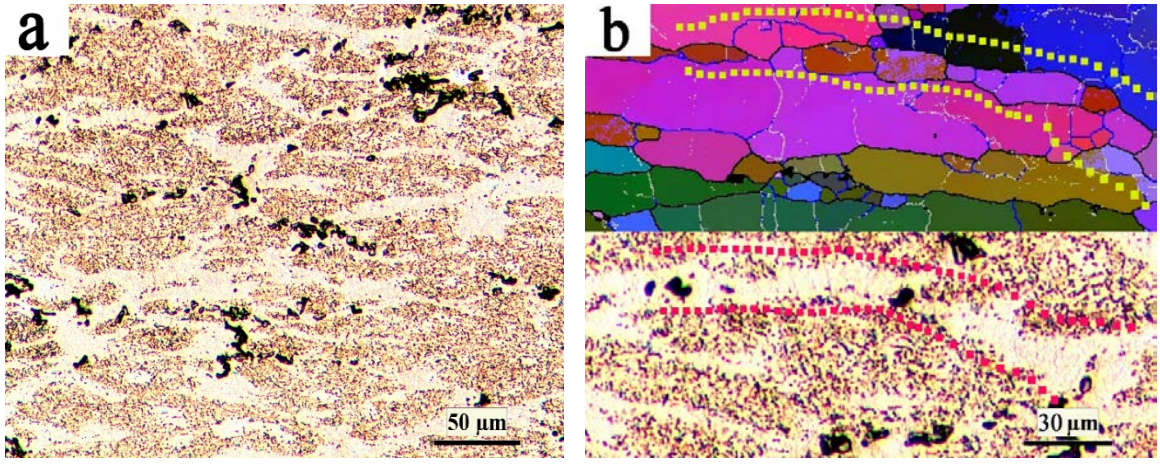

Fig. 4-14 Optical microscopy image showing that the DFZs (white zones) in the grain boundaries persisted during hot deformation and (b) EBSD and optical images taken at the same location showing DRX occurred mainly in DFZs, in an example of 0.7Mn alloy.

4.4.2 Characterizing the dominant softening mechanism

DRV and DRX are the typical softening mechanisms in aluminum alloys during hot deformation, competing with work hardening with increasing strain. As discussed earlier, DRX occurred more easily in the base alloy than in the high-Mn content alloys owing to the absence of dispersoids. CDRX was the main softening mechanism of the base alloy under the medium- and low-Z conditions, as confirmed by the TEM and EBSD observations. The TEM image in Fig. 4-15a shows the rearrangement of dislocations near the grain boundary in the base alloy deformed under the low-Z condition, indicating that the dislocations were continually absorbed to increase the misorientation to reach high angles, where the boundary started migrating at the expense of dislocations. Therefore, new grains could be progressively generated within the deformed grains because of the continuous configuration of a neat array of dislocations and an increase in the subgrain misorientation. Fig. 4-15b and c show the Euler maps of the fully recrystallized structure. Two neighboring grains (Zones I and II) were chosen and their misorientation profiles were compared. As shown in Fig. 4-15d, along with V_1, Zone I had a misorientation of approximately 14° relative to Zone II. Furthermore, the misorientations of the interfaces at V_2 and V_3 were 13.1° and 16.6°, respectively. These results indicate that the two grains were rotated relative to each other and were separated by a single boundary composed of partially MAB (blue line) and partially HAB (black line). With further deformation, these grains further rotated and their

misorientation angle increased, eventually evolving into newly recrystallized grains [10,33, 34]. These microstructural features were also observed in various grains. The subgrain rotations and progressive transition of LAB/MAG to HAG confirm that CDRX was the dominant softening mechanism in the base alloy.

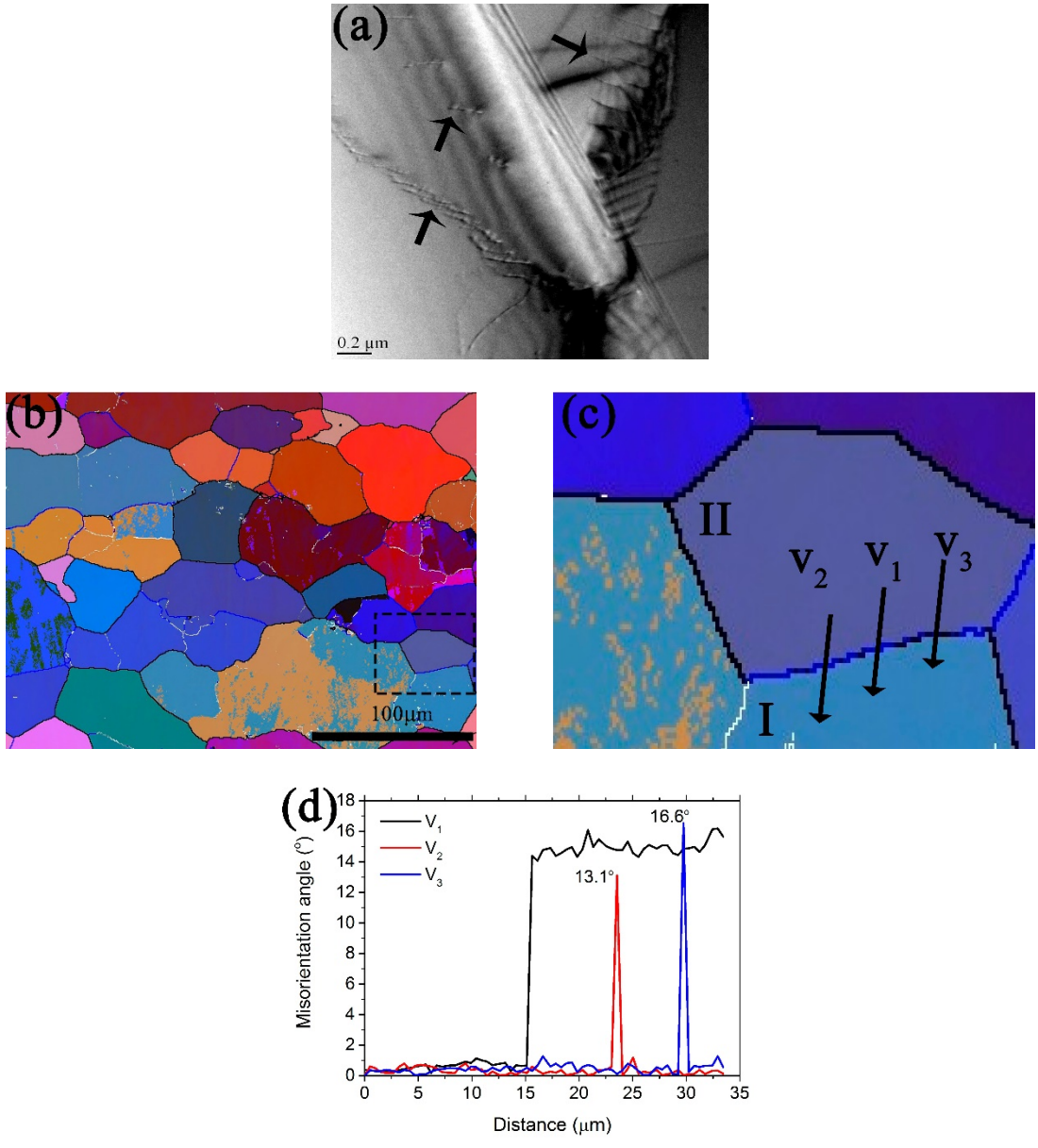

Fig. 4-15 (a) TEM image showing the rearrangement of dislocations near the grain boundary; (b) All Euler orientation map of the base alloy (0.1Mn) deformed under low-Z condition; (c) an enlarged image of the rectangle in Fig. 4-15b, and (d) the misorientation profile of the vectors in Fig. 4-15c.

In the three high-Mn content alloys (i.e., 0.4Mn, 0.7Mn, and 1Mn), DRX was suppressed in the grain interiors owing to the presence of a large number of dispersoids, and hence a strong pinning effect was observed on grain boundary migration and subgrain rotation. Therefore, DRV was the main softening mechanism in the grain interiors of these alloys, whereas DRX was dominant in the vicinity of the grain boundaries (i.e., DFZs). Fig. 4-16a and b show Euler maps of the partially recrystallized structure in the 0.7Mn alloy deformed under the low-Z condition. The grain interiors (along the black line V_7), which were divided into various regions by the subgrains, were mainly composed of LABs. The cumulative misorientation in the grain interior (along V_7) was 3–7° (Fig. 4-16c). These features confirm that DRV was the only active softening mechanism in the grain interiors. As shown in Fig. 4-16b, several small equiaxed grains were observed adjacent to the original grain boundaries. Two adjacent grains (grains 1 and 2) were chosen to examine the orientation profile. The misorientation angles along V_4 and V_5 in grain 1 were 7.8 ° and 15.4°, respectively. The misorientation angle along V_6 in grain 2 was 7.8°. These results indicate that the two identified grains were generated via the rotation of the subgrains and the progressive transition of the LABs/MABs to HABs. Part of Grain 1 had already evolved into HABs (V_5), but the second part was still an MAB (V_4) and transformed into an HAB with further straining. As indicated by the green arrows, the interiors of these newly formed grains were already subjected to subgrain rotation. Thus, these results indicate that CDRX was an active DRX mechanism in the DFZs of the alloys with high Mn contents.

Other DRX mechanisms were also observed in the DFZs of the high-Mn content alloys. In the homogenized and deformed microstructures (Fig. 4-2 and Fig. 4-14), intermetallic particles were always observed near the grain boundaries. As the intermetallic particles are hardly deformed, large strain could accumulate in the neighboring areas, resulting in easy nucleation and growth of new grains around the particles. The Euler map of the 0.7Mn sample deformed under the medium-Z condition is shown in Fig. 4-17. As shown in the enlarged image with a fine acquisition step of 0.1 μm (Fig. 4-17b), several intermetallic particles were observed (non-indexed, indicated in black) in the grain boundary. The intermetallic particles were surrounded by fine equiaxed recrystallized grains. This confirms the occurrence of particle-stimulated DRX in the alloy [10]. In addition, DDRX was observed, although it was less dominant than CDRX. As shown in Fig. 4-17a and c, new

grains nucleated at the local bulge on the original wavy grain boundary. Because the DRV rate was low under the medium-/low-Z conditions, the dislocation density gradient increased in the vicinity of the grain boundaries. Owing to the uneven straining of the neighboring grains, the dislocation density further increased at one side of the boundary, through which the bulged grain boundaries were generated (Fig. 4-17c). After reaching the critical radius, the bulged grains could locally rotate, through which sub-boundaries were formed in the grain interiors. Bulged grains surrounded by HABs on one side and sub-boundaries on the other side are observed in the initial steps of the DDRX phenomenon [9].

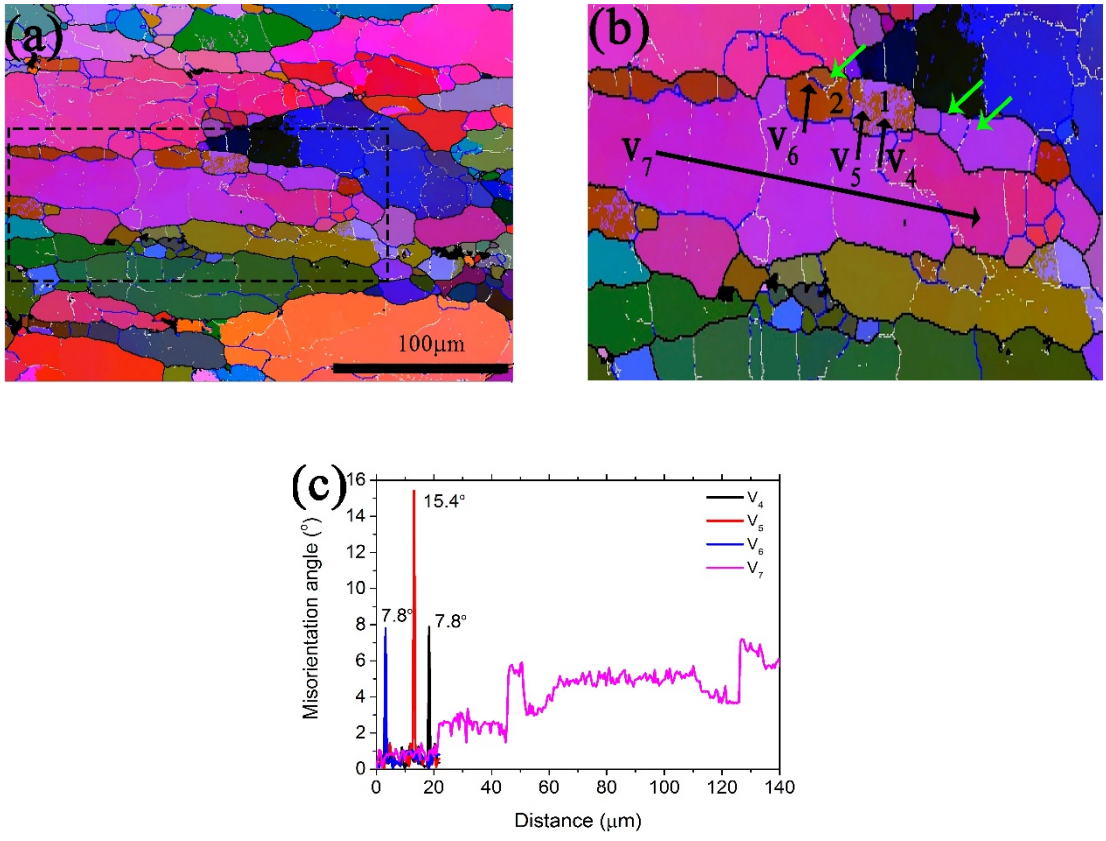

Fig. 4-16 (a) All Euler orientation map of the 0.7Mn alloy deformed under low-Z condition; (b) an enlarged image of the rectangle in Fig. 4-16a, and (c) the misorientation profile of the vectors in Fig. 4-16b.

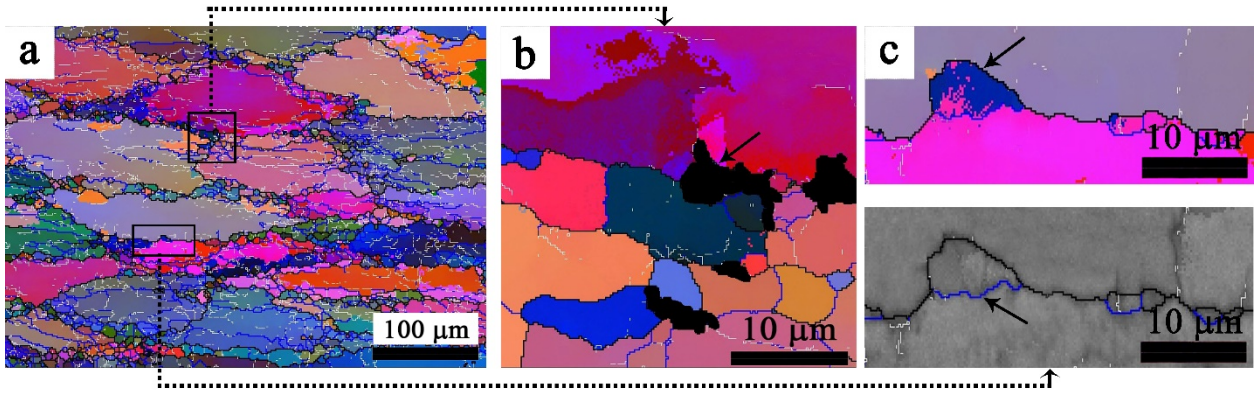

Fig. 4-17 (a) All Euler orientation map of the 0.7Mn alloy deformed under medium-Z condition, (b) an enlarged image indicating particle-stimulated DRX, and (c) an enlarged image and its quality map indicating discontinuous DRX by local boundary bulging.

4.5 Conclusions

1. After homogenization, almost no Mn-rich dispersoids were observed in the microstructure of the base alloy containing 0.1% Mn. With an increase in the Mn content to 0.4%, a number of Mn-rich dispersoids precipitated and were distributed in the interior of aluminum cells/grains. With an increase in the Mn content from 0.4 to 1%, the number density of dispersoids increased along with a remarkable increase in the DFZ fraction.
2. The peak flow stress increased gradually with an increase in the Mn content under a given deformation condition, owing to the strong strengthening effect of the dispersoids. At a low strain rate (0.001 s^{-1}), the peak flow stress increased by up to 43% with an increase in the Mn from 0.1 to 1%, whereas at a high strain rate (1 s^{-1}), the peak flow stress increased moderately to 10%.
3. The hyperbolic-sine constitutive equation was successfully employed to determine the material constants and activation energy for hot deformation in all the alloys. With an increase in the Mn content from 0.1 to 1%, the activation energy for hot deformation increased from 160 to 177 kJ/mol, which is consistent with the values reported in the literature for as-homogenized Al-Mg-Mn 5xxx alloys.

4. Under the high-Z deformation conditions, dynamic recovery was the main softening mechanism in all the alloys. Under the medium-/low-Z conditions, an increase in the Mn content promoted the retardation of DRV and DRX. The EBSD analysis confirmed that CDRX was the main recrystallization mechanism in the base alloy. In the alloys with high Mn contents, DRV was the dominant softening mechanism in the grain interiors, while DRX occurred in the DFZs, in which CDRX, particle-stimulated DRX, and DDRX coexisted.

4.6 References

[1] J. Hirsch, *Aluminium in Innovative Light-Weight Car Design*, Mater. Trans. 52 (2011), pp. 818–824.

[2] K. Zheng, D.J. Politis, L. Wang and J. Lin, *A review on forming techniques for manufacturing lightweight complex—shaped aluminium panel components,* Int. J. Light. Mater. Manuf. 1 (2018), pp. 55–80.

[3] J. Hirsch, *Recent development in aluminium for automotive applications*, Trans. Nonferrous Met. Soc. China (English Ed.) 24 (2014), pp. 1995–2002.

[4] W.S. Miller, L. Zhuang, J. Bottema, A.J. Wittebrood, P. De Smet, A. Haszler et al., *Recent development in aluminium alloys for the automotive industry*, Mater. Sci. Eng. A 280 (2000), pp. 37–49.

[5] D.G. Eskin, *Solidification of Aluminum Alloys*, in *Physical Metallurgy of Direct Chill Casting of Aluminum Alloys*, CRC Press, New York, 2008, pp. 19–78.

[6] J. Hirsch, *Aluminium sheet fabrication and processing*, in *Fundamentals of Aluminium Metallurgy: Production, Processing and Applications*, Woodhead Publishing Limited, 2010, pp. 719–746.

[7] F.J. Humphreys, G.S. Rohrer and A. Rollette, *Hot Deformation and Dynamic Restoration*, in *Recrystallization and Related Annealing Phenomena*, Elsevier Ltd, 2017, pp. 415–450.

[8] A. Heidarzadeh, S. Mironov, R. Kaibyshev, G. Çam, A. Simar, A. Gerlich et al., *Friction stir welding/processing of metals and alloys: A comprehensive review on microstructural evolution*, Prog. Mater. Sci. 117 (2020), pp. 100752.

[9] T. Sakai, A. Belyakov, R. Kaibyshev, H. Miura and J.J. Jonas, *Dynamic and post-dynamic recrystallization under hot, cold and severe plastic deformation conditions*, Prog. Mater. Sci. 60 (2014), pp. 130–207.

[10] F.J. Humphreys, G.S. Rohrer and A. Rollette, *Recrystallization of Two-Phase Alloys*, in *Recrystallization and Related Annealing Phenomena*, Elsevier Ltd, 2017, pp. 285–319.

[11] H.J. McQueen, E. Evangelista, J. Bowles and G. Crawford, *Hot deformation and dynamic recrystallization of Al-5Mg-O.8Mn alloy*, Met. Sci. 18 (1984), pp. 395-402.

[12] E. Cerri, E. Evangelista and H.J. McQueen, *Overview of the high temperature substructure development in Al-Mg alloys*, High Temp. Mater. Process. 18 (1999), pp. 227–240.

[13] W.M. Van Haaften, W.H. Kool and L. Katgerman, *Effect of strain rate and thermal history on the constitutive behaviour of Al-Mg alloy AA 5182*, Mater. Sci. Technol. 20 (2004), pp. 1233–1236.

[14] S. Ding, S.A. Khan and J. Yanagimoto, *Constitutive descriptions and microstructure evolution of extruded A5083 aluminum alloy during hot compression*, Mater. Sci. Eng. A 728 (2018), pp. 133–143.

[15] H.T. Jeong, S.H. Han and W.J. Kim, *Effects of large amounts of Mg (5–13 wt%) on hot compressive deformation behavior and processing maps of Al-Mg alloys*, J. Alloys Compd. 788 (2019), pp. 1282–1299.

[16] Q.S. Dai, Y.L. Deng, J.G. Tang and Y. Wang, *Deformation characteristics and strain-compensated constitutive equation for AA5083 aluminum alloy under hot compression*, Trans. Nonferrous Met. Soc. China (English Ed.) 29 (2019), pp. 2252–2261.

[17] S. Ding, S.A. Khan and J. Yanagimoto, *Flow behavior and dynamic recrystallization mechanism of A5083 aluminum alloys with different initial microstructures during hot compression*, Mater. Sci. Eng. A 787 (2020), pp. 139522.

[18] Y.J. Li and L. Arnberg, *Solidification structures and phase selection of iron-bearing eutectic particles in a DC-cast AA5182 alloy*, Acta Mater. 52 (2004), pp. 2673–2681.

[19] H.J. McQueen, S. Spigarelli, M.E. Kassner and E. Evangelista, *Hot Deformation and Processing of Aluminum Alloys*, CRC Press, 2011.

[20] X. Qian, N. Parson and X.G. Chen, *Effects of Mn content on recrystallization resistance of AA6082 aluminum alloys during post-deformation annealing*, J. Mater. Sci. Technol. 52 (2020), pp. 189–197.

[21] O. Engler, K. Kuhnke and J. Hasenclever, *Development of intermetallic particles during solidification and homogenization of two AA 5xxx series Al-Mg alloys with different Mg contents*, J. Alloys Compd. 728 (2017), pp. 669–681.

[22] X. Qian, N. Parson and X.G. Chen, *Effects of Mn addition and related Mn-containing*

dispersoids on the hot deformation behavior of 6082 aluminum alloys, Mater. Sci. Eng. A 764 (2019), .

[23] M. Shakiba, N. Parson and X.G. Chen, *Hot deformation behavior and rate-controlling mechanism in dilute Al-Fe-Si alloys with minor additions of Mn and Cu*, Mater. Sci. Eng. A 636 (2015), pp. 572–581.

[24] S. Liu, J. Chen, W. Chai, Q. Wang, Z. Yang, L. Ye et al., *Effects of Combined Additions of Mn and Zr on Dispersoid Formation and Recrystallization Behavior in Al-Zn-Mg Alloys*, Metall. Mater. Trans. A 50 (2019), pp. 4877–4890.

[25] F.J. Humphreys, *Grain and subgrain characterisation by electron backscatter diffraction*, J. Mater. Sci. 36 (2001), pp. 3833–3854.

[26] O. Engler and S. Miller-Jupp, *Control of second-phase particles in the Al-Mg-Mn alloy AA 5083*, J. Alloys Compd. 689 (2016), pp. 998–1010.

[27] Y.J. Li, W.Z. Zhang and K. Marthinsen, *Precipitation crystallography of plate-shaped Al6(Mn,Fe) dispersoids in AA5182 alloy*, Acta Mater. 60 (2012), pp. 5963–5974.

[28] A.Y. Algendy, K. Liu and X.G. Chen, *Evolution of dispersoids during multistep heat treatments and their effect on rolling performance in an Al-5 % Mg-0 . 8 % Mn alloy*, Mater. Charact. 181 (2021), pp. 111487.

[29] B. Verlinden, J. Driver, I. Samajdar and R.D. Doherty, *Softening Mechanisms*, in *Thermo-Mechanical Processing of Metallic Materials*, Elsevier Ltd, 2007, pp. 85–108.

[30] R.D. Doherty, D.A. Hughes, F.J. Humphreys, J.J. Jonas, D. Juul Jensen, M.E. Kassner et al., *Current issues in recrystallization: A review*, Mater. Sci. Eng. A 238 (1997), pp. 219–274.

[31] T. Sakai, *Dynamic recrystallization microstructures under hot working conditions*, J. Mater. Process. Technol. 53 (1995), pp. 349–361.

[32] C.M. Sellars and W.J. McTegart, *On the mechanism of hot deformation*, Acta Metall. 14 (1966), pp. 1136–1138.

[33] C. Shi and X.G. Chen, *Effect of Zr addition on hot deformation behavior and microstructural evolution of AA7150 aluminum alloy*, Mater. Sci. Eng. A 596 (2014), pp. 183–193.

[34] C. Shi and X. Chen, *Effect of vanadium on hot deformation and microstructural evolution of 7150 aluminum alloy*, Mater. Sci. Eng. A 613 (2014), pp. 91–102.

[35] B. Li, Q. Pan and Z. Yin, *Microstructural evolution and constitutive relationship of*

Al-Zn-Mg alloy containing small amount of Sc and Zr during hot deformation based on Arrhenius-type and artificial neural network models, J. Alloys Compd. 584 (2014), pp. 406–416.

[36] F.J. Humphreys and M. Hatherly, *The Deformed State*, in *Recrystallization and Related Annealing Phenomena*, Elsevier Ltd., 2004, pp. 11–65.

[37] N. Yan, Z. Li, Y. Xu and M.A. Meyers, *Shear localization in metallic materials at high strain rates*, Prog. Mater. Sci. 119 (2021), 100755.

[38] L.D. S. Martinez de la Puente, B. Verlinden, *Hot workability of an Al-Mg alloy AA5182 with 1wt% Cu*, 29 (1994), pp. 6167–6174.

[39] H.J. McQueen and J. Belling, *Constitutive constants for hot working of Al-4.5 Mg-0.35 Mn (AA5182)*, Can. Metall. Q. 39 (2000), pp. 483–492.

[40] M.A. Wells, D.J. Lloyd, I. V Samarasekera, J.K. Brimacombe and E.B. Hawbolt, *Modeling the microstructural changes during hot tandem rolling of AA5XXX aluminum alloys Part II. Textural Evolution*, Metall. Mater. Trans. A 29B (1998), pp. 621–633.

[41] H.J. McQueen, E. Fry and J. Belling, *Comparative constitutive constants for hot working of Al-4.4Mg-0.7Mn (AA5083)*, J. Mater. Eng. Perform. 10 (2001), pp. 164–172.

[42] I.C. Hsiao and J.C. Huang, *Deformation mechanisms during low-and high-temperature superplasticity in 5083 Al-Mg alloy*, Metall. Mater. Trans. A 33 (2002), pp. 1373–1384.

[43] G. Fang, J. Zhou, L. Pei-Gen and J. Duszczyk, Analysis of hot formability of Al-4.6Mg-0.6Mn alloy (AA5083), in Conference: 11th International Aluminium Conference Eindhoven, the Netherlands, 2011, pp. 431–440.

[44] A.F. Padilha and R.L. Plaut, *Work Hardening, recovery, recrystallization, and grain growth*, in *Handbook of Aluminum: Alloy production and materials manufacturing*, G.E. Totten and D.S. MacKenzie, eds., Marcel Dekker Inc., 2003, pp. 193–220.

Chapter 5: Effect of Mn on hot workability and processing map of Al-Mg-Mn alloy

Mohammadreza Mofarrehi, Mousa Javidani, X.-Grant Chen
Department of Applied Science, University of Québec at Chicoutimi, Saguenay, Québec, G7H 2B1, Canada

This article is going to be submitted in:
Journal of Materials engineering and performance

Abstract

In the present work, the impact of Mn content (0.1 to 1%) on the hot workability of Al-Mg-Mn alloys was investigated. Hot compression test was carried out at 350-500℃ /0.001-1 s^{-1} and the obtained experimental data was treated by Dynamic Material Modeling to construct the processing maps. Based on the maps, the instability region for the base alloy (0.1Mn) extended from 0.03 to 1 s^{-1} at 350 ℃, decreased by temperature, and disappeared at 450℃. Mn marginally shifted the region to higher temperatures and strain rates. Shear banding, which was one of the instability mechanisms observed to occur in the vicinity of the Fe-bearing intermetallics. The higher is the Mn content, more is the number of intermetallics and relevant shear bands. In the safe deformation zone, Mn-containing dispersoids in the high Mn alloys suppressed DRV and DRX. On the basis of the process maps, DRX governs at: I) 400℃/0.001s^{-1} and II) 500℃/1s^{-1} from which, the former was preferable of its uniformly distributed microstructure. Domain (I) lay at 350-450°C/0.001-0.007s^{-1} for the base alloy (0.1Mn) progressively decreased by Mn addition to 375-425°C/0.001-0.002s^{-1} for the 1Mn alloy.

5.1 Introduction

Owing to high strength, good weldability and excellent corrosion resistance, Al-Mg-Mn 5xxx alloys are extensively used in construction, aerospace, automotive and marine industries [1–3]. The 5xxx alloys, which are known as the non-heat treatable aluminum alloys, are usually strengthened by solid solutions with significant Mg addition (up to 5%) and strain hardening where the plastic deformation plays an essential role. The Al-Mg-Mn flat products are usually manufactured through a chain of industrial processes that consist of direct chill (DC) ingot casting, followed by homogenization and hot rolling processes. The hot rolling process is the critical step of the fabrication route, as the DC-cast ingots are usually subjected to intensive deformation. The hot rolling process facilitates the required intensive deformation process (with over 95% area reduction), by reducing the flow stress at high temperatures and activating the dynamic restoration mechanisms (e.g., recrystallization/recovery). However, the industrial hot rolling process is a complex process owing to the temperature variation in the ingots during rolling, and the competing nature of the restoration mechanism and work hardening. Therefore, to improve the productivity and to prevent the material failure, a better understanding of microstructure evolution and optimization of the operating window of the hot deformation are of primary importance.

The addition of Mn in Al-Mg-based alloys is to control the deformed microstructure and enhance the mechanical properties. [4]. During the homogenization process, a number of submicron Mn-bearing dispersoids can be precipitated in Al-Mg-Mn alloys, which can improve the mechanical strength via dispersion strengthening and strain hardening [5–8]. For instance, by increasing the Mn content from 0.4 to 1% in Al-Mg-Mn alloys, UTS was enhanced from 320 MPa to 350 MPa [5]. However, the Mn-bearing dispersoids could have a deleterious impact on the alloy ductility [9,10]. It is reported that adding 0.25 wt.% Mn addition to the binary Al-Mg alloys reduced the tensile elongation-to-failure from 325% to 146% at 400 ºC [11]. The hot workability of Al-Mg-Mn alloys is correlated with the active restoration mechanisms under different deformation conditions, namely dynamic recovery (DRV) and dynamic recrystallization (DRX) [12]. The Mn-dispersoids can remarkably inhibit DRV and DRX by hindering the substructure evolution and pinning the grain boundary migration [13–16]. In our previous study on Al-Mg-Mn alloys [17], it is shown

that with an increase in Mn content, the number density of Mn-bearing dispersoids increased and hence the flow stress increased by retarding DRX at high temperatures.

Several methods have been developed to evaluate the hot workability of metallic materials and to correlate their flow stress with microstructure evolution [18–20]The processing maps, based on the dynamic material model and developed by Prasad *et al.*[21,22] are commonly used to optimize the hot workability and metal processing. The process maps are usually established in a range of temperatures and strain rates to identify the associated hardening and softening mechanisms. The process maps are built on the power dissipation efficiency, through which the maps are correlated with the metallurgical phenomena. For instance, according to Prasad et. al. [23], dynamic recovery (DRV) and dynamic recrystallization (DRX) in Al4Mg alloy were associated with the power dissipation efficiency of 20% and 30%, respectively. Jeong *et al.* [24] stated that, by increasing the Mg level up to 7%, DRX was inhibited, because the power dissipation efficiency was reduced, while further Mg addition (up to 13%) acted in a reverse order. The process maps can also reflect the flow instabilities, which are correlated with the structural defects, such as adiabatic shear bands (ASBs) [25] and deformation bands (DBs) [26]. Shear banding caused microcracks in Al-Mg-Mn 5083 alloy under the deformation condition of 300ºC/10s^{-1}, which was consistent with the instability criterion predicted by the processing map [21]. To the best of our knowledge, a systematic investigation on the impact of Mn on hot workability and optimum processing window of the Al-Mg-Mn alloys have not been reported in literature.

In this study, the process maps were developed for four Al-Mg-Mn alloys containing 0.1-1.0 wt.% Mn. The results of the hot compression tests, which were conducted at various temperatures and strain rates, were used to build the process maps based on the dynamic material model. The processing maps were classified to instability region and safe deformation domains, and the corresponding microstructures were characterized. The underlying stability and instability mechanisms during hot deformation were discussed, and the impacts of Mn on the evolution of the instability region and the safe deformation domains were elaborated.

5.2 Experimental procedure

Experiments were conducted on Al-5Mg-Mn alloys containing 0.1, 0.4, 0.7 and 1% Mn, which covered the chemical composition range of both AA5182 and AA5083 alloys (all alloy compositions are in wt.% unless otherwise indicated). Approximately 5 kg of each material was melted in an electrical resistance furnace at 750 ℃ and then cast into a rectangular permanent mold with the dimension of 30 mm × 40 mm × 80 mm. The chemical compositions of the alloys analyzed by optical emission spectroscopy are listed in Table 1. The cast ingots were subjected to a established industrial two-step homogenisation treatment [27] prior to the deformation: the samples were heated to 420 ℃ for 2 h with a rate of 1℃/min and then continued heating to 500 ℃ for 4 h followed by water quenching at room temperature. Subsequently, cylindrical samples having a length of 15 mm and a diameter of 10 mm were machined from the as-homogenized ingots. The cylindrical samples were then hot-compressed to the strain of 0.8 by a Gleeble 3800 thermomechanical testing unite. The test temperatures were 350, 400, 450, and 500℃ at strain rate of 0.001, 0.01, 0.1, and $1s^{-1}$. The samples were first heated up to the targeted temperatures with a heating rate of 2 ℃/s, and held for 3 min to eliminate the temperature gradient. Each test condition was repeated at least three times to ensure the reproducibility of flow curves. At least one sample out of three was water quenched to preserve the deformed microstructure.

Table 5-1. The chemical compositions of studied alloys

Alloy ID	Mg	Mn	Fe	Si	Ti	Al
0.1Mn	4.67	**0.11**	0.26	0.1	0.01	Bal.
0.4Mn	4.65	**0.4**	0.28	0.09	0.01	Bal.
0.7Mn	4.74	**0.74**	0.27	0.09	0.01	Bal.
1Mn	4.7	**1.05**	0.27	0.09	0.01	Bal.

For the microstructure characterization, samples were subjected to the standard metallographic polishing procedures. The as-deformed microstructures were analyzed from the center of the axial section. To reveal the fine dispersoids and grain boundaries, etching

with 0.5%HF solution and electrochemical etching in Barker's solution were carried out, respectively. The microstructural components including primary intermetallics and dispersoids were analysed by optical microscope (Nikon, Eclipse ME600), and scanning electron microscope (SEM, JEOL JSM-6480LV) equipped with energy dispersive spectroscopy (EDS). The grain and subgrain structure of deformed samples were analyzed by electron backscattered diffraction (EBSD) at step size of 1 and 0.2 μm using HKL Channel 5 software. Accordingly, the misorientation angle of the boundaries were marked by white, blue, and black for low (LAGBs: 2°–5°), medium (MAGBs: 5°-15°), and high (HAGBs:15°<) angle boundaries, respectively [28]. The detailed microstructure was examined by a transmission electron microscope (TEM, JEOL JEM-2100) operated at an accelerating voltage of 200 kV. The TEM samples (3 mm in the diameter) were mechanically ground to a thickness of ~60 μm followed by electropolishing in a twin-jet unit operated at 20 V and -20˚C using a 30% nitric acid and 70% methanol solution.

5.3 Results

5.3.1 Initial microstructure

Fig. 5-1a and b present the optical micrographs of the alloys 0.1Mn and 1Mn; the microconstituents were mainly composed of α-Al dendrites (Al matrix) along with Mg_2Si-(appeared as black intermetallics) and Fe-rich intermetallics (gray colored). According to the EDS analyses, the Fe-rich intermetallics consisted of Al_6(Fe,Mn), Al_m(Fe,Mn), Al_3(Fe,Mn) and α-Al(Fe,Mn)Si [9,29,30]. Increasing the Mn content from 0.1 to 1% modified the plate-like β-Fe particles to the Chinese script α-Fe intermetallics. In addition, as shown in Fig. 5-1c, by increasing the Mn content (from 0.1 to 1%), the area fraction of Fe-rich particles enhanced from 0.7 to 2.7%, respectively. However, the Mn content of the alloys, had a negligible influence on the content of the Mg_2Si intermetallic, which is in consistent with the reported results in literature [6].

After homogenization, the microstructures were partially changed by partial dissolution of Mg_2Si particles and fragmentation of Fe-rich intermetallics, and more important, the precipitation of Mn-bearing dispersoids (Fig. 5-1d-f). In the base alloy (0.1Mn), almost no

dispersoid were observed in the homogenized microstructure, but in the other three alloys containing higher Mn (≥0.4%), the Mn-bearing dispersoids were formed and uniformly distributed in the interiors of the dendrite cells/grains (Fig. 5-1d-e). The details of the type, morphology, and distribution of Mn-bearing dispersoids were described in our previous work [17]. As presented in Fig. 5-1f, the higher was the Mn content of the alloys, the greater was the number density of the dispersoids. Furthermore, by increasing the Mn content, the dispersoids became finer with a reduced interparticle spacing (refer to the inserts of Fig. 5-1d-e). Owing to the increased number density of dispersoids with Mn, the HV was enhanced from 76 Hv in the base alloy to 88 Hv in the alloy of 1%Mn (Fig. 5-1f). However, unlike the dendrite interiors, there were almost free of dispersoids in the interdendritic regions, which were denoted as dispersoid free zones (DFZ, marked with the dotted-lines in Fig. 5-1e).

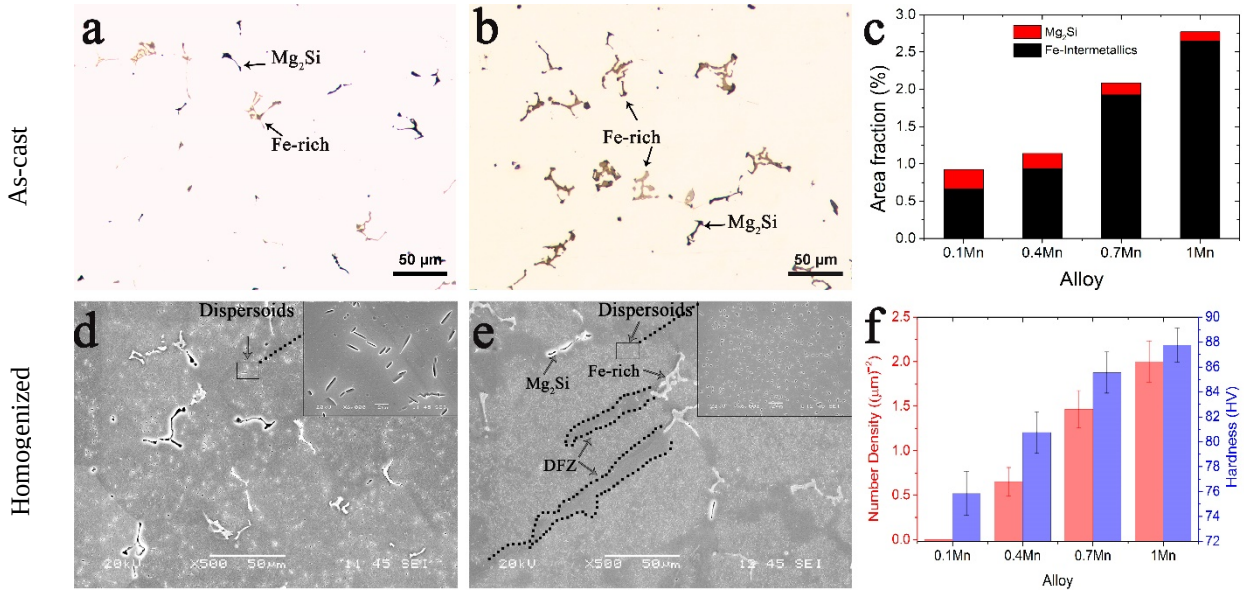

Fig. 5-1: Optical micrographs of the (a) 0.1Mn and (b) 1Mn alloy indicating the main intermetallics in the as-cast state which are quantitatively compared in (c). SEM images of (d) 0.4Mn, and (e) 1Mn etched in 0.5%HF to demonstrate the distribution of dispersoids correlated to Mn addition with clearer illustration of magnified region in the insets. (f) compares the dispersoids distribution with hardness.

5.3.2 Flow stress behavior

A series of true stress-true strain (σ-ε) curves of four studied alloys, obtained by hot compression at the temperature range of 350-500 °C and strain rates of 0.001-1 s^{-1}, are presented in Fig. 5-2. After a rapid raise of the flow stress at the small strains, the curves

reached to the peak stress. By further straining after the peak, the curves were either remained almost constant, or followed by a gradual drop of the flow stress. The hot working conditions (i.e., temperatures and strain rates) had a remarkable impact on the flow behaviors of Al-Mg-Mn alloys. For instance, as the strain rate increases and deformation temperature decreases, the flow stress increases, which agrees with the general trend in aluminum alloy during hot deformation [31]. At the low strain rates, longer time is available for thermally activated energy and diffusion, while the higher deformation temperatures provide greater mobility at the grain boundary for recrystallization and dislocation annihilation.

The deformation condition plays a remarkable role for the impact of Mn on the flow curve tendency and peak stress. At the low temperatures and high strain rates, the impact of Mn on the flow stress was almost negligible; for instance, at the deformation condition of 400 °C and 1 s^{-1}, by increasing the Mn content from 0.1 to 1wt.%, the peak stress was enhanced from 131 to 137 MPa (i.e., ~ 4%). However, at high deformation temperatures and low strain rates, the impact of Mn was significant; for instance, at the deformation condition of 450 °C and 0.001 s^{-1}, by increasing the Mn content from 0.1 to 1%Mn, the peak stress was enhanced from 18 to 23 MPa (i.e., ~ 28%).

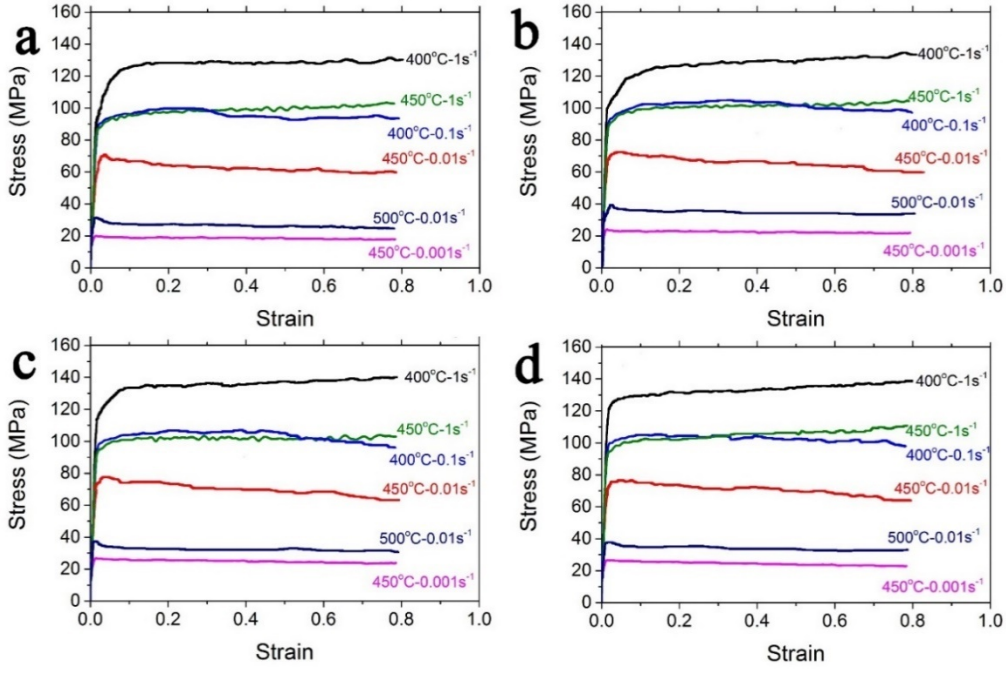

Fig. 5-2: Typical true stress-true strain curves obtained from hot compression test: (a) 0.1Mn (b) 0.4Mn, (c) 0.7Mn, (d) 1Mn.

5.3.3 Establishment of processing maps

5.3.3.1 Calculation of η and ξ($\dot{\varepsilon}$)

Dynamic Material Model (DMM) is usually applied to develop the hot processing map through the superposition of power dissipation efficiency map and instability map using the data derived from stress-strain curves [21,22]. Introduced by Prasad et. al. [22], the processing map represents the response of the material in terms of microstructure evolution for the imposed strain at a range of strain rates and deformation temperatures studied.

In the DMM, the total power P dissipated in a workpiece at any given strain and temperature, consists of two complementary parts. One part is G that represents the energy dissipation through plastic deformation, most of which changes into heat and increases the temperature of the workpiece. The other part is J that manifests the co-content power dissipation through microstructure transition, namely dynamic restoring mechanisms (DRV, DRX), phase transformations, and deformation defects. Therefore, the total power dissipation is expressed as [22]:

$$P = \sigma\dot{\varepsilon} = G + J = \int_0^{\dot{\varepsilon}} \sigma d\dot{\varepsilon} + \int_0^{\sigma} \dot{\varepsilon} d\sigma \quad \text{Eq. 5-1}$$

where $\dot{\varepsilon}$ is the strain rate (s^{-1}) and σ is the stress (MPa). The efficiency of power dissipation (η) demonstrates how the intrinsic energy dissipates efficiently by microstructural evolution during hot deformation which is defined as:

$$\eta = \frac{J}{J_{max}} = \frac{1-G}{J_{\max}} = 2\left(1 - \frac{1}{\sigma\dot{\varepsilon}}\int_0^{\dot{\varepsilon}} \sigma d\dot{\varepsilon}\right) \quad \text{Eq. 5-2}$$

where J_{max} is the maximum value equal to P/2.

In this model, partitioning of G and J can be expressed by the strain rate sensitivity (m) [33] given as follows:

$$m = \left[\frac{\partial J}{\partial G}\right]_{\varepsilon,T} = \left[\frac{\dot{\varepsilon}\partial\sigma}{\sigma\partial\dot{\varepsilon}}\right]_{\varepsilon,T} = \left[\frac{\partial ln\sigma}{\partial ln\dot{\varepsilon}}\right]_{\varepsilon,T} \quad \text{Eq. 5-3}$$

where ε is the true strain. The m values were extracted from the slope of the $ln\sigma - ln\dot{\varepsilon}$ plot. For the given strain and deformation temperature, the flow stress can be calculated as [22]:

$$\sigma = K\dot{\varepsilon}^{m} \quad \text{Eq. 5-4}$$

Subsequently via combination of Eq. 5-1 and Eq. 5-4, J can be expressed as:

$$J = \sigma\dot{\varepsilon} - \int_0^{\dot{\varepsilon}} \sigma d\dot{\varepsilon} = (\sigma\dot{\varepsilon})(\frac{m}{m+1}) \quad \text{Eq. 5-5}$$

then Eq. 5-2 can be rewritten as:

$$\eta = \frac{J}{J_{max}} = \frac{(\sigma\dot{\varepsilon}\times(\frac{m}{m+1}))}{(\frac{\sigma\dot{\varepsilon}}{2})} = \frac{2m}{m+1} \quad \text{Eq. 5-6}$$

Another criterion that Prasad et. al. [22] developed to constitutively express the material behavior is flow instability which is dimensionless parameter defined as:

$$\xi(\dot{\varepsilon}) = \frac{\partial ln[m/(m+1)]}{\partial ln\dot{\varepsilon}} + m < 0 \quad \text{Eq. 5-7}$$

In the instability regions including adiabatic shear bands, flow localization regions, and deformation bands which are characterized by the negative $\xi(\dot{\varepsilon})$ values, failure is highly predictable thus deformation processing is undesirable.

5.3.3.2 Processing map zoning

Fig. 5-3 presents the 2D processing maps of the four studied alloys (i.e., 0.1, 0.4, 0.7 and 1Mn) at the strain of 0.8. To plot these maps, the instability diagrams were superposed on the power dissipation diagrams. According to the instability criterion, the shadowed area ($\xi < 0$) in the processing maps stands for the instability region, and the rest are the safe deformation zone. The contour numbers of the maps, ranged from 10 to 47%, indicate the values of power dissipation efficiency (η). The values of the power dissipation efficiency (η) tends to increase by rising deformation temperature and reducing the strain rate.

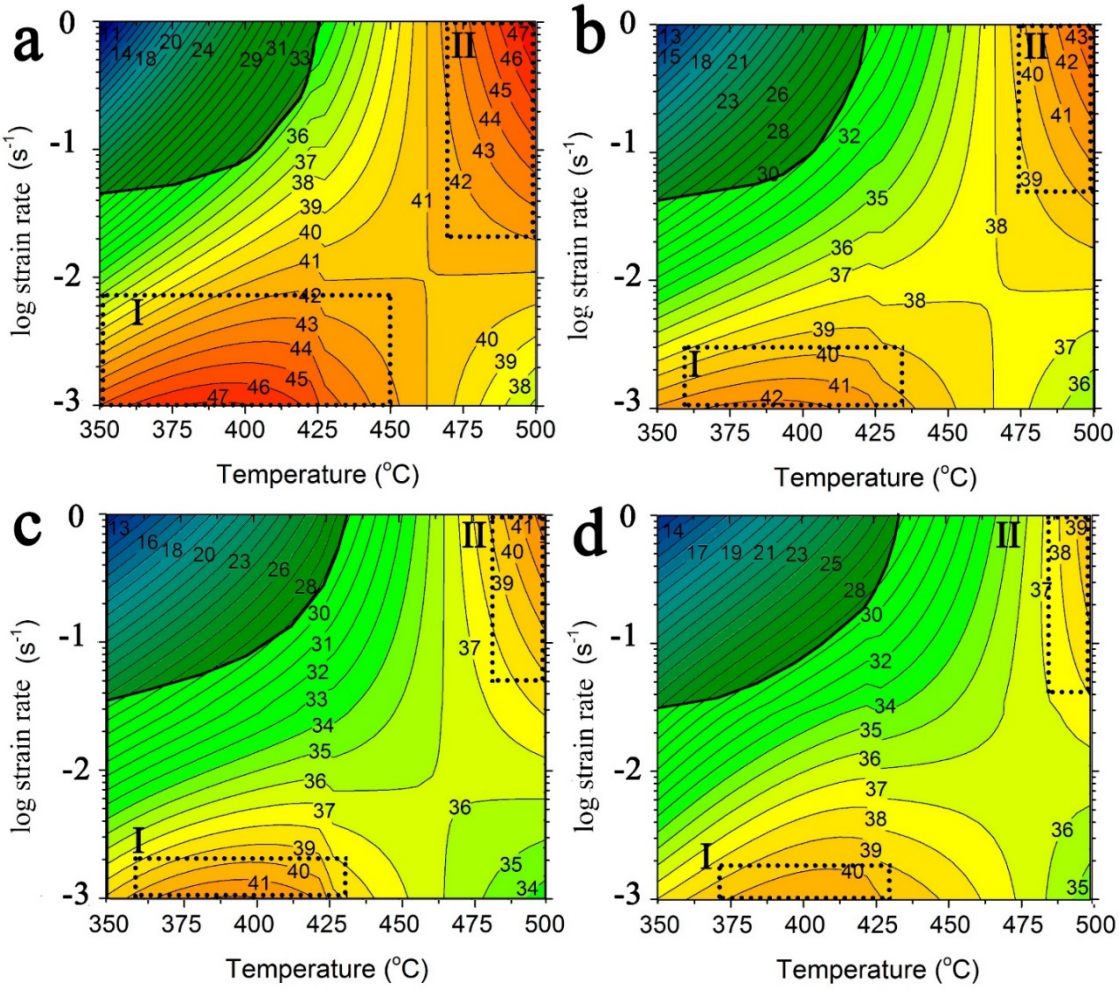

Fig. 5-3: The processing maps developed at true strain of 0.8 for four alloys, (a)0.1Mn, (b)0.4Mn, (c)0.7Mn, and (d)1Mn. The shadowed region is denoted to the instability regions.

The instability regions were established at the same location of the map (i.e., top left) for all the studied alloys, however, the more the Mn content, the larger was the area of the regions. For the base alloy (0.1Mn), the region was emerged between the strain rate of ~0.05-1 s^{-1} at 350 °C, which was narrowed down to the strain rate of 1 s^{-1} as the deformation temperature raised to 425 °C. By increasing the Mn content (to 1%), the instability regions were enlarged to the strain rates of 0.03-1 s^{-1} at 350 °C and extended to higher temperatures 435 °C.

As shown in Fig. 5-3, the peak power dissipation efficiencies (η) were located in a similar place for all the studied alloys: the first one appeared at a relatively lower temperature/strain rate (i.e., 400°C/0.001s^{-1}), and the second one was observed at the maximum applied temperature/strain rate (i.e., 500°C/1s^{-1}). Accordingly, two power

dissipation domains can be identified for each alloy in the maps. For the 0.1Mn, domain I was emerged between 350-450 °C and the strain rates of 0.001-0.007s^{-1}; and domain II appeared between 460-500°C °C and the strain rates of 0.02-1s^{-1}. By increasing the Mn content, the peak power dissipation efficiency (η) was reduced from 47% (0.1Mn alloy) to 39% (1Mn alloy). Furthermore, both domains (I and II) were shrunk by increasing Mn content. For instance, in 1Mn alloy, domain I was restricted to 375-425°C and the strain rates of 0.001-0.002s^{-1}; and domain II was limited to 480-500°C and strain rates of 0.04-1s^{-1}.

5.3.3.3 Effect of strain on processing map

To evaluate the effect of strain on processing map, the alloys with 0.1% and 1% Mn were further investigated at the strains of 0.2, 0.4 and 0.8, and the results are displayed in Fig. 5-4. For the 0.1Mn alloy (Fig. 5-4a), with increase in the strain (from 0.2 to 0.8), the instability region was shifted to higher strain rates (from 0.01 s^{-1} to 0.03 s^{-1}) and higher temperatures (from 410 to 425 °C). The peak power dissipation efficiency (η) exhibited remarkable changes by increasing the strain. Moreover, for the strain of 0.2, a single domain (with η=52%) was observed at 425°C/0.001s^{-1}; however, by increasing the strain to 0.4, the peak power dissipation efficiency of domain I was reduced to η=42%, and domain II (with η=46%) appeared at 500°C/1s^{-1}. By further increasing the straining (to 0.8), the peak power dissipation efficiency was raised to 47% in both domains (I and II).

Unlike the 0.1Mn alloy, in the case of 1Mn alloy (Fig. 5-4b), with increase in the strain (from 0.2 to 0.8), the instability region was shifted to higher strain rates (from 0.01 s^{-1} to 0.02 s^{-1}) and lower temperatures (from 440 to 435 °C). By increasing the Mn content to 1%, the impact of increasing strain (from 0.2 to 0.8) on power dissipation evolution presented a similar trend as 0.1Mn; however, the peak power dissipation efficiencies were significantly reduced by increasing the Mn content to 1%. For the strain of 0.2, a single domain (with η=43%) was observed at 425°C/0.001s^{-1}. By increasing the strain to 0.4, the peak power dissipation efficiency of domain I was reduced to η=37%, and domain II (with η=40%) appeared at 500°C/1s^{-1}. By further straining to 0.8, the peak power dissipation efficiency was raised to 40% in both domains (I and II).

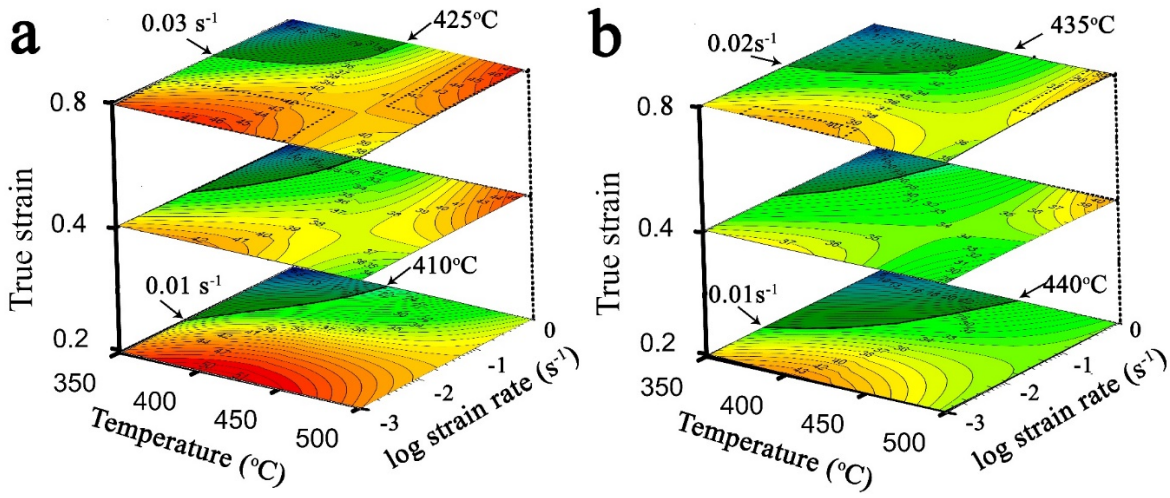

Fig. 5-4: 3D diagram of the processing maps, (a) 0.1Mn and (b) 1Mn alloys showing the effect of the strain.

5.3.4 Microstructure evolution

To investigate the influence of Mn addition on microstructure evolution in the instability regions and safe zones, several typical deformation conditions were selected and their corresponding deformed samples were analyzed, as shown in Fig. 5-5. Two deformation conditions (i.e., A and B in Fig. 5-5) from the instability region, and three deformation conditions (i.e., C, D and E) from the safe zone were selected for the microstructure analysis, and the results are presented in the following sections.

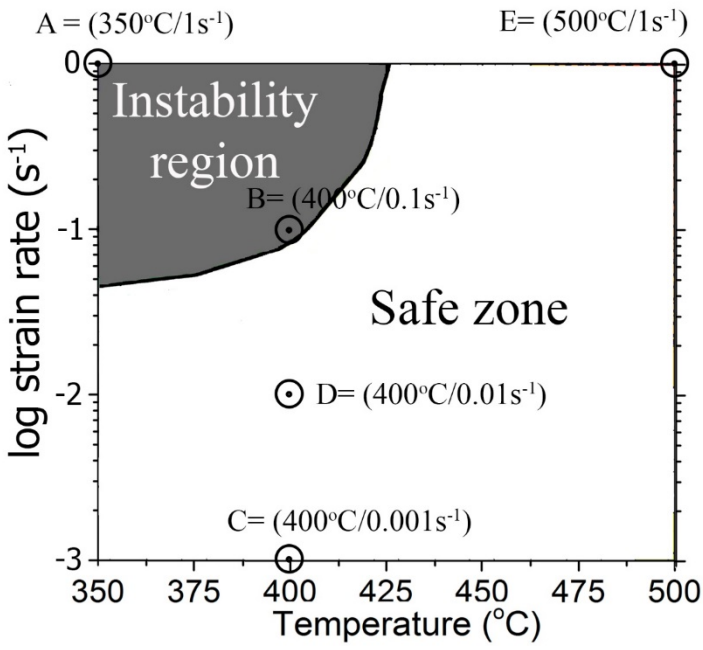

Fig. 5-5: The selected deformation conditions in the processing map for microstructure analysis.

5.3.4.1 Instability region

The typical optical micrographs of the deformed samples (0.1Mn and 1Mn) at the instability region (locations A and B in Fig. 5-5) are displayed in Fig. 5-6. The elongated grain structure perpendicular to the compression direction were seen in all these micrographs. Furthermore, the original grain structure of all the studied alloys were intensively torn and broken into irregular deformation bands (DBs). The deformation bands, as the characteristic of the instability regions, are observed inside the individual grains (marked by the black arrows). Those bands are usually formed either by the inhomogeneous deformation of the grains due to the concentrated stress at the adjacent grains, or by the intrinsic instability of the grains during deformation. In addition to the deformation bands, other microstructural inhomogeneities (e.g. shear bands) were also observed close to the intermetallic particles (marked by the green arrows). As shown in Fig. 5-6c-d, the deformation bands could be still detected at the boundary between the instability region and safe zone (location B, 400 °C/0.1 s^{-1}). However, at the deformation condition, the number density of the deformation bands was significantly reduced. It is worth to mention that no sign of DRX was seen in the instability regions of the studied alloys.

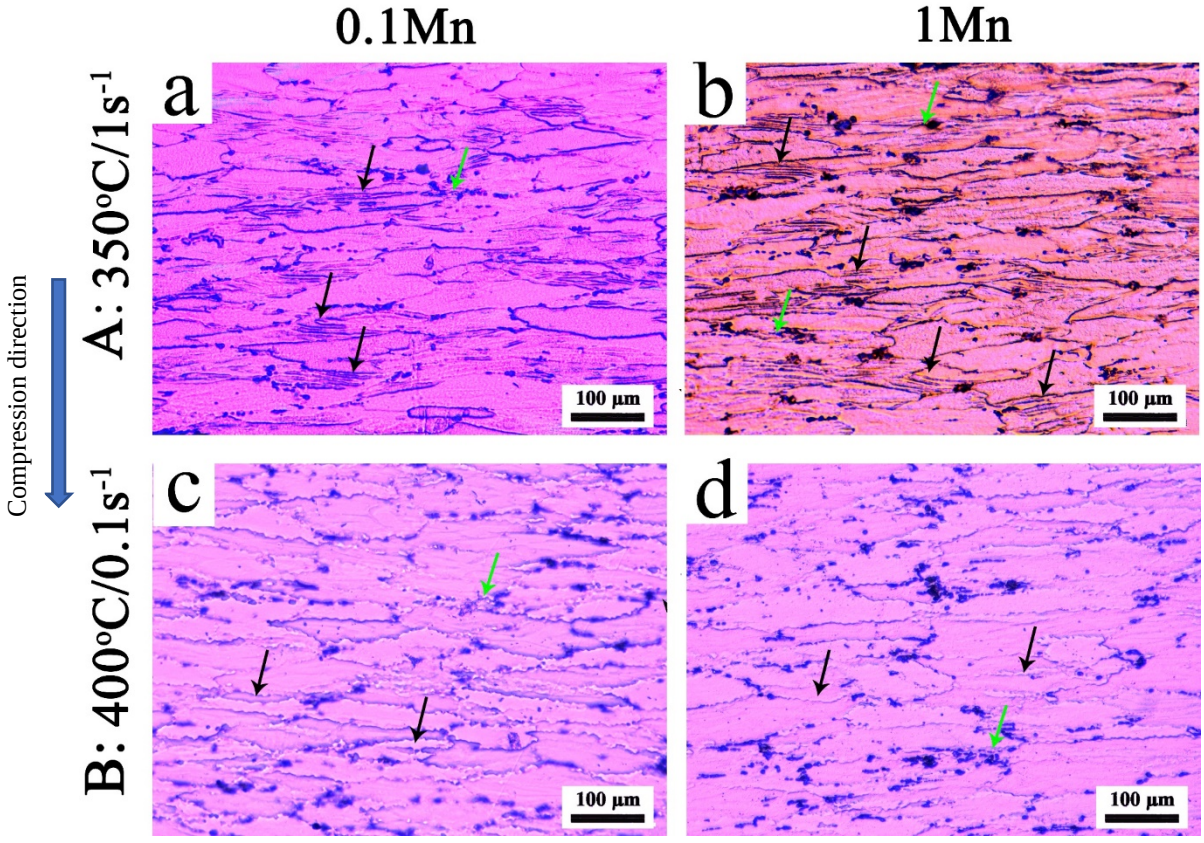

Fig. 5-6: Optical microphotographs (electrochemically etched) of deformed samples in the instability region, (a) 0.1Mn and (b) 1Mn alloys under 350°C/1s^{-1} condition, (c) and (d) 0.1Mn and 1Mn alloys under 400°C/0.1s^{-1}, respectively. Compression direction is perpendicular to the

5.3.4.2 Safe deformation zone

The peak power dissipation domains in the safe zone (i.e., I and II), which had the peak efficiencies $\eta > 40\%$, can be associated with the superior microstructural restoration over the course of the hot deformation. The microstructure investigations were carried out by EBSD analysis to reveal the predominant restoration mechanisms in the safe zone (i.e., domains I and II, and transition area).

5.3.4.2.1 Domain I (400°C/0.001s^{-1})

The EBSD orientation maps of the 0.1Mn and 1Mn samples are presented in Fig. 5-7a-b, respectively, for which the deformations were conducted at 400 °C and 0.001 s^{-1} (location C in Fig. 5-5). Fig. 5-8 shows the quantitative results of recrystallization fraction and recrystallized grain distribution for all four alloy studied. For the 0.1Mn alloy (as shown in

Fig. 5-7a), the microstructure was comprised equiaxed grains surrounded by medium angle- and high angle boundaries developed within the original grains. The equiaxed grains with very low internal substructures, revealed that the DRX was the dominant restoration mechanism at this condition. By increasing the Mn content to 1% (Fig. 5-7b), the microstructure was mostly composed of the pancaked and elongated grains perpendicular to compression direction. Some new equiaxed grains and subgrains can be seen in the DFZs of the grain boundaries and triple junctions. As shown in Fig. 8, by increasing the Mn content (from 0.1 to 1%), the fraction of the recrystallized grains was remarkably reduced (from 65% in 0.1Mn to 23% in 1Mn). Furthermore, the fraction of the large recrystallized grains (>5μm) were also reduced from 84% (in 0.1Mn) to 38% (in 1Mn). Consequently, one can conclude that the DRX and grain coarsening were highly prevented in the alloys containing high Mn due to the presence of Mn-bearing dispersoids.

5.3.4.2.2 Domain II (500℃/1s^{-1})

The EBSD orientation maps of the 0.1Mn and 1Mn alloys deformed at 500°C/1s^{-1} (location D in Fig. 5-5) are shown in Fig. 5-7 e and f, respectively. In both alloys, the original grains were elongated perpendicular to compression direction. The recrystallization mainly occurred around the grain boundaries, which were intensively surrounded by fine equiaxed recrystallized grains (marked by the white arrows). The fraction of the recrystallization and the distribution of recrystallized grains are shown in Fig. 5-8. Actually, all four alloys studied experienced a partial DRX at this deformation condition; however, in the alloy containing high Mn content, the DRXs were reduced (from 28% in 0.1Mn to 20% in 1Mn). Furthermore, the fraction of large grains (>5μm), which were 34% in the 0.1Mn alloy, were remarkably reduced to 12% in 1Mn alloy. Thereby, it is reasonable to conclude that the Mn-containing dispersoids exhibited a strong pinning effect on the grain growth and grain boundary migration at this deformation condition (500°C/1s^{-1}).

5.3.4.2.3 Transition area

With increasing the strain rate to 0.01s^{-1} at 400 °C (location E in Fig. 5-5), this is a typical transition area located between domains I (400°C/0.001s^{-1}) and II (500°C/1s^{-1}). Fig.

5-7c and d illustrate the microstructure evolution of 0.1Mn and 1Mn alloys at the transition zone. The original grains, elongated in the compression direction and surrounded by the fine equiaxed grains, can be observed. Fig. 5-8 provides the quantitative results on the distribution of recrystallized grains. It can be found that that the fraction of recrystallized grains is considerably lower than the one in Domain I, and slightly higher than the one in Domain II for all four alloys studied. Furthermore, the DRX was remarkably inhibited by the Mn-dispersoids in the high Mn-containing alloys; for instance, the DRX fraction were gradually reduced from 33% (in 0.1Mn alloy) to 16% (in 1Mn alloy). In addition, the fraction of the large recrystallized grains (>5μm) was reduced from 51% (in 0.1Mn alloy) to 28% (in 1Mn alloy). The intensive substructure inside the elongated grains and low recrystallization in 1Mn alloy, reveal that DRV was the predominant restoration mechanism in the alloys containing high Mn content.

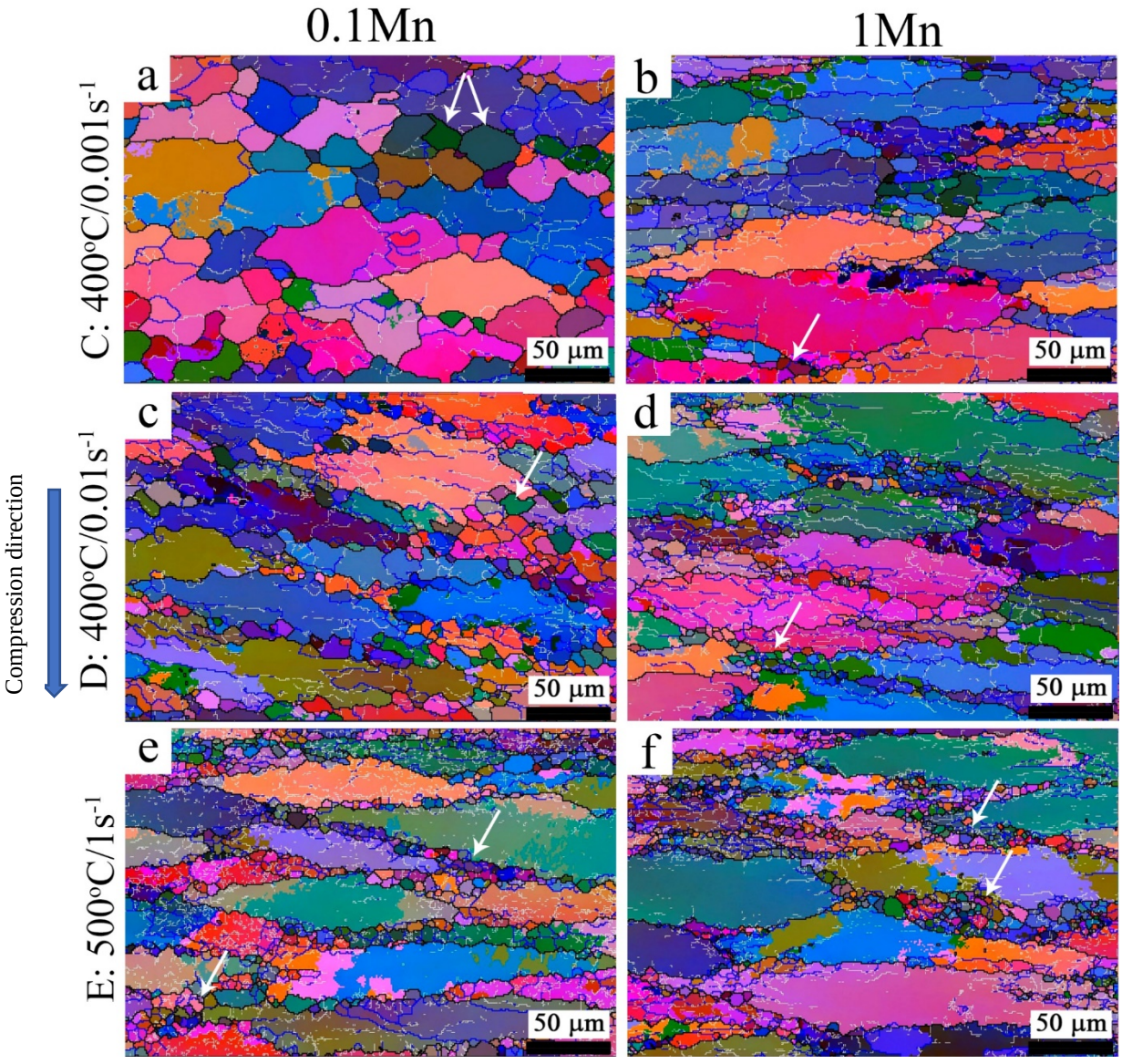

Fig. 5-7 All Euler orientation maps of 0.1Mn and 1Mn samples deformed in different domains ; (a) and (b) Domain II (500℃/1s-1), (c) and (d) Transition area (400℃/0.01s-1), and (e) and (f) Domain I (400℃/0.001s-1). White lines (2°–5°), blue lines (5°-15°), and black lines (>15°).

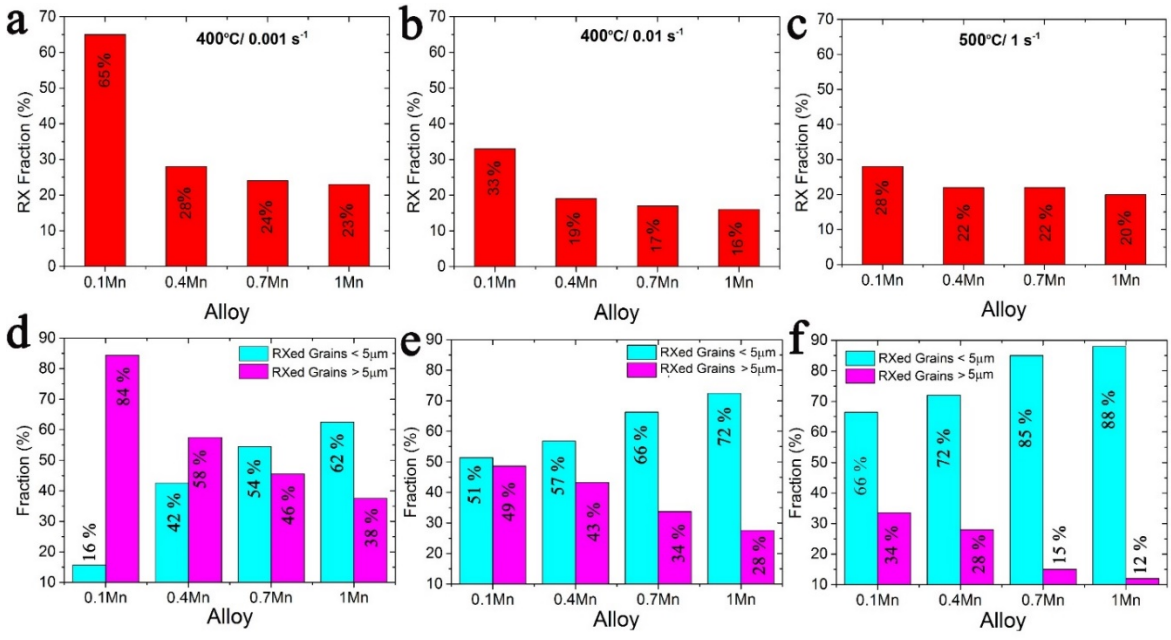

Fig. 5-8: Quantitative measurement of grain distribution and recrystallized fraction for all studies alloys at (a)(d) 400℃/0.001s^{-1} , (b)(e) 400℃/0.01s^{-1}, and(c)(f) 500℃/1s^{-1}

5.4 Discussion

To validate the processing map predictions, typical regions/domains in the processing map are interpreted in terms of its instability (ξ) and efficiency of power dissipation (η) in accord with related microstructural evolution. In the safe deformation conditions (ξ > 0), there are two domains with peak η values. Mn has a significant impact on the instability and the evolution of peak power dissipation domains.

5.4.1 Effect of Mn on the instability region

In the instability region, the flow instability was mainly caused by the deformation and sheer bands, as demonstrated in Fig. 5-6. A close examination of such bands was further carried out using the EBSD analysis (Fig. 5-9). The deformation bands (marked white arrows) displayed in different colors from elsewhere in the grain interiors owing to their local misorientation [33]. The microstructural examination showed that deformation bands existed in the instability region of all four alloys studied irrelevant to the Mn content. The flow localization in the form of accumulative substructure within the grains (the blue dashed

rectangles in Fig. 5-9a and b) showed that few grains in the base alloy (0.1Mn) were harshly distorted. At low deformation temperatures, the stress localization tends to occur in some grains as the consequence of the competition between work hardening and thermal softening. Such inhomogeneously stored strain was accompanied by a simultaneous heat localization, which promotes the configuration of high energy dislocations in cell boundaries [34]. Subsequently, the formed cells rotated and elongated progressively to evolve to subgrains, which concurrently underwent straining until breaking up [35].

With increasing Mn content, the number of deformation bands increased. In addition, the sheer bands were often observed (the black-dashed rectangles in Fig. 5-9c and d), which were formed by creating a large amount of tiny, recrystallized grains along the original grain boundaries (Fig. 5-9d and e). Such process was known as adiabatic shearing [34–36], and intensified by hard intermetallic particles embedded in the grain boundaries, which provoked the stress concentration at their neighborhood [37]. The enlarged EBSD map with a fine step size of 0.2 μm (Fig. 5-9e) provided a clear evidence of many fine grains formed near the intermetallic particles along the grain boundaries. Because the Mn increased the amount of Fe-rich intermetallics (Fig. 5-1), the high Mn-containing alloys experienced more shear bands relative to the base alloy. Owing to increase numbers of the deformation and shear bands, the instability region extended with increasing Mn content (Fig. 5-3), leading to a reduction of hot workability. It is worth to mention that the deformation and shear bands are the microstructural defects to be prone to the crack initiation and material failure during the plastic forming [38].

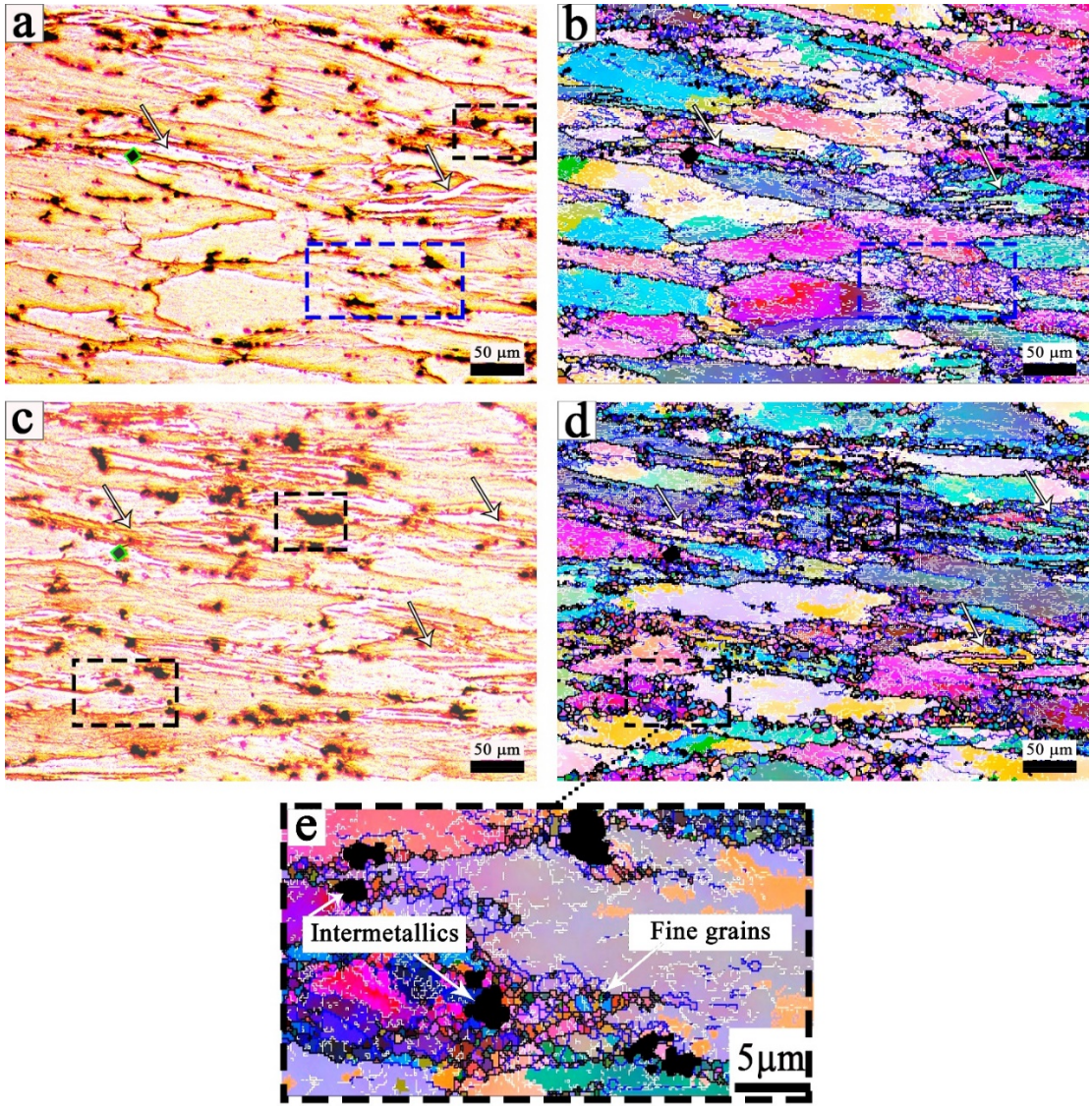

Fig. 5-9: Optic images and correspondent all Euler maps of samples deformed at 350℃/1s^{-1}showing the deformation and shear bands, (a-b) 0.1Mn and (c-d) 1Mn alloy, (e) High resolution EBSD mapping of black dashed rectangular of Fig. 5-8d.

5.4.2 Impact of Mn on the safe deformation zone

The increase in the Mn level from 0.1% to 1% made the change of the η value range from 35-47% (0.1Mn alloy) to 30-40% (1Mn alloy) in the safe deformation zones (Fig. 3). This decrease is related to the impact of Mn-bearing dispersoids on the retardation of substructure motion and reconstitution of microstructure in high Mn-containing alloys. The dispersoids act as barriers against dislocation motion and reduce the effectiveness of DRV

[31]. However, the major impact of Mn and dispersoids was on Domains I and II in the processing maps.

5.4.2.1 Impact of Mn on Domain I

The low strain rates and high temperatures of Domain I (400°C/0.001s^{-1}) provide an appropriate condition for substructure migration. In the base alloy, the mobile dislocations continuously pile up at the grain boundaries where they polygonize into the subgrain boundaries (Fig. 5-10b) a). These subboundaries evolve to high angle boundaries by entering more dislocations as the deformation progresses [39]. Due to the adequate energy and time, boundaries migrate at the expense of dislocations and grow the new grains [24,39,40] (Fig. 5-10b). Therefore, the microstructure of the base alloy contains large equiaxed recrystallized grains observed in the map of Fig. 5-7. The dislocation consumption by boundaries effectively dissipates the energy (47%), which is consistent with Prasad's finding (35-45%) obtained from the hot compression of Al-4Mg alloy [41].

The Mn-bearing dispersoids in high Mn-containing alloys substantially obstruct the mobility of the substructure. As illustrated in Fig. 5-10c, the array of dislocations is in the course of by-passing a dispersoid and detachment of its strain field. Moreover, dispersoids effectively retard the boundary migration and the advancement of grains (Fig. 5-10d). Both effects reduce subgrain formation and evolution, lowering the η value to 40% in high Mn alloys (0.7-1Mn). Therefore, the microstructure of high Mn alloys mainly consists of recovered original grains with some recrystallization at the DFZs (Fig. 5-7b). In all studied alloys, at higher temperatures (i.e. 475-500℃) where dislocations prefer to annihilate rather than being consumed by boundaries [39], the input energy dissipates by thermal diffusion instead of being utilized for the evolution of the microstructure [42,43]. Consequently, the relaxation of DRX is replaced with that of DRV, which is comparatively subordinate.

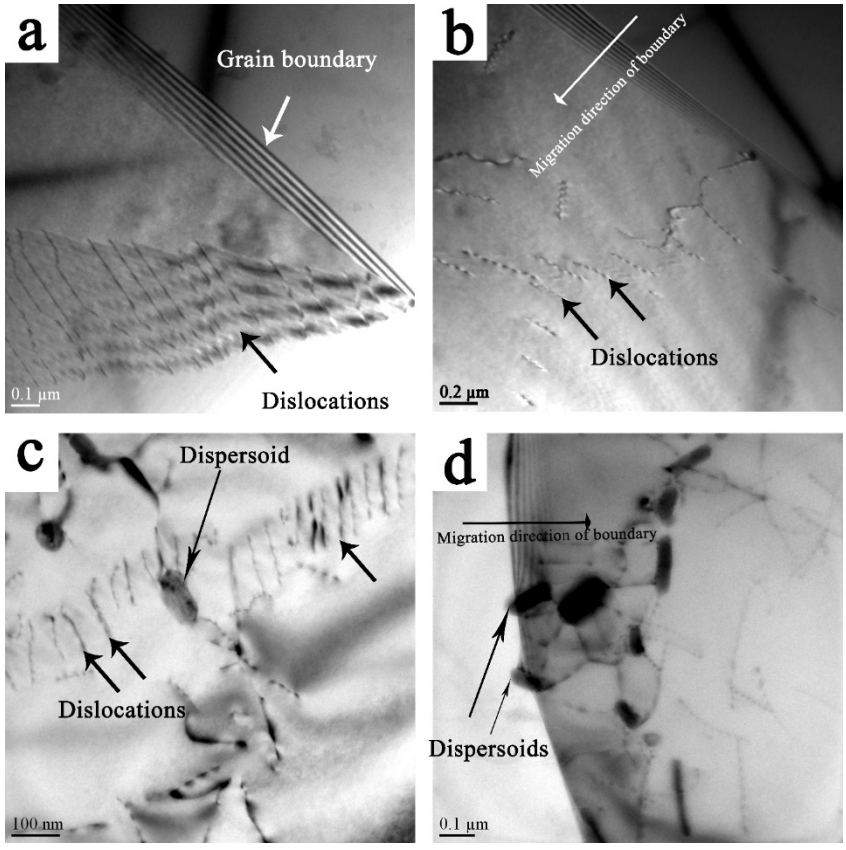

Fig. 5-10: Bright-filed TEM microimages showing (a) rearrangement of dislocations and (b) grain boundary migration in the 0.1Mn alloy. Dispersoid in 0.7Mn acts as an obstacle against (c) mobile dislocations and (d) grain boundary migration.

5.4.2.2 Impact of Mn on Domain II

Dissimilar to the low strain rate (0.001 s^{-1} in Domain I), the strain preferentially accumulated in the vicinity of grain boundaries at the high strain rate (1 s^{-1} in Domain II) [44]. Owing to the thermal activation at the high temperature (500 °C), the stored energy was mainly released by polygonization of piled-up dislocations forming fine grains and subgrains [17]. Thus, DRX mostly occurred around the grain boundaries and triple junctions, where new grains formed. The higher is the straining, more will be the driving force for recrystallized grains to form. Also, the high temperature promotes grain boundary mobility and grain coarsening [39]. In the base alloy (0.1Mn), the recrystallized grains can grow and consume the dislocations. However, in the high Mn-containing alloys, the dislocations mainly accumulated in the vicinity of the grain boundaries where the dispersoid free zones (DFZ) located to form fine subgrains and grains. The recrystallization was restrained to the narrow DFZs because the high number density of dispersoids in the grains did not allow the

boundaries migration toward the grain interior. In addition, the high pinning effect of dispersoids inhibited grain coalescence. Therefore, the power dissipation in the coarse recrystallized structure (0.1Mn base alloy) is higher than that in the fine recrystallized one (three high Mn containing alloys).

5.4.3 Optimum hot working conditions

Fig. 5-11 displays a schematic diagram illustrating the impact of Mn on the hot workability of 5xxx alloys. Two peak power dissipation domains were identified at 400℃/0.001s^{-1} and 500℃/1s^{-1}, which were considered as favorable hot working conditions governed by DRX. With 0.1%Mn, DRX effectively served at both domains, and thus the optimum hot working conditions were at the wide range of temperature and strain rate. With Mn addition to 0.4 and precipitation of Mn-bearing dispersoids, DRX was gradually suppressed, and the optimum conditions shifted to the narrow range of temperature and strain rate. The high number density of dispersoids with increased Mn toward 1% yielded the stronger interaction with substructure, which shrunk the optimum hot working conditions to even lower temperatures and strain rates. For the 0.1Mn base alloy, the recommended optimum condition to achieve a uniform microstructure (Domain I) is 350-450°C/0.001-0.007s^{-1}. The optimum hot working condition progressively decreased with increase Mn content, and went down to 375-425°C/0.001-0.002s^{-1} (Domain I) for 1Mn alloy. Domain II shows the same tendency as Domain I, namely it shrunk towards the narrow range of temperature and strain rate with increasing Mn level. However, as observed in Fig. 7, uneven microstructure in Domain II including the accumulation of tiny recrystallization grains around the grain boundaries was less desirable than in Domain I.

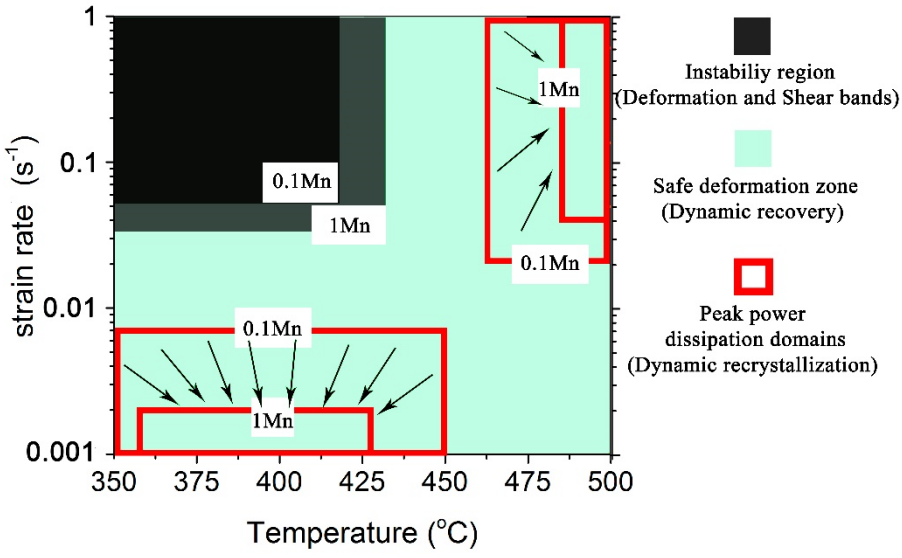

Fig. 5-11: A schematic diagram demonstrating the impact of Mn on the hot workability.

5.5 Conclusion

1. With increasing Mn from 0.1 to 1%, the volume of iron-rich intermetallics increases, so does the number density of dispersoids. The Mn content of 0.1% is not adequate for dispersoid precipitation, while with 0.4% Mn long plate-like and fine dispersoids are formed. Further increase in Mn level refines the dispersoids and increases their number density in the dispersoid accumulated zones.
2. Flow instability during hot deformation of Al-Mg-Mn alloys occurred between 0.03-1 s^{-1} at 350 ℃, which decreased by temperature and disappeared at 450℃. The instability region in the processing map is attributed to the formation of deformation and shear bands. With increasing Mn level, the instability region moderately extended.
3. The processing maps of Al-Mg-Mn alloys at strain of 0.8 exhibited two domains with peak power dissipation efficiency, which occurred at 400℃/0.001s^{-1} (Domain I) and 500℃/1s^{-1} (Domain II). In both domains CDRX dissipates the applied power by forming fine new grains at the grain boundaries in the former but coarser and uniformly distributed grains in the latter domain. In Domain I for high Mn alloys, recrystallization was suppressed to the DFZ regions because of the pinning effect of dispersoids. At the grain boundaries d In Domain I, CDRX effectively dissipated the energy (35-47%) of dislocations, while CDRX was mostly through the polygonization of piled-up

dislocations forming new grains along original grain boundaries and triple junctions in Domain II.

4. The processing map evolved with increase strain during hot deformation. With the increase in strain, the instability region marginally shifts to higher strain rates and temperature. As strain reached to 0.4, one more Domain (II) appeared in addition to the existing Domain I.
5. Domain I was more preferable compared to Domain II in terms of microstructural uniformity. The optimum hot working condition was defined at 350-450°C/0.001-0.007s^{-1} for the base alloy with 0.1% Mn. It progressively decreased with increasing Mn content, and shrunk down to 375-425°C/0.001-0.002s^{-1} for the 1% Mn alloy, owing to the strong pinning effect of Mn-containing dispersoids on grain boundary migration.

5.6 References

[1] J. Hirsch, *Aluminium in Innovative Light-Weight Car Design*, Mater. Trans. 52 (2011), pp. 818–824.

[2] J. Hirsch, *Aluminium sheet fabrication and processing*, in *Fundamentals of Aluminium Metallurgy: Production, Processing and Applications*, Woodhead Publishing Limited, 2010, pp. 719–746.

[3] J. Hirsch, *Recent development in aluminium for automotive applications*, Trans. Nonferrous Met. Soc. China 24 (2014), pp. 1995–2002.

[4] W.M. Mao, G.E. Totten and D.S. MacKenzie, *Handbook of Aluminum: Vol. 1: Physical Metallurgy and Processes*, Marcel Dekker Inc., 2003.

[5] Y.L. Liu and S.B. Kang, *Influence of manganese on microstructure and solidification behaviour of aluminium-magnesium alloys*, Mater. Sci. Technol. 12 (1996), pp. 12–18.

[6] Y. Liu, G. Huang, Y. Sun, L. Zhang, Z. Huang, J. Wang et al., *Effect of Mn and Fe on the formation of Fe- and Mn-rich intermetallics in al-5Mg-Mn alloys solidified under near-rapid cooling*, Materials (Basel). 9 (2016), pp. DOI:10.3390/ma9020088.

[7] S.W. Choi, Y.C. Kim, C.S. Kang, J.M. Jung and S.K. Hong, *Effects of Mn and Ca additions on microstructure and mechanical properties of Al-Mg alloy*, Adv. Mater.

Res. 813 (2013), pp. 427–430.

[8] Y. Liu, L. Ou, C. Han, L. Zhang and Y. Zhao, *The influence of Mn on the microstructure and mechanical properties of the Al-5Mg-Mn alloy solidified under near-rapid cooling*, J. Mater. Res. 31 (2016), pp. 1153–1162.

[9] O. Engler and S. Miller-Jupp, *Control of second-phase particles in the Al-Mg-Mn alloy AA 5083*, J. Alloys Compd. 689 (2016), pp. 998–1010.

[10] O. Engler, Z. Liu and K. Kuhnke, *Impact of homogenization on particles in the Al-Mg-Mn alloy AA 5454-Experiment and simulation*, J. Alloys Compd. 560 (2013), pp. 111–122.

[11] E.M. Taleff, G.A. Henshall, T.G. Nieh and D.R. Lesuer, *Warm-temperature tensile ductility in Al−Mg alloys.pdf*, Metall. Mater. Trans. A 29 (1998), pp. 1081–1091.

[12] H.J. McQueen and O.C. Celliers, *Review application of hot workability studies to extrusion processing : part II. microstructural development and extrusion of Al , Al-Mg , and Al-Mg-Mn alloys*, Can. Metall. Q. 35 (1996), pp. 305–319.

[13] H. Zhang, E. V. Konopleva and H.J. McQueen, *Effects of Mn dispersoid on hot working Al-1Mn*, Mater. Sci. Eng. A 319 (2001), pp. 711–715.

[14] K. Liu and X.G. Chen, *Evolution of Intermetallics, Dispersoids, and Elevated Temperature Properties at Various Fe Contents in Al-Mn-Mg 3004 Alloys*, Metall. Mater. Trans. B Process Metall. Mater. Process. Sci. 47 (2016), pp. 3291–3300.

[15] X. Qian, N. Parson and X.G. Chen, *Effects of Mn addition and related Mn-containing dispersoids on the hot deformation behavior of 6082 aluminum alloys*, Mater. Sci. Eng. A 764 (2019), pp. DOI:10.1016/j.msea.2019.138253.

[16] M. Shakiba, N. Parson and X.G. Chen, *Hot deformation behavior and rate-controlling mechanism in dilute Al-Fe-Si alloys with minor additions of Mn and Cu*, Mater. Sci. Eng. A 636 (2015), pp. 572–581.

[17] M. Mofarrehi, M. Javidani and X. Chen, *Effect of Mn content on the hot deformation behavior and microstructure evolution of Al – Mg – Mn 5xxx alloys*, Mater. Sci. Eng. A 845 (2022), pp. https://doi.org/10.1016/j.msea.2022.143217.

[18] M.G. Cockroft and D.J. Latham, *Ductility and the Workability of Metals*, ournal Inst. Met. 96 (1968), pp. 33–39.

[19] M. Oyane, *Criteria of ductile fracture strain*, Bull. JSME 15 (1972), pp. 1507–1513.

[20] N. Brännberg and J. Mackerle, *Finite element methods and material processing technology*, Eng. Comput. 11 (1994), pp. 413–455.

[21] A. Rudra, M. Ashiq, J.K. Tiwari, S. Das and R. Dasgupta, *Study of Processing Map and Effect of Hot Rolling on Mechanical Properties of Aluminum 5083 Alloy*, Trans. Indian Inst. Met. 73 (2020), pp. 1809–1826.

[22] Y.V.R.K. Prasad, *Processing maps: A status report*, J. Mater. Eng. Perform. 22 (2013), pp. 2867–2874.

[23] K.P. Rao, Y.V.R.K. Prasad and K. Sivaram, *Deformation processing map for control of microstructure in Al4Mg alloy*, Mater. Lett. 10 (1990), pp. 66–70.

[24] H.T. Jeong, S.H. Han and W.J. Kim, *Effects of large amounts of Mg (5–13 wt%) on hot compressive deformation behavior and processing maps of Al-Mg alloys*, J. Alloys Compd. 788 (2019), pp. 1282–1299.

[25] B. Ke, L. Ye, J. Tang, Y. Zhang, S. Liu, H. Lin et al., *Hot deformation behavior and 3D processing maps of AA7020 aluminum alloy*, J. Alloys Compd. 845 (2020), pp. DOI:10.1016/j.jallcom.2020.156113.

[26] C. Shi and X.G. Chen, *Hot Workability and Processing Maps of 7150 Aluminum Alloys with Zr and V Additions*, J. Mater. Eng. Perform. 24 (2015), pp. 2126–2139.

[27] M. Mofarrehi, M. Javidani and X.G. Chen, *On the intermetallic constituents in the sodium-induced edge cracking of hot-rolled AA5182 aluminum alloys*, Philos. Mag. 101 (2021), pp. 1849–1870.

[28] F.J. Humphreys, *Grain and subgrain characterisation by electron backscatter diffraction*, J. Mater. Sci. 36 (2001), pp. 3833–3854.

[29] O. Engler, K. Kuhnke and J. Hasenclever, *Development of intermetallic particles during solidification and homogenization of two AA 5xxx series Al-Mg alloys with different Mg contents*, J. Alloys Compd. 728 (2017), pp. 669–681.

[30] Y.J. Li and L. Arnberg, *Solidification structures and phase selection of iron-bearing eutectic particles in a DC-cast AA5182 alloy*, Acta Mater. 52 (2004), pp. 2673–2681.

[31] H.J. McQueen, S. Spigarelli, M.E. Kassner and E. Evangelista, *Hot Deformation and Processing of Aluminum Alloys*, CRC Press, 2011.

[32] Y.V.R.K. Prasad, H.L. Gegel, S.M. Doraivelu, J.C. Malas, J.T. Morgan, K.A. Lark et al., *Modeling of dynamic material behavior in hot deformation: Forging of Ti-6242*, Metall. Trans. A 15 (1984), pp. 1883–1892.

[33] Q. Luan, J. Wang, Y. Huang, D.S. Balint and J. Jiang, *How would the deformation bands affect recrystallization in pure aluminium?*, Mater. Des. 209 (2021), pp. DOI:10.1016/j.matdes.2021.109960.

[34] N. Yan, Z. Li, Y. Xu and M.A. Meyers, *Shear localization in metallic materials at*

high strain rates, Prog. Mater. Sci. 119 (2021), pp. DOI:10.1016/j.pmatsci.2020.100755.

[35] Y. Xu, J. Zhang, Y. Bai and M.A. Meyers, *Shear localization in dynamic deformation: Microstructural evolution*, Metall. Mater. Trans. A Phys. Metall. Mater. Sci. 39 A (2008), pp. 811–843.

[36] Y.B. Xu, W.L. Zhong, Y.J. Chen, L.T. Shen, Q. Liu, Y.L. Bai et al., *Shear localization and recrystallization in dynamic deformation of 8090 Al-Li alloy*, Mater. Sci. Eng. A 299 (2001), pp. 287–295.

[37] A.T. Stewart and J.W. Martin, *Dislocation-particle interactions in plastically deformed two-phase aluminium crystals*, Acta Metall. 23 (1975), pp. 1–7.

[38] X. Ma, D. Zhao, S. Yadav, D. Sagapuram and K.Y. Xie, *Grain-subdivision-dominated microstructure evolution in shear bands at high rates*, Mater. Res. Lett. 8 (2020), pp. 328–334.

[39] F.J. Humphreys and M. Hatherly, *Recrystallization and Related Annealing Phenomena*, SecondElsevier Ltd, 2004.

[40] A. Heidarzadeh, S. Mironov, R. Kaibyshev, G. Çam, A. Simar, A. Gerlich et al., *Friction stir welding/processing of metals and alloys: A comprehensive review on microstructural evolution*, Prog. Mater. Sci. 117 (2020), pp. DOI:10.1016/j.pmatsci.2020.100752.

[41] Y.V.R.K. Prasad and S. Sasidhara, *Introduction*, in *Hot Working Guide A Compendium of Processing Maps*, ASM international, 2013, pp. 1–30.

[42] N. Nayan, S.V.S.N. Murty, S. Chhangani, A. Prakash, M.J.N.V. Prasad and I. Samajdar, *Effect of temperature and strain rate on hot deformation behavior and microstructure of Al-Cu-Li alloy*, J. Alloys Compd. 723 (2017), pp. 548–558.

[43] O. Sitdikov, E. Avtokratova, T. Sakai and K. Tsuzaki, *Ultrafine-grain structure formation in an Al-Mg-Sc alloy during warm ECAP*, Metall. Mater. Trans. A Phys. Metall. Mater. Sci. 44 (2013), pp. 1087–1100.

[44] A. Chaudhuri, A.N. Behera, A. Sarkar, R. Kapoor, R.K. Ray and S. Suwas, *Hot deformation behaviour of Mo-TZM and understanding the restoration processes involved*, Acta Mater. 164 (2019), pp. 153–164.

Chapter 6: On the Intermetallic Constituents in the Sodium-Induced Edge Cracking of Hot-Rolled AA5182 Aluminum Alloys

Mohammadreza Mofarrehi, Mousa Javidani, X.-Grant Chen
Department of Applied Science, University of Québec at Chicoutimi, Saguenay, Québec, G7H 2B1, Canada

This manuscript was published in:
Philosophical Magazine

Abstract

The productivity and recovery of hot-rolled Al-Mg-Mn sheets often suffer from sodium-induced edge cracking. In this study, AA5182 ingots with different levels of Na were prepared by direct-chill (DC) casting and were then subsequently subjected to homogenisation and hot-rolling processes. The edge crack occurrence during hot rolling in the pass #11 (84% reduction) and pass #18 (96% reduction) was investigated, with special attention paid to the impact of intermetallic constituents in the ingot subsurface region, where all edge cracks were initiated. Correlations between the susceptibility to edge cracking, enriched intermetallic constituents in the inverse segregation zone, Mg_2Si cavitation, meniscus bands, and Na contamination were observed. The results revealed that Fe-rich intermetallic particles were not involved in crack formation, while Mg_2Si particles had a strong tendency to debond from the Al matrix and form cavities at the edges of the rolled strip. The higher the Na content, the more severe the Mg_2Si cavitation, and consequently, the higher the susceptibility to edge cracking. Numerous debonded Mg_2Si particles contaminated with Na in the subsurface region provided favourable conditions for crack initiation and propagation. The role of the meniscus bands on the large and profound edge cracks was also elaborated.

6.1 Introduction

Owing to their high strength-to-weight ratio, excellent corrosion resistance, good formability and weldability, Al-Mg sheets are increasingly used to manufacture lightweight parts of the car body and chassis in the automotive industry [1−3]. However, the productivity, recovery, and quality of Al-Mg sheet pro- ducts often suffer from edge cracking during hot rolling [4−6]. In commercial Al-Mg alloys, Na is a common undesirable impurity; even a trace amount of Na can jeopardize productivity by contributing to severe edge cracking. However, the presence of Na in the order of ppm is inevitable in the casting process.

Commercial Al-Mg sheet products are usually fabricated through DC casting, homogenization, hot rolling, and cold rolling. Since all edge cracks initiate at the surface of DC-cast ingots, the microstructural aspects in the subsurface region of DC ingots and their relationship with the impact of Na are of great technical interest.

In DC-cast ingot products, an enriched layer composed of a large amount of solutes and intermetallic constituents is formed in the subsurface region by inverse segregation [7,8]. Through the inverse segregation and volume contraction, the solute-rich liquid moves in the opposite direction of the solidification front by penetrating into the network of solidifying dendrites in the mushy zone [8]. Owing to the fluctuation of the melt pressure, the movement of the liquid level, and the surface tension of the liquid, meniscus bands also form on the ingot surface at regular intervals, through which the inverse segregation is further extended toward the bulk [9,10]. Prior to hot rolling, the ingot is homogenized, and the surface zone is scalped off from the rolling faces of the ingot. However, the homogenization process cannot completely remove the effect of inverse segregation and the meniscus bands, as some intermetallics are insoluble or only partially soluble. Furthermore, in industrial practices, the short sides of Al DC-cast ingots are usually not scalped prior to rolling. Consequently, the enriched layer of intermetallics in the subsurface region could potentially be favorable sites for edge cracking.

The detrimental influence of Na on the embrittlement and edge cracking of Al-Mg alloys has been long recognized and investigated. Ransley and Talbot [11] first investigated the embrittlement of Al−Mg−Si alloys and reported that hot ductility was strongly impaired at high Na levels. Several researchers reported that the high-temperature embrittlement of Al-Mg alloys was caused by the segregation of trace Na to grain boundaries; hence, grain boundary weakening was considered as the root cause of edge cracks [12−16]. Horikawa et al. [16] examined the effect of Na on high-temperature embrittlement by measuring the reduction of area during tensile testing of Al−5Mg alloys containing different levels of Na, in the range of 0.01-2 ppm. Trace Na was detected by glow discharge mass spectrometry and was assumed to segregate to the grain boundaries in the form of free Na atoms. However, Lynch [17] believed that the hypothesis of grain boundary segregation was doubtful and suggested that the high-temperature embrittlement might be due to the formation of low melting point Na-rich phases or particles after comparison with other Al alloys. Simensen and Sodervall [18] investigated the trace elements in Al-4.8Mg-0.3Mn DC- cast ingots and found that the impurities (e.g. Na, Ca, etc.) were segregated and enriched in the cast surface layer of DC ingots, forming a number of Na particles on the surfaces of intermetallic particles. Through a thermodynamic simulation, Zhang et al. [19] reported that Na in Al-Mg system could form a so-called liquid-2 phase at fairly low-Na concentrations, which had a very low melting point. During hot rolling, it transformed into a liquid and caused low ductility at the grain boundaries or at other phase boundaries. It was concluded that the higher the Na content in the alloy, the greater the volume of this liquid phase, and consequently the higher the embrittlement. Hosokawa et al. [20] studied the development of cavitation on the periphery of Mg_2Si particles during large-scale tensile deformation in an Al-4.5Mg alloy and found that the volume fraction of Mg_2Si cavities significantly increased with increasing strain, and that Mg_2Si particles were not beneficial for hot workability by promoting cavitation at high temperatures.

Despite numerous investigations, the mechanisms of Na on embrittlement and edge cracking in Al−Mg alloys have not been fully understood. In the present work, great efforts have been made to characterize the microstructure in the subsurface region of DC-cast ingots, where the enriched intermetallic constituents were segregated and induced crack

initiation. Furthermore, the interaction of the intermetallics with Na, as well as the combined effect of microconstituents and hot-rolling process on edge cracking susceptibility, were studied.

6.2 Experimental procedure

AA5182 alloys with two different levels of Na were prepared by DC casting for pilot-scale casting and hot rolling trials; one alloy had an Na content of less than 0.5 ppm, and the other consisted of more than 1 ppm Na. The former is denoted hereafter as LS (which stands for low Na), and the latter as HS (standing for high Na). Rectangular DC-cast ingots with dimensions of 600 × 229 × 75 mm were provided by the Arvida Research and Development Centre of Rio Tinto Aluminum, Saguenay, QC, Canada. The chemical compositions analyzed by optical emission spectroscopy are shown in Table 6-1.

Rectangular blocks for the hot-rolling process, with the dimensions presented in Fig. 6-1, were prepared from the cast ingot. The rolling faces of the blocks were machined (10 mm from each side) to remove the as-cast surface. To investigate the effect of subsurface microstructure on edge cracking, one of the short faces of each ingot was also scalped off by approximately 25 mm, while the cast surface of the other short face remained intact. The pre- pared blocks were subsequently homogenized using the procedure depicted in Fig. 6-2. One test block of each alloy was water quenched right after the homogenization treatment to study the microstructure evolution. The remaining heat-treated blocks were directly subjected to 18 consecutive passes of hot rolling. The hot rolling was carried out on a two-high rolling mill with ~310 mm roll diameter in the 400–500 °C temperature range.

Table 6-1: Chemical compositions of the DC cast AA5182 alloys (wt.%).

Alloy ID	Si	Fe	Cu	Mn	Mg	Ti	Na (ppm)
HS	0.05	0.14	≤0.05	0.25	4.8	0.023	1.1
LS	0.06	0.15	≤0.05	0.25	4.8	0.023	0.3

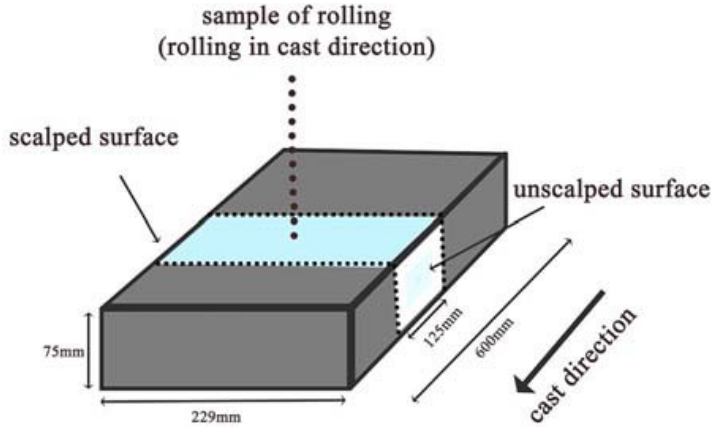

Fig. 6-1: Schematic of the prepared block for the hot rolling from DC-cast ingots.

During hot rolling, the rolled strip temperature was constantly monitored to maintain over 400 °C. When the strip temperature fell below 400 °C, the strip was put back in the furnace to re-heat to 500 °C in-between the rolling passes. Through the rolling process, the thickness of the blocks was reduced from 75 to 3 mm with an area reduction of 96%. Samplings for further microstructural characterization were carried out after the 11th and 18th passes as well; pass #11 (plate thickness of 12 mm, 86% area reduction) was the initiation point of edge cracking detected by the naked eye and pass #18 was the last step of the rolling process. The rolled samples of the alloy containing high sodium from the 11th and 18th passes are denoted as HS11 and HS18, respectively, while the samples of the alloy with low sodium are referred to as LS11 and LS18, respectively. Samples which were scalped from the short surface of the ingot have a 'S' appended to the end of their label (e.g. HS11S). The sample identification for the different conditions is listed in Table 6-2.

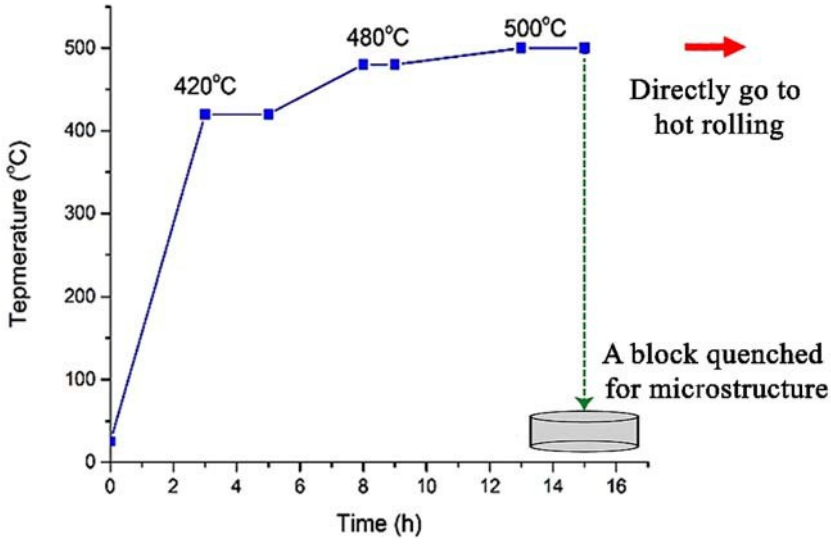

Fig. 6-2: Homogenisation procedure applied to the DC-cast ingots.

Table 6-2: Sample ID of rolling plates under different conditions.

Alloys	#11 pass - unscalped surface	#11 pass - scalped short surface	#18 pass - unscalped surface	#18 pass - scalped short surface
HS (High Na)	HS11	HS11S	HS18	HS18S
LS (Low Na)	LS11	LS11S	LS18	LS18S

For the microstructure observation, an optical microscope, and a scanning electron microscope (SEM, JEOL JSM-6480LV) equipped with energy dispersive spectroscopy (EDS) were used. The samples were mounted and mechanically ground using SiC papers. The polishing was subsequently carried out using alcohol-based colloidal silica suspensions to avoid any possible dissolution of Mg_2Si phase during water-based polishing. The quantitative analysis of the microstructural features was performed by the image analysis software (Clemex PE4.0). To better characterise the intermetallic particles and facilitate phase identification, the metallographic samples were etched using 0.5% HF for 10 s. However, SEM-EDS analyses were per- formed prior to etching.

6.3 Results

6.3.1 Microstructures under as-cast and as-homogenized conditions

The edge cracks during rolling were all initiated from the subsurface region of the DC-cast ingot, and then propagated toward the ingot bulk in different extensions. Therefore, the microstructure analyses were focussed on two dis- tinct regions: the subsurface region that covers the ingot cast surface to several millimeters' inwards, and the bulk region. Representative micrographs from the subsurface region are shown in Fig. 6-3. The cast surface from the short side of the DC-cast ingot is shown in Fig. 6-3a. From the cast surface, the first visible zone was the inverse segregation zone, which contains enriched intermetallic particles and solute elements, as shown in Fig. 6-3b. The inverse segregation zone had a thickness that ranged from 85 to 250 μm and could occasionally extend to approximately 400 μm. In the subsurface region, there were meniscus bands (Fig. 6-3a and c), which were more noticeable at the corners of the ingot and presented a repetitive pattern along the casting direction with an interval of approximately $5.5 \pm 1.5 \times 10^3$ μm. These meniscus bands brought the inverse segregation zone (enriched intermetallic particles) toward the bulk with a depth of up to approximately 800-1000 μm.

The typical as-cast microstructures of the subsurface and bulk region, dis- played in Fig. 6-4, were composed of Mg_2Si, β-Al_8Mg_5, and Fe-rich intermetallics. Mg_2Si intermetallic particles with Chinese script morphology (Fig. 6-4, #1) and Fe-rich intermetallics were mostly located in the interdendrite regions. The Mg-rich β-Al_8Mg_5 particles (Fig. 6-4, #3) with a bulky morphology were the last eutectic intermetallic solidified in the interdendrite regions, where adequate Mg atoms were available [21,22]. The Fe-rich intermetallics appeared in three distinct types: Al_6(Mn,Fe), Al_3(Mn,Fe), and metastable Al_m(Mn,Fe); these intermetallics were characterized by SEM-EDS analysis, and were consistent with the results reported in the literature [23–26]. Al_6(Mn,Fe) particles had a plate-like morphology (Fig. 6-4, #4), while Al3(Mn,Fe) particles were distinguished by a needle-like morphology (Fig. 6-4, #2). The metastable Al_m(Mn, Fe) particles also presented a plate-like shape and appeared only in the subsurface region (Fig. 6-4, #5). The type and morphology of the intermetallic constituents were similar between the inverse segregation zone (Fig.

6-4a) and the bulk material (Fig. 6-4b). However, the quantity of intermetallic constituents in the inverse segregation zone was much higher than that in the bulk. The results of the quantitative image analysis indicated that the volume fraction of Mg_2Si was five times higher in the inverse segregation zone relative to the bulk, while the volume fractions of Fe-rich intermetallics and β-Al_8Mg_5 particles were two and eight times higher, respectively (Table 6-3). It is worth mentioning that the trace amount of Na did not affect the type and morphology of the intermetallic phases, and therefore, the results in Fig. 6-3 and Fig. 6-4 and Table 6-3 are valid for both high Na and low Na (HS and LS) alloys. The EDS spectra of the phases were presented in Fig. 6-5.

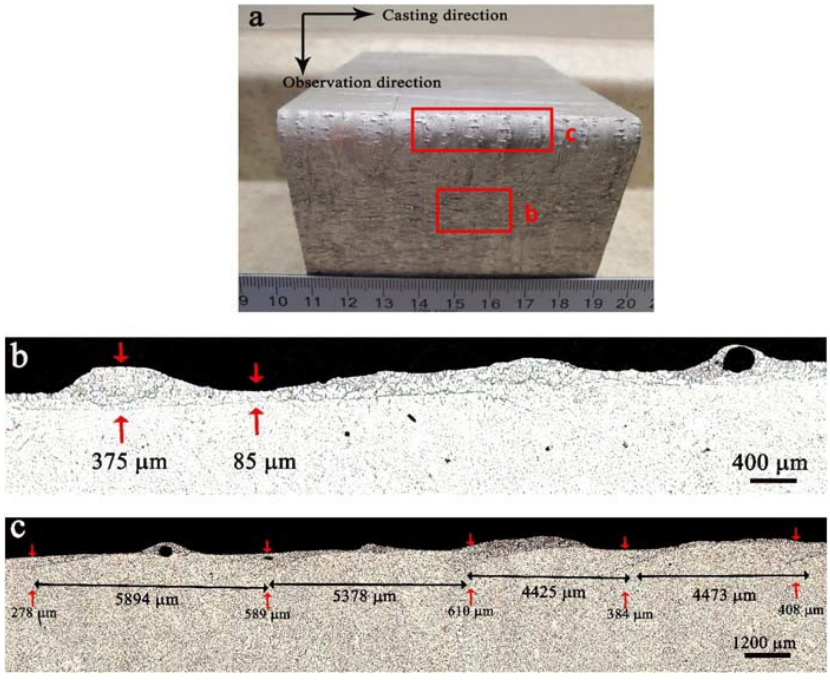

Fig. 6-3: The cast surface and the microstructure in the subsurface region: a) cast surface of the short side of the ingot, b) the inverse segregation zone and c) the meniscus bands.

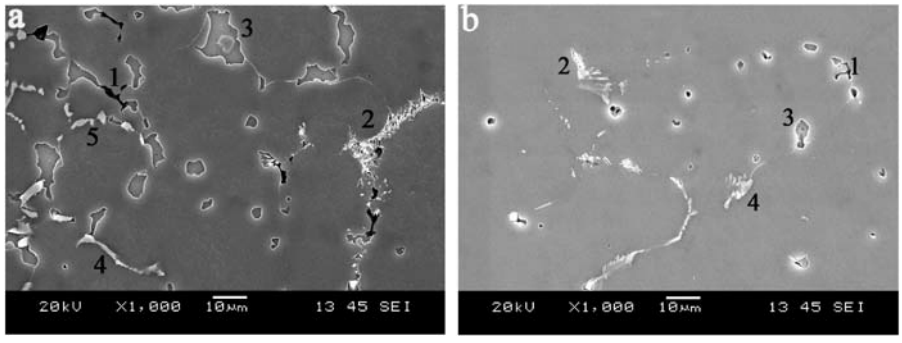

Fig. 6-4: SEM images of the as-cast microstructure at a) the inverse segregation zone and b) bulk: (1) Mg_2Si, (2) $Al_3(Mn,Fe)$, (3) β-Al_8Mg_5, (4) $Al_6(Mn,Fe)$, (5)$Al_m(Mn,Fe)$.

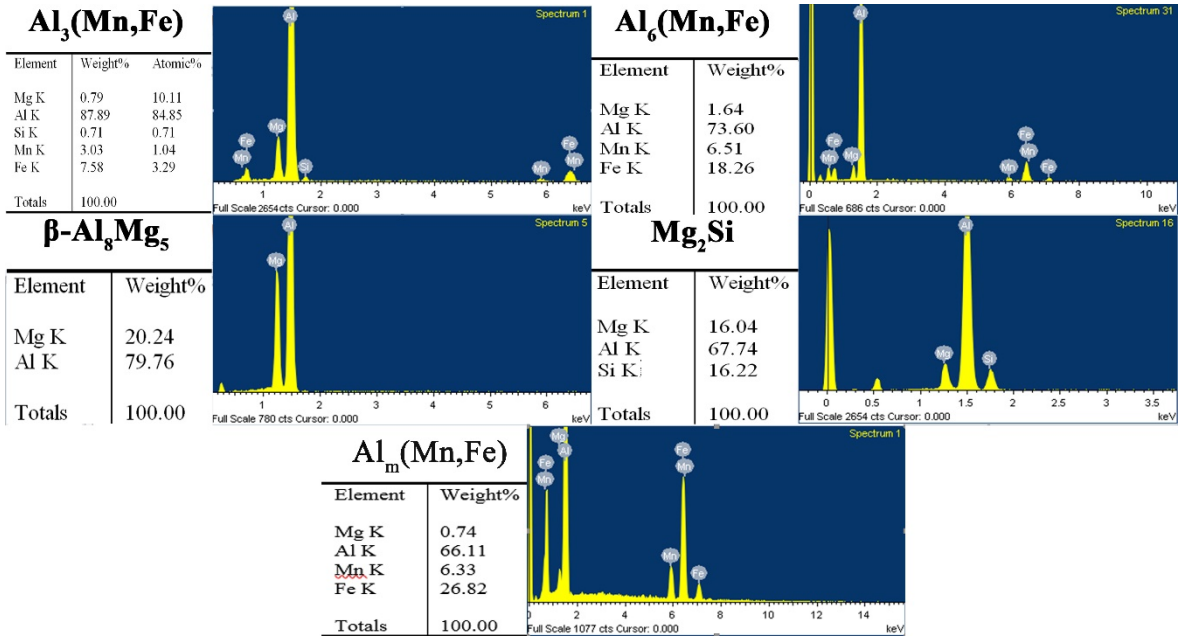

Fig. 6-5: SEM-EDS spectra of the intermetallics.

Fig. 6-6 shows SEM micrographs of the as-homogenized microstructure in the subsurface and bulk region. After homogenization, the β-Al_8Mg_5 intermetallics were entirely dissolved in both the subsurface and bulk region, which was in good agreement with the results reported in the literature [21]. As the β- Al_8Mg_5 eutectic phase solidified at a temperature close to 451°C, the present homogenization practice was adequate to completely dissolve these intermetallic particles. On the other hand, Mg_2Si particles were partially dissolved (close to 50%). It was reported [27] that the Mg_2Si phase changes during homogenization with the following sequences: 1) decomposition into small fragments, 2) diffusion-controlled spheroidization and 3) coarsening. Microstructural results revealed that Mg_2Si particles in this study experienced only the first two steps (the decomposition and spheroidization) without any noticeable coarsening. A limited dissolution of Mg_2Si for the alloys containing 2 wt.% Mg or higher has also been reported by Radetic et al. [28]. The Fe-rich intermetallic particles experienced only partial spheroidization, but their dissolution was negligible. It was observed that the metastable $Al_m(Mn,Fe)$ had transformed into $Al_3(Fe, Mn)$ during homogenization. This solid-state eutectoid phase transformation was discussed in detail by Li and Arnberg [23]. Therefore, there were

two types of Fe-rich intermetallics that remained in the as-homogenized micro- structure: plate-like $Al_6(Mn,Fe)$ and needle-like $Al_3(Mn,Fe)$ (Fig. 6-6). The quantitative results of the volume fraction of all intermetallics in the subsurface and bulk regions after homogenization are shown in Table 6-3. Although the total amount of Mg_2Si was considerably reduced during homogenization, the volume fraction of Mg_2Si was still five times higher in the inverse segregation zone than in the bulk. The amount of Fe-rich intermetallics in these samples was slightly decreased compared to the quantity in the as-cast samples, but the measured volume fraction was still two times higher in the inverse segregation zone relative to the bulk region.

Due to the large difference in the quantity of intermetallics (Mg_2Si and Fe- rich intermetallics) between the subsurface and bulk regions, the inverse segregation zone and meniscus bands were still clearly visible after homogenization. Another characteristic observed in the subsurface area of Al-Mg 5182 alloy was severe oxidization during homogenization. As shown in Fig. 6-7, the porous oxidized areas penetrated the cast surface inward, extending up to a few hundred micrometers into the material. The SEM-EDS results confirmed that the porous oxidized areas contained mostly AlMgO particles. Together with porosities and inclusions that were often encountered in the subsurface area (Fig. 6-3b), these defects provided favorable sites for the initiation of edge cracks during hot rolling.

Table 6-3: Comparison of the volume fraction of intermetallic constituents in the inverse segregation zone and bulk area (vol.%).

	As-cast			After homogenization		
	Mg_2Si	Fe-rich particles	β-Al_8Mg_5	Mg_2Si	Fe-rich particles	β-Al_8Mg_5
Inverse segregation zone	1.0	2.1	9.4	0.54	2.0	0
Bulk area	0.2	1.2	1.2	0.1	1	0

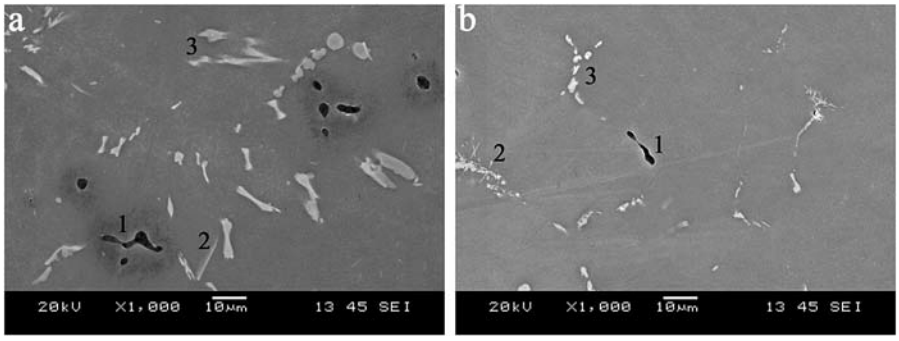

Fig. 6-6: SEM images of the as-homogenized microstructure at a) the inverse segregation zone and b) bulk: (1) Mg_2Si, (2) $Al_3(Mn,Fe)$ and (3) $Al_6(Mn,Fe)$.

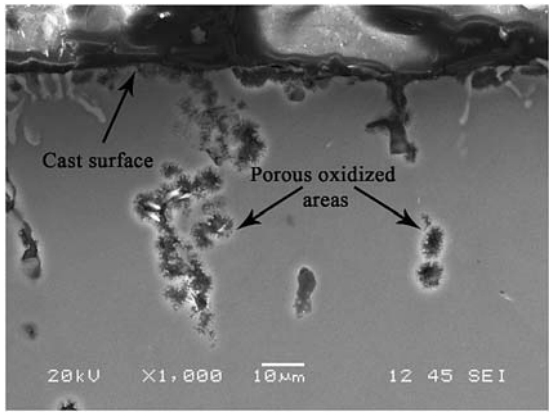

Fig. 6-7: Porous oxidized areas in the subsurface area of the ingot after homogenization.

6.3.2 Edge cracking evolution during hot rolling

In the present work, the cracks in the ingot edges during hot rolling became visible by the naked eye after pass #11, with pass #18 being the final pass during hot rolling. Therefore, the results of the rolled samples after pass #11 (with 84% area reduction) and pass #18 (with 96% area reduction) are presented here.

Cracks after pass #11 (Fig. 6-8a) were observed only in the sample with high Na content (HS11, Fig. 6-8a), and no visible cracks could be found in the sample with low Na content (LS11, Fig. 6-8b). By continuing the hot deformation (rolling to pass #18), the detrimental impact of Na on edge cracking susceptibility was more exposed. The macroscopic edge cracks encountered in the present work can be divided into two categories: 1) small cracks that remained superficially on the edge of the rolled strip with a maximum penetration depth of 3 mm, and 2) large cracks that were profoundly propagated into the bulk of the material. As the edges of the rolled strip are always trimmed out during

the industrial rolling process, the small cracks are less harmful in terms of the rolling recovery, while the large cracks are particularly detrimental for the rolling process recovery and productivity. In the high Na sample (HS18), although the majority of the cracks were small cracks, a number of large cracks were observed on the edges and propagated up to 12-15 mm inwards (Fig. 6-8c and d).

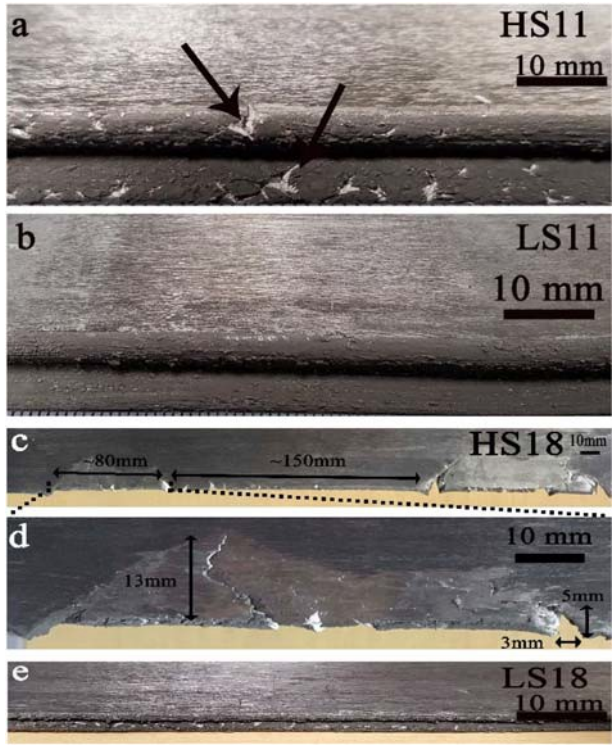

Fig. 6-8: The edges of high and low sodium rolled samples after passes #11 and #18 of hot rolling: a) HS11, b) LS11, c and d) HS18, e) LS18. The rolling direction is horizontal.

Furthermore, there were some triangular torn-off areas at the edges, where the cracks propagated up to 7 mm inward (Fig. 6-8c and d). These triangular cracks indicated the possibility of tearing off small pieces from the rolled block, which may fall out in the successive rolling passes. By moving away from the surface toward the bulk, the cracks tended to align toward the rolling direction. Another important feature of the large cracks was their repetitive pattern along the casting/rolling direction at intervals of 150 ± 20 mm, as shown in Fig. 6-8c. Unlike the sample HS18, in the low Na LS18 sample,

no profound cracks were observed. As shown in Fig. 6-8e, the cracks in LS18 were all superficial with a depth of 1-3 mm, even after pass #18 with 96% reduction.

The quantity versus depth of cracks in high Na samples, measured over a 30 cm length in several samples in the rolling direction, is presented in Fig. 6-9. As the statistical results of Fig. 6-9 show, almost all cracks in the HS11 sample were small, with a maximum propagation depth of 3 mm. In the HS18 sample, a majority of the cracks (more than 80% in term of the crack number) were still small and superficial, but the rest were large and profound, with a depth of greater than 3 mm. In industrial practice, these large cracks could not only scrap the entire rolling product, but also jeopardise the rolling production line.

On the other hand, the edge cracks were mostly eliminated in the surface- scalped samples, where the side was scalped off 25 mm from the short side of the ingot. As illustrated in Fig. 6-10, almost no edge cracks could be found after pass #11 in both the low Na and high Na samples (Fig. 6-10a of LS11S and Fig. 6-10b of LS18S). After pass #18, no edge cracks were detectable in the low Na sample (LS18S, Fig. 6-10c), while a few small and superficial cracks with a depth of 1-2 mm were seen in the high Na sample (HS18S, Fig. 6-10d). It is important to highlight that the number of cracks in HS18S (Fig. 6-10) was significantly lower even than that in the unscalped LS18 (Fig. 6-8e) and HS11 samples (Fig. 6-8a).

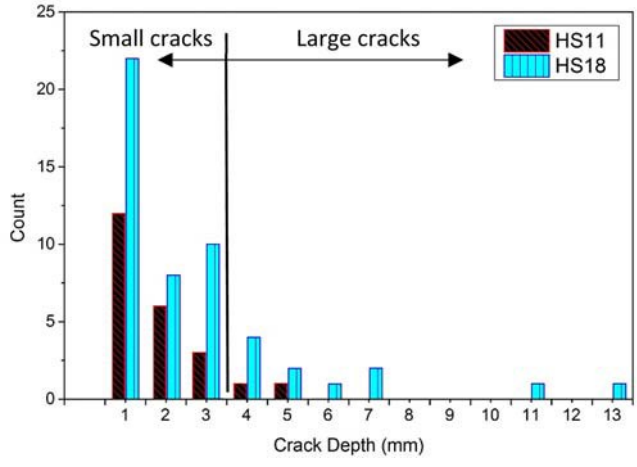

Fig. 6-9: Statistical data of the number and depth of edge cracks in HS11 and HS18 samples, measured over 30 cm length of rolled samples.

The cracking behaviour in the subsurface area was further investigated by SEM, and the results for different samples are compared in Fig. 6-11. The macrocracks on the edges were generally composed of numerous microcracks, and their length and width varied significantly. Although the edge cracks in the LS11 sample were not visible on the macroscale (Fig. 6-8b), some microcracks were still detectable, with lengths and widths of less than 50 and 5 μm, respectively (Fig. 6-11a). By applying further deformation (after pass #18), the micro- cracks in the LS18 sample were enlarged and had a maximum length of 100 μm and a width of up to 15 μm (Fig. 6-11b). These cracks were mostly limited to within 1-2 mm of the sample edge area. In the high Na HS11 sample (Fig. 6-11c), the cracks were remarkably larger and several times wider than those in the LS11 sample. The high Na HS18 sample showed the most severe cracking (Fig. 6-11d). The cracks were mostly connected to the sample surface, elongated longitudinally up to several millimeters, and branched into numerous smaller cracks along the primary crack path. The cracks/cavities were mostly inclined toward the rolling direction as they traveled from the surface toward the bulk.

Microcracks could also be found in the surface-scalped samples after passes #11 and #18 (Fig. 6-12). In the low Na sample (LS18S), a few microcracks were detectable in edge area of the sample. These small microcracks did not propagate and further develop into macro edge cracks, and they were also all restricted inside the ingot subsurface region without the connection to the ingot surface (Fig. 6-10Fb). In the high Na sample (HS18S), the number of micro- cracks increased considerably relative to the low Na sample (LS18S). Some of them were propagated and transformed to macroscopically visible edge cracks and were also connected to the sample surface (Fig. 6-10d). Nevertheless, it was evident that the number, length, and width of the micro- and macro- cracks in the scalped samples (Fig. 6-10 and Fig. 6-12) were very restricted and were much smaller when compared to the unscalped HS11 and HS18 samples (Fig. 6-8, Fig. 6-9, and Fig. 6-11).

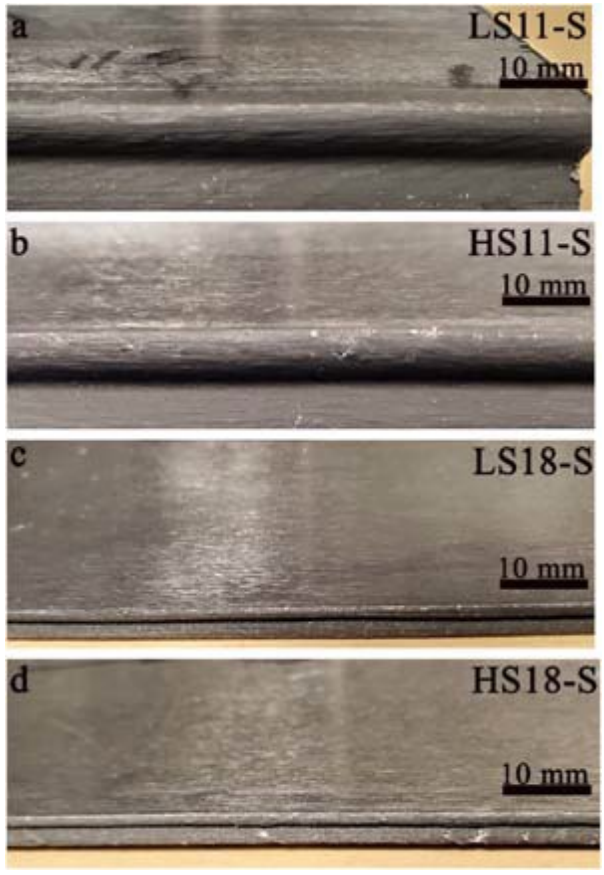

Fig. 6-10: The edges of the surface-scalped samples in both high and low sodium alloys after passes #11 and #18 of hot rolling: a) LS11S, b) HS11S, c) LS18 and d) HS18S.

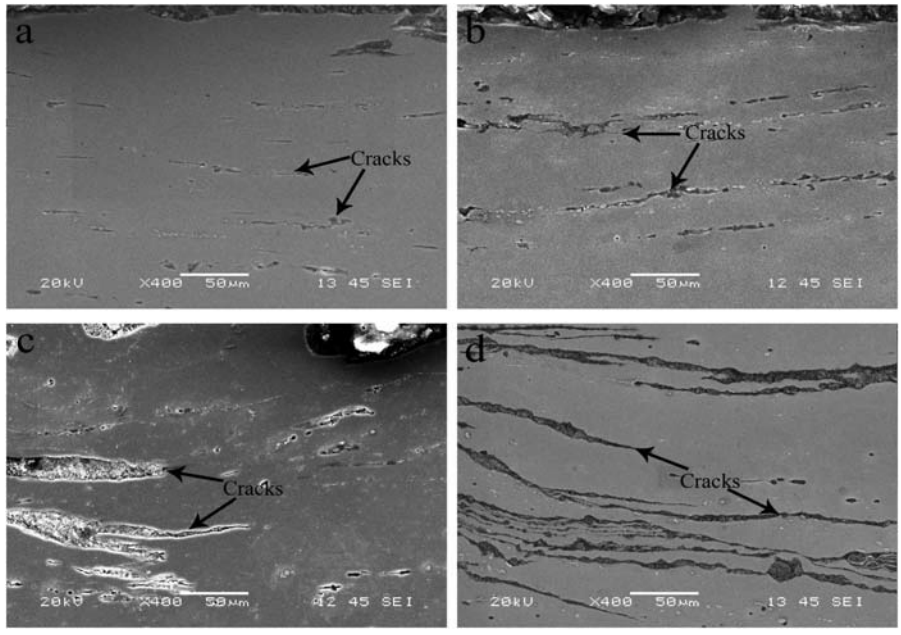

Fig. 6-11: SEM images of the microcracks of the rolled samples: a) LS11, b) LS18, c) HS11 and d) HS18. The top of each image is the edge of the rolled strip.

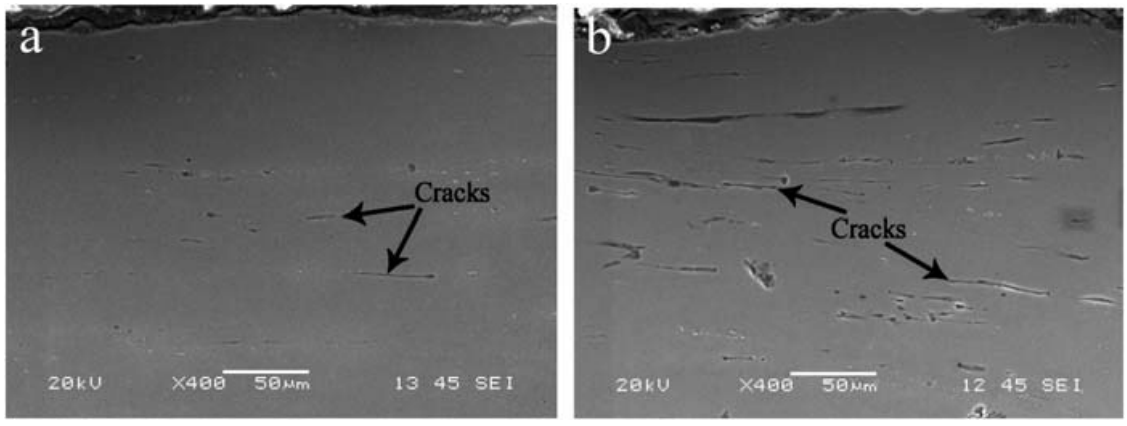

Fig. 6-12: SEM images of the microcracks in the surface-scalped samples: a) LS18S and b) HS18S. The top of each image is the edge of the rolled strip.

6.3.3 Impact of intermetallic constituents on edge cracks

As mentioned above, the β-Al_8Mg_5 intermetallics were entirely dissolved during the homogenization treatment, and Mg_2Si and Fe-rich intermetallic particles were the only intermetallic constituents remaining in the ingot micro- structure during the rolling process. The Mg_2Si and Fe-rich particles in the rolled microstructure could be easily distinguished by their color, as well as by EDS analysis in SEM. In the subsurface region, Mg_2Si particles were often detached from the aluminum matrix, forming cavities/voids on their periphery adjacent to the path of the microcracks. The micrographs in Fig. 6-13 illustrate the debonding and cavitation of Mg_2Si particles from the Al matrix in the samples containing high Na (i.e. HS11 and HS18). In contrast to the Mg_2Si particles, Fe-rich particles underwent fragmentation during rolling, but no evidence of Fe-rich particle detachment from the aluminum matrix could be found (Fig. 6-13). As shown in Fig. 6-13, a few Fe-rich particles were also found near the Mg_2Si particle and crack path, but no decohesion of Fe-rich particles from the aluminum matrix was observed for either type of Fe-rich particles. It is evident that Fe-rich intermetallic particles did not contribute to cavitation and void formation. It is worth mentioning that at least 100 particles and the surrounding matrix were analyzed by SEM to confirm the detachment and cohesion behavior of both Mg_2Si and Fe-rich intermetallic constituents, respectively.

Results of numerous particle analyses showed that the cavities were formed in the detached area of Mg_2Si particles and extended into the matrix along the rolling direction.

The phenomenon of the Mg_2Si particle-matrix decohesion and the subsequent cavitation is well depicted in Fig. 6-14. Fig. 6-14a illustrates an early stage of particle debonding, with an approximately 1 μm cavity formed on one side of the Mg_2Si particle. Fig. 6-14b presents the coalescence of several instances of Mg_2Si particle-matrix decohesion and subsequent growth to elongated cavities, leading to a path for crack propagation in the rolling direction. The particle decohesion and cavitation in the samples with high Na content (HS11 and HS18) were much more severe than in the low Na containing samples (LS11 and LS18). It is interesting to note that in both micro- graphs shown in Fig. 6-14, the Fe-rich intermetallic particles were well-bonded with the Al matrix.

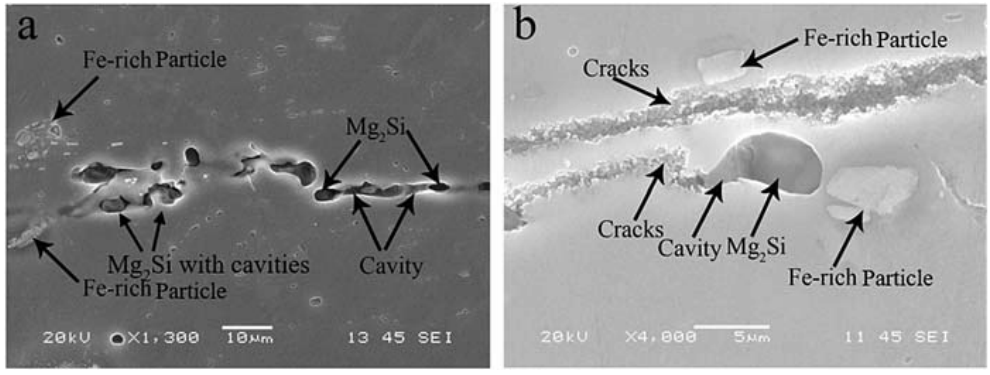

Fig. 6-13: SEM images of the Mg_2Si cavitation in the high Na samples: a) HS11 and b) HS18.

During SEM observation, it appeared that not all, but a considerable number, of Mg_2Si particles detached from the Al matrix and formed cavities. To better quantify the decohesion of Mg_2Si particles and their cavitation in the samples, the distribution of the non-debonded Mg_2Si and the debonded Mg_2Si with their adjacent cavities, as well as the area fraction of Mg_2Si plus the adjacent cavities, were measured. To do so, an area of approximately 50 mm in length and a 5 mm wide was carefully scanned in 1.25 mm intervals from the surface inwards by SEM for each sample. The results are presented in each 1.25 mm interval from the surface toward the bulk material, as shown in Fig. 6-15. In general, the number of debonded Mg_2Si particles in the first 1.25 mm interval was the highest, and it decreased from the surface inward (Fig. 6-15a). Both the number density of the debonded Mg_2Si particles and the ratio of the debonded to non-debonded particles in the first 1.25 mm interval for the HS18 sample containing high Na are very high at 325

particles per mm^2 and a ratio of 2.3, respectively. In contrast, the number density of the debonded Mg_2Si particles and the ratio of the debonded and non-debonded particles for the LS18 sample containing low Na are quite low (80 particles per mm^2 with a ratio of 0.25). Furthermore, for the inside of the strip, the number densities of the debonded Mg_2Si particles of the HS18 sample are always considerably higher than those of the LS18 sample. As shown in Fig. 6-15b, the area fraction of debonded Mg_2Si and their associated cavities in the first 1.25 mm interval for the samples containing high Na was about three times higher than the samples with low Na content (0.75% of HS18 vs 0.25% of LS18, and 0.5% of HS11 vs 0.18% LS11). The area fraction of the Mg_2Si cavitation became progressively smaller toward the sample inside, but the area fractions of the high Na sample (HS18 and HS11) were always higher than those of the low Na samples (LS18 and LS11).

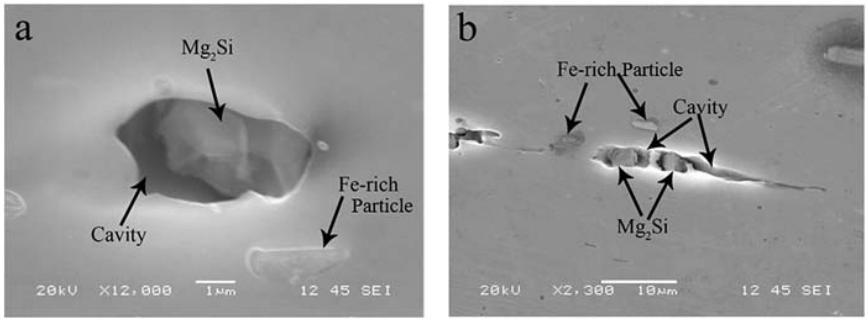

Fig. 6-14: Typical Mg_2Si particle-matrix decohesion and subsequent cavitation: a) an early stage of particle decohesion and b) the coalescence of cavities to form the microcrack. It is noted that the nearby Fe-rich particles were well-bonded with the matrix.

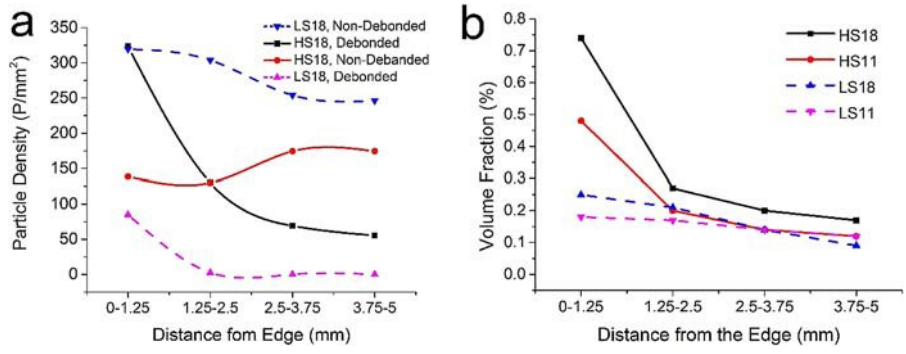

Fig. 6-15: Comparison of Mg_2Si particles and their cavities in the sample edge area for both rolled plates containing high and low Na, a) the distribution of the non-debonded Mg_2Si and the debonded Mg_2Si with cavity and b) the area fraction Mg_2Si particles and their cavities.

6.4 Discussion

During hot rolling, aluminum metal near the rolling surface of the cast ingot undergoes significantly greater deformation than the center part of the ingot. Furthermore, the essential plane-strain conditions prevail in the middle zone of the rolled ingot, while localized lateral flow occurs near the (two) edges [29]. This localized lateral flow usually results in a concave edge profile, through which the edge surface (i.e. the subsurface region of the cast ingot) is incorporated and extended into the rolling surface, as shown in Fig. 6-16. In successive rolling passes, the unsupported edges of the ingot strip experienced tensile stresses because of the greater elongation and bulging in the edges [5]. The applied tensile stress and the incorporation of edge surfaces into the rolling surface may create the necessary condition for crack initiation and propagation during subsequent rolling, as the material in the subsurface region had limited ductility, which may lead to macroscopic edge cracks.

The sensitivity to crack initiation and propagation at the edges of the strip is strongly dependent on the material ductility. The lower the material ductility, the more sensitive it is to the edge crack occurrence. Compared to the bulk of the material, the material ductility in the subsurface area of the cast ingot was strongly deteriorated by different defects, such as porosities and inclusions in the cast surface (Fig. 6-3), subsurface oxidation during homogenization (Fig. 6-7), and enriched intermetallic particles (Fig. 6-4). Consequently, sub- surface defects alongside the applied tensile stress during rolling provided favorable conditions for developing cracks. As the surface porosity, oxidation, and segregation zones were mainly driven by cast and homogenization processes rather than by alloy chemistry and impurities, subsurface crack initiation and propagation were observed in all of the LS18 and HS18 samples, regardless of Na content. Furthermore, by machining the subsurface region and removing the segregation zone and meniscus bands, the subsurface materials with limited ductility were scalped off of the ingot, and therefore, edge cracking was almost completely eliminated, occurring only near the end of the hot-rolling process (Fig. 6-10).

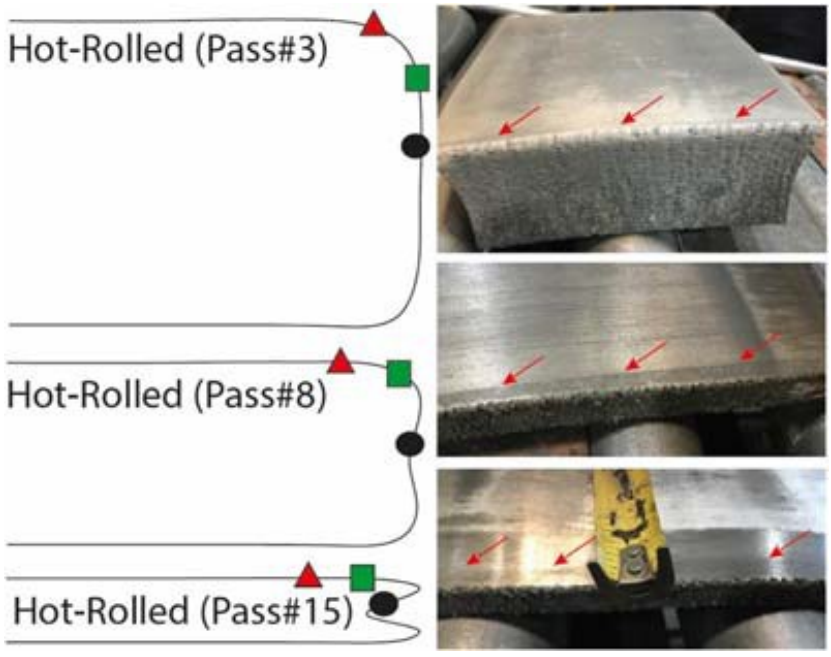

Fig. 6-16: Schematic of edge profile development during the reduction of hot-rolled ingot.

As mentioned above, after homogenization and prior to rolling, there were only two kinds of intermetallic constituents left in the Al matrix in both the subsurface and bulk regions: Mg_2Si and Fe-rich intermetallic particles, which were involved in plastic deformation during rolling. The subsurface region contained much more intermetallic particles than the bulk of the material (Table 6-3). During rolling, the Fe-rich intermetallic particles generally fragmented into small particles, but Fe-rich particles were well-bonded with the aluminum matrix, and neither decohesion from the matrix nor cavity formation were observed. It can be concluded that, although the Fe-rich intermetallic particles were twice as large in the subsurface region than in the bulk, they were not involved in the edge crack initiation and propagation. In contrast, Mg_2Si particles had a strong tendency to debond from the Al matrix and form a cavity in the Mg_2Si/Al interface under the applied tensile condition at the edges of the strip. The cavitation at the Mg_2Si particles could already be observed in pass #11, where macrocracks in HS11 and microcracks in LS11 occurred. With further deformation, the cavities grew and coalesced in both the HS18 and LS18 samples, resulting in a further loss of ductility on the edge surfaces. The development of cavitation on the periphery of the Mg_2Si particles during large-scale tensile deformation has long been observed in a similar Al-4.5Mg alloy [20], and it was found

that the volume fraction of Mg_2Si cavities significantly increased with increasing strain. The microstructure analysis in the present work clearly demonstrated that the proportion of the debonded Mg_2Si with cavities and the area fraction of cavities in the high Na alloy were much higher than in the low Na alloy (Fig. 6-15), which is consistent with the high susceptibility of edge cracking in the high Na alloy.

The inverse segregation zone in the ingot subsurface region was generally enriched with intermetallic particles and solute elements. Simensen and Sodervall [18] investigated the trace elements in Al-4.8Mg-0.3Mn DC-cast ingots by means of microprobe analysis and secondary ion mass spectrometry. They found that the impurities (Na, Ca, etc.) were enriched in the cast surface layer, and that a number of Na particles could be found on the surface of the intermetallic particles. Even in the homogenized and hot-rolled material, a small number of Na particles, which heterogeneously nucleated on the intermetallic particles, were detectable. Lynch [17] suggested that the high-temperature embrittlement of Al-Mg alloys could be due to the formation of low-melting- point Na-rich phases or particles. In further work by Zhang et al. [19] using thermodynamic simulation, it was found that a so-called Na-rich liquid-2 phase formed in Al-5Mg-Na system at relatively low Na concentrations, and that it exists in the 98−450 °C temperature range and incipiently melts at grain boundaries or other phase boundaries during hot rolling. It was concluded that the higher the Na content of the alloy, the greater the volume fraction of this low melting point phase. Regarding the Mg_2Si cavitation found in the present work, it is reasonable to assume that Na would segregate on the Mg_2Si boundaries and form a low-melting-point Na-rich thin layer or particle on the periphery of Mg_2Si particles, which underwent incipient melting during hot rolling, causing the decohesion of Mg_2Si from the matrix and subsequent cavitation. This phenomenon would be intensified in the inverse segregation zone of the alloy with high Na level, as the inverse segregation zone contained much more Mg_2Si particles (several times more than the bulk of the material in the present study alloy) and a high amount of segregated Na was also available. It is evident that numerous debonded Mg_2Si particles contaminated with Na in the ingot subsurface region provided favorable conditions for crack initiation and propagation, provoking the occurrence of macro-scale edge cracking.

This hypothesis can explain the occurrence of numerous superficial, small edge cracks – a majority of the cracks – that remained on the edges of the strip. It is still difficult to explain the development of large edge cracks that can extend several dozen millimeters from the edge into the bulk when taking into account the limited thickness of the inverse segregation zone (100-300 μm) and the significant reduction in the number of Mg_2Si particles with increasing distance from the edge (Fig. 6-15). However, the meniscus bands brought the inverse segregation zone with enriched Mg_2Si particles deeper toward the bulk (several times deeper than the segregation zone self), as shown in Fig. 6-3c. Utilizing the same cause and process as Mg_2Si cavitation, the debonded Mg_2Si particles contaminated with Na that existed along the penetrating meniscus bands provided favorable paths for large crack propagation. Fig. 6-17 shows an example where the Mg_2Si particles and the associated coalesced cavities can be found along the crack path and in the crack tip in a large and widely opened edge crack. The large and profound cracks, which were mainly seen in HS18 samples, presented a repetitive pattern with an interval of 150 ± 20 mm along the rolling direction. A number of microstructure analyses were performed to determine the possible correlation of the edge cracks with the subsurface microstructure. The contribution of the meniscus bands to the large and profound cracks can be determined from the following two facts, in addition to the much deeper Mg_2Si cavitation into the bulk material induced by the meniscus bands. First, considering the approximately 25 times elongation applied in the rolling direction after pass #18, the interval of the large and profound cracks (150 ± 20 mm) is in satisfactory agreement with the intervals of meniscus bands (5.5 ± 1.5 mm). Second, after scalping the cast surface layer on the short side of the ingot to remove all the inverse segregation zone and meniscus bands, the large and profound cracks completely disappeared, and the small and surficial cracks were reduced significantly (Fig. 6-10).

Several researchers reported that the Na-induced cracks were intergranular, owing to the segregation of Na on the aluminum grain boundaries [12,15,16]. In our observation, many edge cracks were found to be a mixture of intergranular and transgranular in nature. The large crack shown in Fig. 6-18 was intergranular in the middle and transgranular near the end of the path. The small crack at the right bottom of Fig. 6-18 was

transgranular, and the thin crack on the left side was mainly intergranular. As mentioned above, Mg_2Si particles precipitated in the interdendrite regions during solidification, which might be in the interiors of the aluminum grain or in the aluminum grain boundaries. Therefore, the Mg_2Si cavitation, as discussed above, may provide a reasonable explanation for the intergranular and transgranular propagation of the edge cracking. On the other hand, considering that a portion of the Mg_2Si particles that originated from solidification were dissolved during homogenization, the low-melting-point Na-rich layer on the periphery of Mg_2Si particles could have dissolved back to the matrix and segregated along the aluminum grain boundaries, leading to the intergranular propagation of the crack.

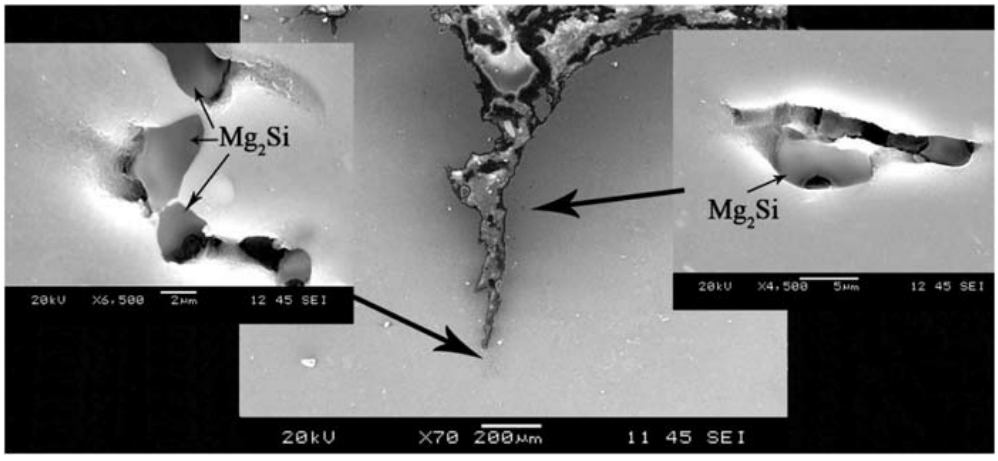

Fig. 6-17: Observation of Mg_2Si cavitation on an HS18 sample where the Mg_2Si particles and their associated, coalesced cavities were detected both along the crack path and in the crack tip.

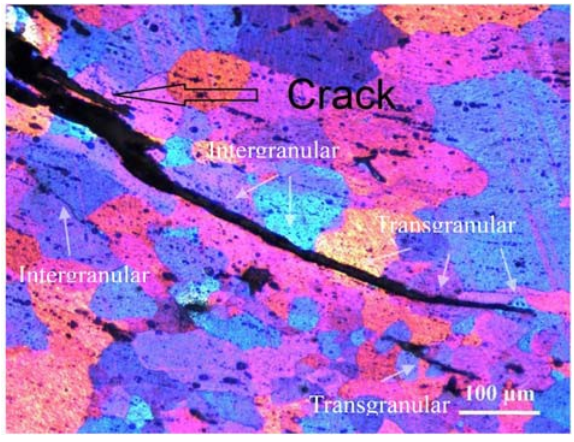

Fig. 6-18: The edge cracks display the mixing of intergranular and transgranular propagation in HS18 sample. The grain structure was revealed under polarized optical microscopy using electrochemically etching in Barker solution.

6.5 Conclusions

The occurrence of edge cracks during pilot-scale casting and hot rolling trials of AA5182 aluminum alloys containing two levels of Na were investigated. The present work focused on the impact of the intermetallic constituents in the DC-cast ingot on sodium-induced edge cracking. The following conclusions can be drawn:

1. After homogenization of the DC-cast ingots, two main intermetallic constituents remained in the ingot microstructure: Fe-rich intermetallic particles and Mg_2Si particles. The amount of Fe-rich intermetallics was two times higher and the volume of Mg_2Si particles was five times higher in the inverse segregation zone of the ingot subsurface region than in the bulk of the material.
2. During hot rolling, neither decohesion of the Fe-rich intermetallic particles from the aluminum matrix nor cavity formation were observed, indicating the absence of Fe-rich intermetallic particles in the crack initiation and propagation process. In contrast, Mg_2Si particles had a strong tendency to debond with the matrix and form cavities in the Mg_2Si/Al interface at the edges of the rolled strip. The Mg_2Si cavitation in the high Na alloy was much more severe than that in the low Na alloy.
3. Sodium promoted the Mg_2Si cavitation, most likely due to the segregation of Na on the periphery of the Mg_2Si particles, resulting in the high susceptibility of edge cracking in the high Na alloy. Numerous debonded Mg_2Si particles contaminated with Na in the ingot subsurface region provided favorable conditions for crack initiation and propagation.
4. The large edge cracks with a repetitive pattern could be related to the meniscus bands on the cast ingot surface. The meniscus bands moved the inverse segregation zone, along with the enriched Mg_2Si particles, deeply toward the bulk. The debonded Mg_2Si particles and their cavitation along the penetrated meniscus bands provided favorable paths for large crack propagation, which were particularly detrimental to the rolling recovery and process.

5. Removing the segregated zones and meniscus bands on the short side of DC- cast ingots or reducing the Na content can significantly reduce the edge cracking susceptibility.

6.6 References

[1] J. Hirsch, Recent development in aluminium for automotive applications, Trans. Nonferrous Met. Soc. China 24 (2014), pp. 1995–2002.

[2] W.S. Miller, L. Zhuang, J. Bottema, A.J. Wittebrood, P. De Smet, A. Haszler et al., Recent development in aluminium alloys for the automotive industry, Mater. Sci. Eng. A 280 (2000), pp. 37–49.

[3] J. Hirsch, Aluminium in Innovative Light-Weight Car Design, Mater. Trans. 52 (2011), pp. 818–824.

[4] P. Thomson and N. Burman, Edge cracking in hot-rolled Al-Mg alloys, Mater. Sci. Eng. 45 (1980), pp. 95–107.

[5] N.M. Burman and P.F. Thomson, Edge cracking and profile of hot rolled aluminum slabs, J. Mech. Work. Technol. 13 (1986), pp. 205–217.

[6] H. Riedel, F. Andrieux, T. Walde and K. Karhausen, The Formation of Edge Cracks during Rolling of Metal Sheet, Steel Res. Int. 78 (2007), pp. 818–824.

[7] D.G. Eskin and L. Katgerman, Macrosegregation Mechanisms in Direct-Chill Casting of Aluminium Alloys, Mater. Sci. Forum 630 (2010), pp. 193–199.

[8] R. Nadella, D.G. Eskin, Q. Du and L. Katgerman, Macrosegregation in direct-chill casting of aluminium alloys, Prog. Mater. Sci. 53 (2008), pp. 421–480.

[9] J.F. Grandfield and P.T. McGlade, DC casting of aluminium: Process behaviour and technology, Mater. Forum 20 (1996), pp. 29–51.

[10] N. Bayat and T. Carlberg, Surface structure formation in direct chill (DC) casting of al alloys, Jom 66 (2014), pp. 700–710.

[11] C.E. Ransley and D.E.J. Talbot, The embrittlement of aluminium magnesium alloys by sodium, J. Inst. Met. 88 (1959), pp. 150–158.

[12] G.H. Lu, Y. Zhang, S. Deng, T. Wang, M. Kohyama, R. Yamamoto et al., Origin of intergranular embrittlement of Al alloys induced by Na and Ca segregation: Grain boundary weakening, Phys. Rev. B - Condens. Matter Mater. Phys. 73 (2006), pp. 1–5.

[13] H. Yamada, K. Horikawa and H. Kobayashi, Effect of trace sodium on high temperature embrittlement in quasi-static and impact deformation of Al–5 mass% Mg alloys, J. Japan Inst. Light Met. 60 (2010), pp. 31–35.

[14] S. Zhang, O.Y. Kontsevoi, A.J. Freeman and G.B. Olson, Sodium-induced embrittlement of an aluminum grain boundary, Phys. Rev. B - Condens. Matter Mater. Phys. 82 (2010), .

[15] S. Zhang, O.Y. Kontsevoi, A.J. Freeman and G.B. Olson, Aluminum grain boundary decohesion by dense sodium segregation, Phys. Rev. B - Condens. Matter Mater. Phys. 85 (2012), pp. 1–8.

[16] K. Horikawa, S. Kuramoto and M. Kanno, Intergranular frecture caused by trace impurities in Al-5.5mol %Mg alloy, Acta Mater. 49 (2001), pp. 3981–3989.

[17] S.P. Lynch, Comments on Intergranular fracture caused by trace impurities in an Al-5.5 mol% Mg alloy, Acta Mater. 47 (2002), pp. 125–129.

[18] C.J. Simensen and U. Södervall, Investigation of trace elements in an Al-4.8 wt.% Mg-0.3 wt.% Mn alloy, Surf. Interface Anal. 30 (2000), pp. 309–314.

[19] S. Zhang, Q. Han and Z.K. Liu, Fundamental understanding of Na-induced high temperature embrittlement in Al-Mg alloys, Philos. Mag. 87 (2007), pp. 147–157.

[20] H. Hosokawa, H. Iwasaki, T. Mori, M. Mabuchi, T. Tagata and K. Higashi, Effects of Si on deformation behavior and cavitation of coarse-grained Al-4.5Mg alloys exhibiting large elongation, Acta Mater. 47 (1999), pp. 1859–1867.

[21] O. Engler and S. Miller-Jupp, Control of second-phase particles in the Al-Mg-Mn alloy AA 5083, J. Alloys Compd. 689 (2016), pp. 998–1010.

[22] O. Engler and J. Hirsch, Control of recrystallisation texture and texture-related properties in industrial production of aluminium sheet, Int. J. Mat. Res. 100 (2009), pp. 564–575.

[23] Y.J. Li and L. Arnberg, A eutectoid phase transformation for the primary intermetallic particle from Alm(Fe,Mn) to Al3(Fe,Mn) in AA5182 alloy, Acta Mater. 52 (2004), pp. 2945–2952.

[24] Y.J. Li and L. Arnberg, Solidification structures and phase selection of iron-bearing eutectic particles in a DC-cast AA5182 alloy, Acta Mater. 52 (2004), pp. 2673–2681.

[25] G. Yi, B. Sun, J.D. Poplawsky, Y. Zhu and M.L. Free, Investigation of pre-existing particles in Al 5083 alloys, J. Alloys Compd. 740 (2018), pp. 461–469.

[26] A. Poznak, D. Freiberg and P. Sanders, Automotive Wrought Aluminium Alloys, in Fundamentals of Aluminium Metallurgy, Elsevier Ltd., 2018, pp. 333–386.

[27] M.A. Moustafa, F.H. Samuel and H.W. Doty, Effect of solution heat treatment and additives on the microstructure of Al-Si (A413.1) automotive alloys, J. Mater. Sci. 38 (2003), pp. 4507–4522.

[28] T. Radetić, M. Popović and E. Romhanji, Microstructure evolution of a modified AA5083 aluminum alloy during a multistage homogenization treatment, Mater. Charact. 65 (2012), pp. 16–27.

[29] L.S. Bayoumi, Edge stresses in wide strip hot rolling, Int. J. Mech. Sci. 39 (1997), pp. 397–408.

Chapter 7: General Conclusion and Recommendations

7.1 General conclusions

This research was carried out to identify several aspects of the effect of alloying element and trace element contamination on the thermomechanical behavior of Al-Mg-Mn 5xxx alloys. Manganese and sodium are two critical elements which immensely affect the hot workability of the Al-Mg-Mn systems. The former is a key alloying element intentionally added to increase the mechanical properties by precipitation of Mn-bearing dispersoids, which decrease the hot workability. The latter contaminates the DC cast ingots and leads to the edge crack susceptibility during the hot rolling process.

It was observed that microscale Fe-rich intermetallics were increased in the volume fraction from 0.7 to 2.7% with Mn addition from 0.1 to 1%. Submicron Mn-containing dispersoids formed at 0.4% Mn during homogenization. From 0.4 to 1%, the size of dispersoids became finer and the composition enriched with Mn. Moreover, it accompanied by a higher number density of dispersoids but a remarkable increase in the fraction of dispersoid free zones (DFZs).

The microstructures of the deformed samples were analyzed on the basis of the Zener-Hollomon parameter. It was revealed that under the high-Z deformation conditions, dynamic recovery was the main softening mechanism, on which Mn had marginal influence. Under the medium conditions, CDRX occurred along with particle-stimulated DRX and DDRX. Mn effectively inhibited DRX in these deformation conditions. CDRX was the main recrystallization mechanism in the base alloy at low Z conditions. In the alloys with high Mn contents, DRV was the dominant softening mechanism in the grain interiors, while CDRX occurred in the DFZs.

Due to the presence of dispersoids, hot formability was decreased, which was consistent with the constitutive analyses showing an increase in the activation energy from 160 to 177 kJ/mol with increasing Mn addition from 01 to 1%. This increase was less than what reported in other aluminum alloys. The reason was attributed to the increase in the area of dispersoid

free zones as Mn was increased. DFZs underwent DRX easier than grain interior and decreased the effect of the work hardening.

Deformation at low temperatures and high strain rates was governed by instability mechanisms including shear banding and deformation band formation. The instability region falls between 0.03-1s^{-1} at 350℃ which decreased by temperature and disappeared at 450℃. Mn slightly increased the range of domain in terms of temperature and strain rate. The deformation bands occurred in all alloys regardless of dispersoids presence. It was also revealed that shear bands in the form of very fine grains occurred at the vicinity of primary intermetallics. The more is the Mn level in the alloy, more will be the volume of intermetallics and their imposed adjacent shearing.

Mn typically decreased the power dissipation in the safe zone deformation conditions by DRV retardance. Two peak power dissipation occurred at strain of 0.8: 400℃/0.001s^{-1} and 500℃/1s^{-1}. In both domains DRX was the active softening mechanism. The increase in Mn and Mn-bearing dispersoids decreased the range of temperature and strain rate at these domains because of DRX suppression. The optimum deformation temperatures/strain rates regarding the microstructure uniformity fell in 350-450°C/0.001-0.007s^{-1} for 0.1Mn alloy, which shrank to 375-425°C/0.001-0.002s^{-1} for 1Mn alloy.

It was shown that edge cracking provoked by Na contamination occurred at the edge surface of the rolled sheets. There was no cavity formation nor decohesion of Fe-rich intermetallic particles indicating no involvement of Fe-rich intermetallic particles in crack initiation and propagation. Comparatively, Mg_2Si intermetallics had a strong tendency to be debonded from matrix and formed cavities at the Mg_2Si/Al interface. The volume of Mg_2Si particles was five times higher in the subsurface region introducing more cavitation.

In the high Na alloy, cavitation on Mg_2Si was much more severe than in the low Na one because of higher matrix/particle interface contamination. Moreover, deep edge cracks observed to form repetitively on the meniscus bands. Meniscus bands were enriched with Mg_2Si constituents, which caused high volume of cavitation, and promoted the deep crack propagation. Removing the segregated zones and meniscus bands or reducing the Na content can significantly reduce the risk of edge cracking.

7.2 Recommendations and future works

The effect of Mn and Na addition on hot workability and microstructural evolution of the Al-Mg-Mn aluminum alloy were investigated. Based on the present study, following recommendations can be drawn for future work in this field:

1. Survey on the control of the size, morphology, and distribution of the dispersoids is necessary. The reason behind the different shapes of the Mn-containing dispersoids at different Mn levels is unknown. The volume of DFZ can be manipulated by addition of alloying elements and its impact can be studied on the hot deformation behavior.
2. It is known that dispersoids stabilize the matrix and they can suppress the crack propagation. However, the impact of different volume of dispersoids on the sodium-induced embrittlement remained intact.
3. The relationship of the different homogenization regimes in terms of particle coarsening and DFZ alteration in Al-Mg-Mn alloys needs to be investigated.
4. The impact of other alloying elements including Mg, Zr, Sc, and Cu on the deformation behavior and microstructure evolution is an interesting subject to be studied.
5. It is necessary to quantitatively investigate the correlation between the volume of Mg_2Si and the Na content on the crack initiation and propagation.
6. The microstructural evolution of Al-Mg-Mn alloys at strain rate of $0.1s^{-1}$ can be studied at different strains.
7. The shearing and deformation bands take place during deformation at low temperature and high strain rates and possess different inherent stored energies. The impact of each on the microstructure of the post annealing microstructure is a practical study for the industry.

Appendix I

Silicon is one of the main alloying elements added to aluminum alloys in order to increase the mechanical properties. Silicon has already shown influence on the reduction of hot workability of the dilute Al-Fe-Si alloys (1xxx) [Shakiba et. al., J. Mater. Eng. Perform, 2015]. In this study, it was attempted to investigate the impact of Si on the hot workability and microstructure evolution of the Al-Mg-0.4Mn alloy. For this purpose, three alloys containing base (0.05%), upper limit (0.2%), and double higher than upper limit (0.4%) Si contents on the basis of the standard composition of 5xxx alloys were designed. The alloys were casted in permanent mold and homogenized up to 500℃ then machined for hot compression test (similar to the procedure introduced in chapter IV). The pre-deformed microstructure showed a significant impact on the increase in the volume of intermetallics, specifically the Mg_2Si phase (Figs. 8-1a-d). However, there was a minor change on the solid solution level and the volume of dispersoid. Therefore, the influence of the Si addition on hot workability was negligible as the peak flow curves of Fig. 8-1e demonstrate. It seems the excessive Si reacts with Mg and increases the volume of constituents and has less contribution in dispersoids formation in the Al-Mg-0.4Mn alloy.

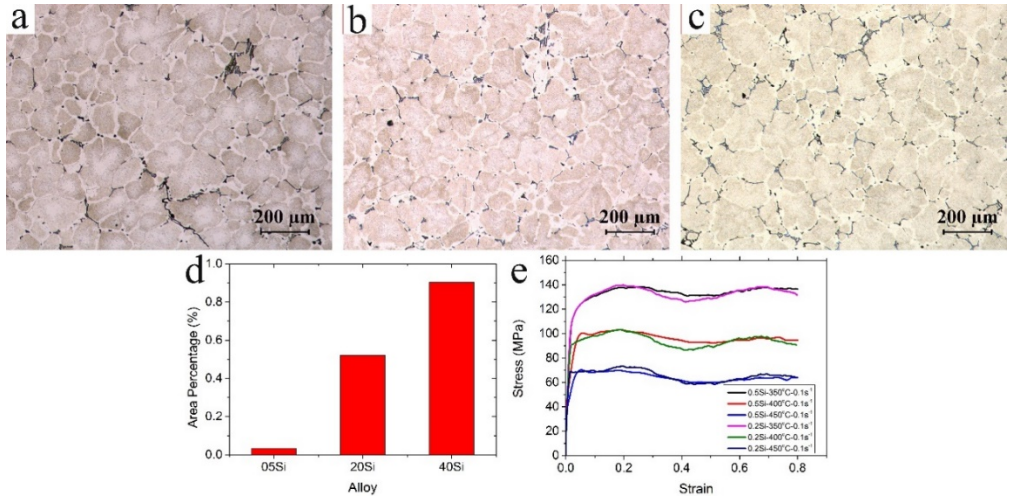

Fig. 8-1: The micrographs of the Al-Mg-0.4Mn alloys containing (a) 0.05%, (b) 0.2%, and (c) 0.4% silicon. (d) is the comparison between the volume of Mg_2Si and (e) exhibits some flow curves of hot compression test

Appendix II

Indexing in the EBSD analysis is based on the comparison of measured interplanar angles, which correspond to the angles between the Kikuchi bands. Theoretically, the geometry of a Kikuchi pattern is particularly unique for a crystal lattice orientation. In order to determine the crystal structure, it is sufficient for indexing to know the positions and widths of at least 3 bands in the pattern to calculate the intersection of bands and correspond to zone axes or poles. The grain orientation can then be determined with high precision. Fundamentals and detailed algorithms of indexing was described in Electron Backscatter Diffraction in Materials Science (Schwartz et al. 2000).

Optimum surface preparation is a fundamental requirement for high indexing acquisition. Electropolishing and colloidal silica polishing are implemented in the final metallographic stage. Normally the low index maps are the result of an inappropriate sample preparation. On an ideal surface, defects such as grain boundaries, cracks/porosities, and highly deformed structures show low indexing. Raw maps of Fig. 9-1a-b are exemplified for high Z and low Z deformed microstructures, respectively. As can be seen, high reliable indexing is obtained from highly recrystallized/recovered microstructure. Throug the noise reduction feature of the Tango software, the non-indexed grain boundaries are modified and a clear grain structure is obtained (Fig. 9-1c-d).

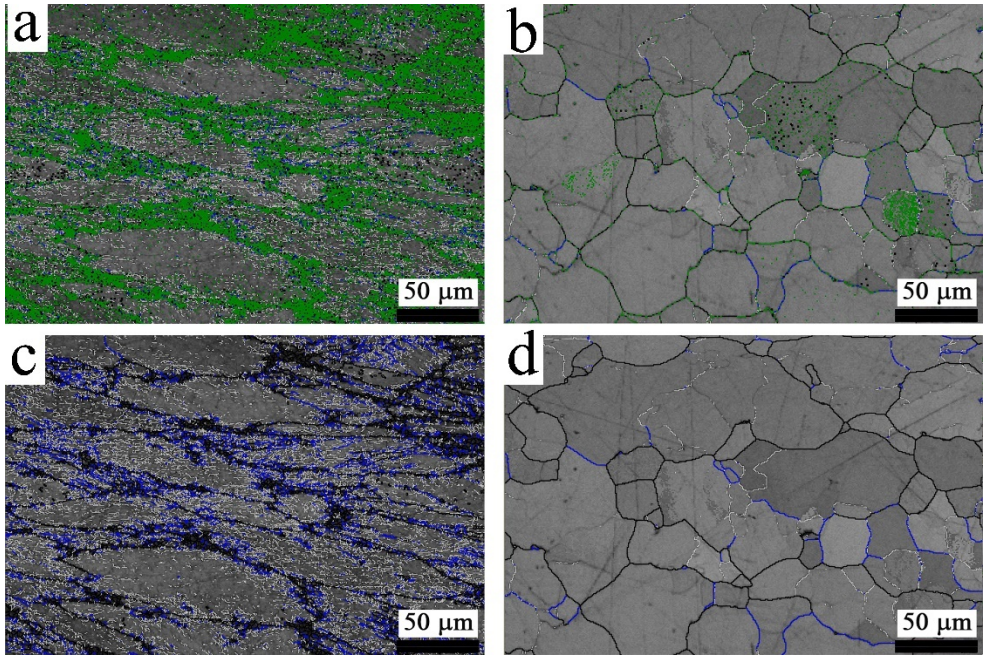

Fig. 9-1: The raw quality maps of 0.1Mn alloys deformed at (a) high Z (350℃/1s^{-1}) and (b) low Z (500℃/0.001s^{-1}) conditions. The green regions are non-indexed spots which are removed by noise reduction in (c) and (d).

During the experiment, some obstacles on the way of Kikuchi band detection will lead to the index miss. One technical problem that I faced was an issue in the beam emission equipment of the microscope. It reduced the static background acquisition and increased the frame time. The result was the extremely low indexed raw map and consequently a low-quality noise-reduced map as presented in Fig. 9-2. The problem was solved by replacement of the defective hardware. The quality of the pattern can also drop at low magnifications and/or if the distance of the measured location increases from the point at which the system had been calibrated initially.

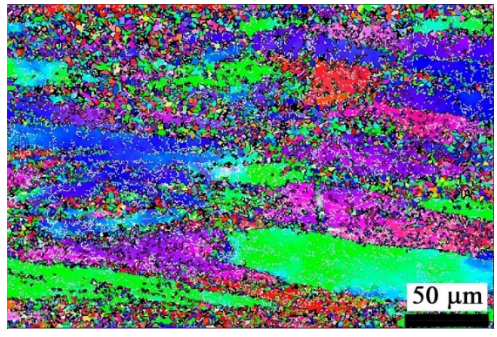

Fig. 9-2: The low index IPF map of 0.7Mn sample deformed at 350℃/1s^{-1}

List of publications

Journal articles

1. M. Mofarrehi, M. Javidani, X.-G. Chen, “On the intermetallic constituents in the sodium-induced edge cracking of hot-rolled AA5182 aluminum alloys”, **Philosophical Magazine, Vol. 101 (16), 2021, 1849-1870**, doi.org/10.1080/14786435.2021.1937368.
2. M. Mofarrehi, M. Javidani, X.-G. Chen, “Effect of Mn content on the hot deformation behavior and microstructure evolution of Al-Mg-Mn 5xxx alloys”, **Materials Science and Engineering A**, **Vol. 845, 2022, 143217,** doi.org/10.1016/j.msea.2022.143217**.**

Scientific posters

1. M. Mofarrehi, M. Javidani, X.-G. Chen, “The role of the constituent phases of 5xxx alloys in the sodium induced edge cracking during hot rolling”, REGAL student’s day, 2019, Laval University, Quebec City.
2. M. Mofarrehi, M. Javidani, X.-G. Chen, “Impact of Mn concentration on dispersoid evolution in AlMgMn alloys by applying two step homogenization treatment”, REGAL student’s day, 2020, ETS, Montreal.
3. M. Mofarrehi, M. Javidani, X.-G. Chen, “The impact of Mn on the hot workability and processing map of Al-Mg-Mn alloys”, REGAL student’s day, 2020, UQATR, Trio-Rivier, (the best poster award).

Contribution:

Akbar Heidarzadeh, and X.-Grant Chen, Mousa Javidani, Mohammadreza Mofarrehi, Amir Farzaneh, “Submerged dissimilar friction stir welding of AA6061 and AA7075 aluminum alloys: Microstructure characterization and mechanical property”, **Metals, Vol. 11, 2021, 1592**, doi.org/10.3390/met11101592.